ZnO based micro and nanomaterials for breast cancer therapy

Dissertation

zur Erlangung des akademischen Grades

Doktor der Ingenieurwissenschaften

(Dr.-Ing.)

der Technischen Fakultät

der Christian-Albrechts-Universität zu Kiel

Tehseen Riaz

Kiel, October 2022

Academic supervisor,1st Reviewer: (Prof. Dr. Rainer Adelung)

2nd Reviewer: (Prof. Dr. Franz Faupel)

Date of oral examination: (15.12.2022)

Abstract

Breast cancer is one of the largest causes of women's death in the world. Millions of women are affected by breast cancer. Despite the significant achievements in breast cancer treatment, some problems, such as damage to healthy tissues and adverse effects including myelosuppression, heart failure, and infertility have been observed in the case of the non-specific systemic delivery of the cytostatic agent. Nanoparticles are gaining attention as a valuable solution to addressing these problems because of their unique characteristics, such as their enhanced permeability and retention in tumor tissue. In this thesis, it is investigated and compared the effect of spherical zinc peroxide (ZnO_2) nanoparticles of different sizes, commercially available ZnO nanopowder as well as tetrapodal-shaped ZnO (T-ZnO) microparticles on breast cancer (MCF-7) cells as a function of particle concentration. The cytotoxicity and viability of the different particles were investigated for breast cancer (MCF-7) cells in comparison with normal fibroblasts cells (RMF-EG). The results indicated that ZnO_2 nanoparticles of average size between 20 - 80 nm were most effective against MCF-7 cells and showed minimal toxicity to normal fibroblasts (RMF-EG) cells. To better understand the underlying mechanism, we investigated cellular uptake into MCF-7 human breast cancer cells and correlated their uptake with cell death. In summary, it is demonstrated that ZnO_2 particles are taken up by MCF7 cells and induced stronger cytotoxic effect in these malignant cells. This suggested their potential clinical advantages (application to reduce side-effects of non-malignant tissue) in treatment of breast cancer. It was also anticipated that ZnO_2 nanoparticles could be used for the development of a pH-sensitive drug delivery system that minimizes drug toxicity.

Acknowledgments

Foremost, I would like to express my sincere gratitude to my advisor, Prof. Dr. Rainer Adelung, Chair of Functional Nanomaterials, Kiel University for the continuous support of my Ph.D. research, for his patience, motivation, enthusiasm, and immense knowledge. His guidance helped me in all the time of research and writing of this thesis. I could not have imagined having a better advisor and mentor for my Ph.D. research. I thank him for allowing joining his research group and write my doctoral thesis under his supervision.

Besides my advisor, I would like to thank the group leader of my thesis: Dr. Fabian Shutt for his encouragement and insightful comments. The completion of this project could not have been accomplished without his support.

My sincere thanks also go to Prof. Dr. med. Dirk Bauerschlag, Prof. Dr. Norbert Arnold, and Dr. Nina Hedemann, Department of Gynecology and Obstetrics of the Universitätsklinikum Schleswig-Holstein (UKSH) Kiel, for offering me the opportunity to work in their group and leading me working on biological and cell culture part of the project. I would especially like to express my deep and sincere gratitude to Dr. Nina Hedemann. She has taught me to carry out cell culture experiments, how to work in biological labs, and to present the biological data by using suitable software. It was a great privilege and honor to work and study under her guidance. I am extremely grateful for what she has offered me.

I was not alone in obtaining all the experimental results. My research assistant, Catharina Verkooyen, and other group members of the Department of Gynecology and Obstetrics UKSH, Sigrid Hamann, and Dr. rer. NAT. Inken Flörkemeier helped me throughout my experimental work. They provided me with every facility in their lab that was needed for my research.

The person who introduced me to the group "Molecular Immunology" Institute of Immunology, UKSH Kiel should not go unforgotten, Dr. Marcus Lettau, was the one who introduced me to this wonderful group when I was searching for Flow Cytometry measurements. I thank him wholeheartedly for that. It was a pleasure working with every one of them.

I would like to thank DAAD (**Deutscher Akademischer Austauschdienst**) for funding the project "Doxorubicin loaded ZnO for targeted drug delivery to breast cancer cells" as well as for financial

assistance during my stay in Germany. It was a great pleasure collaborating with my DAAD coordinator Mrs. Dagmar Beerwerth, and I thank all the other members of the DAAD Group for organizing the very informative meetings every year.

Last but not least, I would like to express my utmost gratitude and debt toward my parents, brother, and sister, whose continuous love, help, patience, and encouragement motivated me to overcome all the obstacles to complete my work.

Table of Contents

Abstract iii
Acknowledgments iv
List of Figures viii
List of Tables xi
Chapter 1: Introduction 1
1.1. Motivation of thesis 1
Chapter 2: Theoretical background 3
2.1. Enhanced permeability and retention (EPR) effect 3
2.2. Zinc oxide nanoparticles (ZnO NPs) 4
2.3. Zinc ion release from ZnO NPs 5
2.4. Generation of reactive oxygen species (ROS) by ZnO NPs 6
2.5. Cellular fate after treatment with ZnO NPs 6
2.6. ZnO NPs as innovative anti-tumor agents 7
2.7. Conventional drug delivery system 8
2.8. Doxorubicin (DOX) 11
2.9. An overview of ZnO based Doxorubicin delivery systems 12
2.10. State of the art syntheses of zinc peroxide nanoparticles (ZnO_2 NPs) 13
2.11. Properties and common applications of zinc peroxide nanoparticles 15
2.12. Dynamic underwater chemistry for the synthesis of size-tailored zinc per oxide nanoparticles 15
2.13. Flame transport synthesis (FTS) of tetrapodal ZnO micro-nano structures 18
2.14. MCF-7 Breast Cancer Cells 20
2.14.1. Uses of MCF-7 20
2.15. RMF-EG cells 21
Chapter 3: Theory of Materials and Methods 23
3.1. ApoLive-Glo™ Multiplex Assay for cell culture 23
3.2. Zinc ion release from ZnO and ZnO_2 micro and nanostructures 26
3.3. Zinquin ethyl ester 28
3.4. Flow cytometry 29
3.5. Scanning electron microscopy (SEM) 31

3.6. RAMAN spectroscopy 34
3.7. Ultraviolet and visible spectroscopy 37
3.8. X-ray diffraction (XRD) 40
3.9. Transmission electron microscopy (TEM) 43
3.10. Energy dispersive X-ray analysis (EDX) 45
3.11. Techniques used in cell culture 47
Chapter 4: Materials and methods 52
4.1. Synthesis and Characterization of ZnO tetrapods and ZnO_2 NPs 52
4.2. Determination of cytotoxicity of ZnO_2 NPs and T-ZnO 54
4.3. Zinc ion release from ZnO and ZnO_2 micro and nanostructures 55
4.4. Protocol for intracellular zinc ion measurement 56
4.5. Release of DOX from ZnO_2 NPs 57
4.6. Cell culture protocol of MCF-7 cells for bare and drug loaded ZnO_2 NPs 57
Chapter 5: Results and discussion 59
5.1. Scanning electron microscopy 59
5.2. RAMAN spectroscopy 61
5.3. X-ray diffraction analysis of micro and nano ZnO and ZnO_2 62
5.4. Transmission electron microscopy of ZnO_2 NPs 63
5.5. Transmission electron microscopy of DOX loaded ZnO_2 (20-80 nm) nanoparticles 64
5.6. Cytotoxicity tests 67
5.7. Zinc ion release from ZnO and ZnO_2 micro and nanostructures 71
5.8. Assessment of zinc ions released into MCF-7 cells 73
5.9. pH-responsive drug release profile of ZnO_2 NPs (20-80 nm) 79
5.10. Impact of bare and drug-loaded ZnO_2 NPs (20-80 nm-sized) on cell viability of MCF-7 cells 81
Summary and outlook 83
Chapter 6: Bibliography 84

List of Figures

Figure 2.1: Nanoparticle design involves tuning particle characteristics (the inner circle) and their behavior and particle–cell interactions within the human body (outer circle). 4
Figure 2.2: Comparison of the drug release patterns by the traditional drug delivery system and the nanocarrier drug delivery system. 9
Figure 2.3: The schematic shows that when nanochemistry occurs at the overheated zone, the formed nanoparticles assembled as nanoclusters erupt towards the much colder region for further growth. This tendency can be controlled and utilized for tailoring the size 16
Figure 2.4: Cell mortality induced by cytotoxic effect of ZnO_2 nanoparticles. Flow cytometric analysis of cells (a) Jurkat ATCC, (b) PBMC, (c) U937, (d) HT29, (e) Panc89, (f) L929Ts stained with PI (PI-positive fraction) treated with the 126 and 426 nm ZnO_2 nanoparticles (black and red columns, respectively) at various concentrations for 24 h. '0' concentration represents blank samples containing the cell culture media but in absence of ZnO_2 nanoparticles 18
Figure 2.5: Three-dimensional T-ZnO particles produced by the Flame Transport Synthesis (FTS) 19
Figure 2.6: A microscopic image of elongated spindle-shaped human breast fibroblasts of size around 30-35 µm (RMF-EG) taken at ×40 22
Figure 3.1: Cell viability assay chemistry. The cell-permeant substrate enters the cell, where it is cleaved by the live-cell protease activity to produce the fluorescent AFC. 24
Figure 3.2: Schematic diagram of the ApoLive-Glo™ Multiplex Assay. Cell viability fluorescence is measured at $400_{Ex}/505_{Em}$. 25
Figure 3.3: Structures of Zincon (2-carboxy-20 -hydroxy-50 -sulfoformazylbenzene) in its free and zinc-bound form. 28
Figure 3.4: Chemical structure of zinquin ethyl ester 28
*Figure 3.5: Schematic and working of scanning electron microscope** 32
Figure 3.6: Schematic diagram of the sample, incident light and collection optics in the Raman spectrometer. 35
Figure 3.7: Three types of scattering by a molecule excited by a photon with energy E = hv. The most common transitions are marked with bold arrows. 37
Figure 3.8: UV-visible spectrometer working 39
Figure 3.9: Bragg's law reflection 41
Figure 3.10: Components of X-ray diffractometer 43
Figure 3.11: Classification of transmission electron microscopy 44
Figure 3.12: Working principle of transmission electron microscope 45
Figure 3.13: Energy dispersive X-ray spectroscopy schematic and working 46
Figure 3.14: EDX spectrum obtained for synthesized zinc per oxide nanoparticles. 46
Figure 3.15:Components of Light Microscope taken at Oncology lab UKSH, Kiel 48
Figure 3.16: Schematic of working of microplate reader for cytotoxicity assays 50
Figure 3.17: Trans-illumination of hydrodynamically focused cells done orthogonally by a laser(s) and a brightfield light source. 51

Figure 4.1: (a) Color changes in zinc stock solution after adding Zincon solution (b) Structures of Zincon in its free and zinc-bound form. 56
Figure 5.1:The Scanning Electron Microscope (SEM) images of the zinc peroxide nanoparticles (a-d) under higher magnification. For figures a-d, particles were formed with size in the nano range, and, the particle separation is good in type 1 nanoparticles (a, b). (e) SEM image of 3D tetrapodal zinc oxide (T-ZnO) powder. (f) SEM image of crushed tetrapodal zinc oxide (T-ZnO) at low magnification. Figure (g) shows the scanning electron micrograph of ZnO nanoparticles from Sigma Aldrich. 60
Figure 5.2: RAMAN spectra of ZnO tetrapods, commercial ZnO and ZnO_2 NPs..... 61
Figure 5.3: XRD patterns of T-ZnO (untreated, crushed, and etched), commercial ZnO, and ZnO_2 NPs. 62
Figure 5.4: TEM images of unloaded nanoparticles with sizes of 50-300 nm and 20-80 nm are shown in TEM bright-field images (A) and (C), respectively. The area of the white square in (A) is depicted in (B) at a larger magnification for particle size in comparison with (C). The SAED pattern (D) indicates the presence of hexagonal ZnO phase. The orange line in the STEM HAADF image (E) marks the path of the EDX line scan. The counts for Zn and O from the line scan in (E) are plotted in (F). The 0 nm position in the plot is chosen to be the edge of the particle. 64
Figure 5.5: The EDX spectra of ZnO_2 nanoparticles with sizes of 50-300 nm (b) of the area of the white square in (a) and the EDX spectra of ZnO_2 nanoparticles with sizes of 20-80 nm (d) of the area of the white square in (c). 65
Figure 5.6: (a, b) TEM images of Doxorubicin-loaded nanoparticles with sizes of 20-80 nm are shown in TEM bright-field images (c,d). The EDX spectra of drug-loaded ZnO_2 nanoparticles with sizes of 20-80 nm (d) of the area of the white square in (c)...... 66
Figure 5.7: Effect of ZnO_2 nanoparticles (a) on cell viability of human breast cancer cells (MCF-7) (b) on normal fibroblasts determined by ApoLive-GloMultiplex Assay. Passage number: P15–P25. Seeded cell numbers: 17000 cells/cm^2 for MCF-7 and 10,000 cells/cm^2 for RMF-GE; Particle concentration: 0.001–10 mg/ml; duration of treatment: 48 h. Each symbol represents the mean ±SE of n=3 independent experiments with three-fold determinations. 67
Figure 5.8: Effect of ZnO tetrapods (a) on cell viability of human breast cancer cells (MCF-7) (b) on normal fibroblasts determined by ApoLive-GloMultiplex Assay. Passage number: P15–P25. Seeded cell numbers: 17,000 cells/well for MCF-7 and 10,000 cells/well for fibroblasts; Particle concentration: 0.001–10 mg/ml; duration of treatment: 48 h. Each symbol represents the mean ±SE of n=3 independent experiments with three-fold determinations. 69
Figure 5.9: Release of Zn^{2+} ions from different ZnO structures in buffer solutions and culture medium at pH 7.4, 5.5 and 7.2...... 72
Figure 5.10: (a) Staining intensity of zinquin alone without and with ZnO_2 nanoparticles treatment for 2h and 4h (b) Percentage dead (FRD+) and alive cells (FRD-) compare without and with ZnO_2 nanoparticles treatment for 2h and 4h. 73
Figure 5.11: (a) Percentage dead cell (FRD+ staining intensity) compare of untreated and ZnO_2-treated cells for 2h and 4h (b) percentage alive cell (FRD- staining intensity) compare of untreated and ZnO_2-treated cells for 2 h and 4 h. 74

Figure 5.12: (a) Uptake of ZnO_2 particles in terms of staining intensity of zinquin for untreated and after 2 h of incubation with NPs (b) Staining intensity of zinquin for dead (FRD+) and alive (FDR-) cells (c) Percentage of staining intensity of dead (FRD+) cells with (2 h incubation) and without ZnO_2 NPs treatment. 75
Figure 5.13: (a–d) Bright field and confocal images of MCF-7 cells untreated (a, b) and exposed to 1mg/ml ZnO_2 NPs (c, d) showing the release of Zn^{2+} inside the cells over time (2 h and 4 h) as indicated by the increase in the intensity of the Zn^{2+} indicator, zinquin. 77
Figure 5.14: (a–c) Bright field and confocal images showing MCF-7 cells (a) untreated and exposed to 1 mg/ml of the ZnO_2 NPs led to the release of Zn^{2+} inside the cells over time; (b) 2 h and (c) 4 h, as indicated by the increase in the intensity of the Zn^{2+} indicator, Zinquin (purple). Toxic levels of Zn^{2+} ions inside the cell subsequently resulted in cellular penetration of FRD (red), indicating the loss in viability and cell death. 78
Figure 5.15: Cumulative drug release profile of drug loaded ZnO_2 nanoparticles (20-80 nm). . 80
Figure 5.16: Effect of 20-80 nm-sized ZnO_2 nanoparticles (bare and drug-loaded) on cell viability of human breast cancer cells (MCF-7) determined by ApoLive-GloMultiplex Assay. Passage number: P15–P25; seeded cell numbers: 17,000 cells/well; particle concentration: 0.001–10 mg/ml; duration of treatment: 48 h. Each symbol represents the mean ±SE of n=3 independent experiments with three-fold determinations. 81

List of Tables

Table 1: Impact of nanoparticles and ZnO tetrapods (T-ZnO) on IC50 values for MCF-7 cells 70
Table 2: Impact of nanoparticles and ZnO tetrapods (T-ZnO) on IC50 values for RMF-EG cells 70

Chapter 1: Introduction

Random growth of cells called cancer is becoming increasingly common in humans and is also one of the leading causes of death. Using chemotherapy, it is challenging to eliminate the cancer tissues without affecting the body's normal organs because of its complex nature, multidrug resistance capability, and metabolic pathways. Thus, the damage of cancer cells accompanies the damage to the body's healthy tissues. This usually leads to failure of usual cancer treatments which has excessive systemic side effects. Therefore it is essential to fabricate on-demand cancer treatment, especially a drug delivery system which can deliver therapeutics in a dose-controlled manner [1–5].

The term nanomedicine was introduced in 2000 and is defined as the usage of nanoscale materials (10–1,000 nm) in medicine [6–8]. Nanomedicine is also known as "nanobiotechnology," based on its applications in nanomaterials such as nanoparticles. Several therapeutic nanoparticle (NPs) platforms, such as albumin nanoparticles, liposomes, and polymeric micelles, have been approved for cancer treatment and several other nanotechnology-enabled therapeutic modalities are under clinical investigation [9,10].

1.1. Motivation of thesis

Breast cancer is the most common and malignant cancer in women and characterized by a high resistance to the conventional therapy. Firstly, the systemic chemotherapy is inefficient, as the drug is distributed in the entire body and damage the healthy cells. Secondly, to attain a therapeutic effect, high drug concentrations are needed which eventually lead to strong side effects and an overall low efficacy of the treatment. In order to increase the patients' lifetime and reduce the side effects, more advanced treatment strategies are required, involving, e.g., the use of ZnO based nanoparticles or drug loaded nanoparticles for enhanced efficacy as well as local drug administration at the tumor site. The local delivery of these nanoparticles allows several advantages over systemic treatment, including strongly increased efficiency due to reduced side effects, a lower required drug concentration, and an associated higher patients' compliance.

In the framework of this thesis, alternative treatment schemes for improved breast cancer therapy were investigated. The motivation of this dissertation is also to present particularly alternative

breast cancer treatment schemes involving the use of ZnO tetrapods and spherical ZnO as drug or therapeutic agents. The tetrapds and spherical ZnO nanoparticles have been thoroughly investigated in an in vitro model using a novel cell viability assay (Apolive Glu Multiplex Assay). In the next step, spherical zinc peroxide nanoparticles were developed as pH responsive drug delivery system (DDS) and their uptake by MCF-7 breast cancer cells was investigated by fluorescence-activated single cell sorting (FACS) analysis.

The major aim of this thesis is to compare the structural, morphological properties, and biological toxicity of different types of ZnO and ZnO_2 nano- and microparticles against human breast cancer and healthy breast cells. The design of these materials is based on a simple flame transport synthesis (FTS) technique for generating micro-nano T-ZnO materials and underwater Leidenfrost nanochemistry to create size-tailored ZnO_2 nanoparticles.

This interdisciplinary thesis integrates the knowledge from biology bridged by applying materials science and micro and nanofabrication technology. In the materials part, the structural and morphological properties of T-ZnO and nano ZnO_2 were investigated and compared to commercial ZnO nanoparticles. In the biological part, a therapeutic window was defined for the cytotoxicity and viability of the aforementioned particles investigated for breast cancer (MCF-7) cells in comparison with normal human breast cells (RMF-EG). This thesis deals with another challenge in the perspective of biological science, i.e., to study the ability of ZnO_2 nanoparticles to be uptaken by cancer cells. After being uptaken, these ZnO_2 nanoparticles caused the cell death of cancerous cells due to Zn^{+2} ions released at low pH inside the cellular environment. At the same time, it has been successfully demonstrated that these ZnO_2 nanoparticles exhibited a pH-dependent drug delivery profile for an anticancer drug Doxorubicin. Therefore, a material (zinc per oxide) synthesized with a novel methodology (Leidenfrost nanochemistry) has been proposed here as a novel drug delivery system that, as per our best knowledge, has not been reported before.

Chapter 2: Theoretical background

2.1. Enhanced permeability and retention (EPR) effect

Accompanied by vast progress in cancer nanomedicine, several opportunities and challenges lie ahead. The main challenge is the complexity and the heterogeneity of tumors. Mostly solid tumors are administered systemically with the help of therapeutic NPs; nanoparticles accumulate in the tumor through the enhanced permeability and retention (EPR) effect [11–14]. EPR effect is generally considered the result of leaky tumor vasculature and poor lymphatic drainage. Multiple biological processes in the systemic delivery of nanoparticles influence the EPR effect. These include protein-NPs interaction, blood circulation, interaction with the perivascular tumor microenvironment (TME), tumor cell internalization, and tumor tissue penetration. Properties of nanoparticles, e.g., composition, size, surface, mechanical properties, and porosity, can influence the aforementioned biological processes.

Therefore, nanoparticles are designed for tumor therapy through their size, charge, composition, morphology, and surface properties (Figure 2.1). These properties affect nanoparticles circulation time in the bloodstream, their diffusion in the extracellular environment, their extravasation out of the vessels into the tissue, and their degradation and internalization within the tumor cells. Thus, the tumor environment is specifically affected by nanoparticles to achieve cancer cell death.

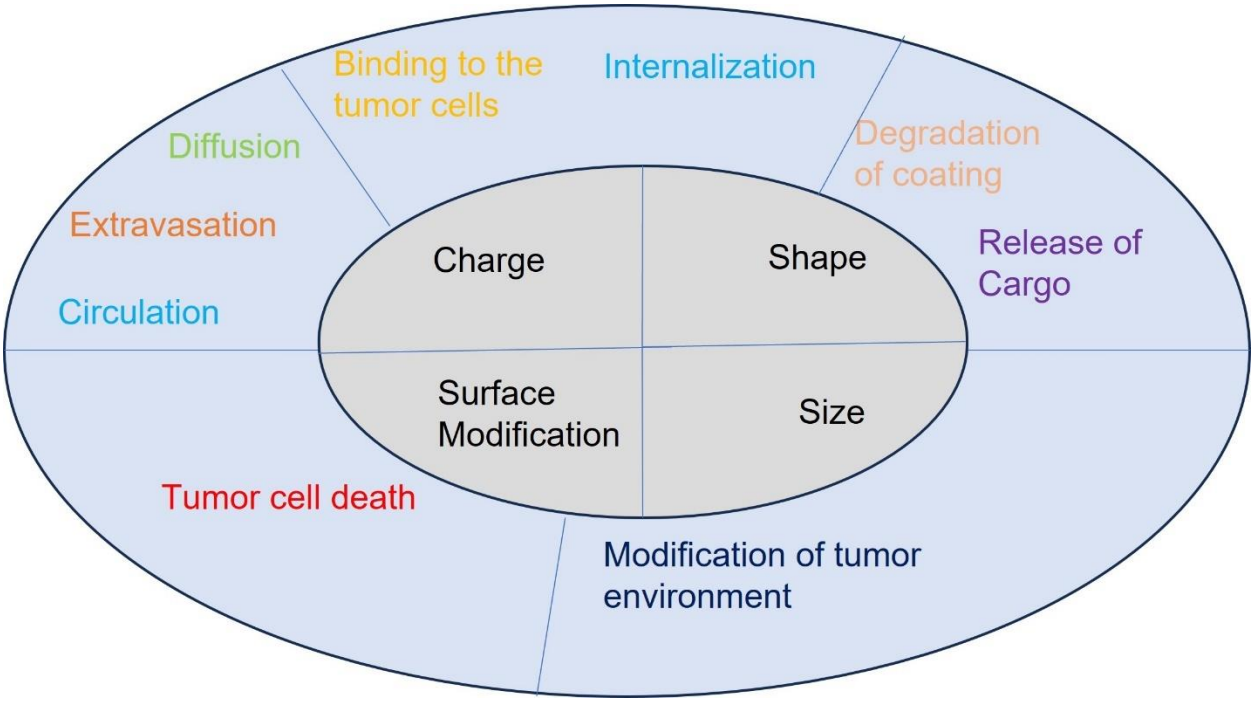

Figure 2.1: Nanoparticle design involves tuning particle characteristics (the inner circle) and their behavior and particle–cell interactions within the human body (outer circle).

2.2. Zinc oxide nanoparticles (ZnO NPs)

Among the manufactured compounds of zinc**,** zinc oxide (ZnO) is one of the most important compounds having a prodigious diversity of applications in various branches of industry. ZnO exhibits a hexagonal wurtzite structure (crystalline) at ambient conditions. Zinc oxide nanoparticles (ZnO NPs) exist in various morphologies with a wide range of properties. These surface, chemical, and morphological properties make ZnO one of the most versatile nanomaterials [15,16]. Especially chemical characteristics of ZnO make it favorable for biomedical applications. For example, its inexpensive synthesis, easy tenability, and the possibility of surface modification by different coatings make it suitable materials for different biomedical applications.

ZnO is recognized as a so-called GRAS (generally recognized as safe) substance by the U.S. Food and Drug Administration (FDA) [17]. This allows their use in healthcare products. ZnO is a component of many medical products and in lotions and creams, for example, in sun cream and wound healing products [18]. Zinc oxide is relatively non-toxic and biocompatible as compared to

other metal oxides. The remaining part of this introduction will highlight the essential aspects of ZnO NPs in biological systems to understand their potential for application in cancer medicine.

2.2.1. Surface charge of ZnO NPs

The most favorable properties for biomedical applications of ZnO NPs are their characteristic electrostatic properties. ZnO surface is hydroxylated with water molecules due to the amphoteric properties of zinc. Water (H_2O) molecules are deprotonated in an aqueous medium of pH value ≥9 (the isoelectric point). These molecules leave behind a negatively charged surface with surface-bound hydroxide groups (Zn–(OH^-). At acidic or neutral pH values (lower pH values), the nanoparticle's surface takes protons from the environment, which results in a positively charged surface because of the formation of $Zn(OH_2)^{x+}$ groups or positively charged Zn^{2+} surface sites after the release of H_2O [19,20]. This means that ZnO NPs are positively charged under physiological conditions (pH value of 7.4). This positive charge on nanoparticles is responsible for likely conditions for their interaction with tumor cells which commonly carry a negative surface charge due to a special feature of their metabolism, called the Warburg effect [21].

2.3. Zinc ion release from ZnO NPs

ZnO NPs are inclined to dissolve with an associated release of Zn^{2+} ions due to zinc's amphoteric properties [22]. Zinc ions dissolution occurs more easily in an acidic environment. This means that ZnO NPs are dissolved into zinc ions in the acidic tumor microenvironment [23]. Zn^{2+} ions released from ZnO NPs in the cell culture medium are complexed by various medium components, such as amino acids, carbonate, phosphate, and serum proteins.

Along with the retained proteins, zinc carbonate and zinc phosphate take part in the crystalline or amorphous form. These proteins are another micro or nano-sized species that could affect the biological system [24–27]. In addition, ZnO NPs possess a solid capacity to adsorb proteins onto their surface, the protein corona. Thus the observed toxicity may also originate from nanoparticle-protein complexes, which vary in cellular uptake, reactivity, and surface chemistry from the original uncoated nanoparticles [28].

The stability against zinc oxide nanoparticles dissolution could be influenced by coatings consisting of polymers (e.g., polyethylene glycol) [29], lipids [30]or silica [31]. Several studies reported that proteins and coatings deposited on the ZnO NPs surface reduce their cytotoxicity in adherent

cell cultures [32]. This might be due to reduced zinc ions dissolution, reduced reactive oxygen species (ROS) generation, or less surface contact between cells and NPs [33–36].However, in suspension cell models, protein coatings can increase cytotoxicity due to increased dispersion stability and a decrease in sedimentation and aggregation [35].

2.4. Generation of reactive oxygen species (ROS) by ZnO NPs

Due to their small size, large surface area, and high reactivity, nanoparticles can generate Reactive Oxygen Species (ROS). Various metal oxide nanoparticles generate ROS by contributing to Fenton and Haber–Weiss reactions. However, this mechanism could be ruled out for ZnO NPs because zinc ions (Zn^{2+}) are redox inert in biological systems. Still, ZnO NPs are also potent generators of ROS.

It has been reported that ZnO nanoparticles can generate ROS under biotic (in the cell's existence) and abiotic conditions (in the nonexistence of cells) [37]. The in vitro cytotoxicity of ZnO nanoparticles was found to be greatly increased by their photocatalytic activity. This was presented by using visible light or UV irradiation in combination with NPs [38,39]. Additionally, the production of ROS at the ZnO nanoparticle's surface is also probable in the dark, fostered by the surface defects [40].

It is shown in numerous studies [37,41–44] that ZnO NPs can induce the intracellular increase in ROS concentrations. In principle, ROS generation results from the direct interaction of ZnO nanoparticles with the Zn^{2+} released by nanoparticles or biological surroundings. Which mechanism causes the intracellular rise of ROS is hard to unravel because of the challenging phenomenon of the intracellular visualization of ZnO NPs in a living system. Mitochondrial damage is mainly related to the intracellular rise in ROS after treatment with ZnO nanoparticles, but it is unclear whether the intracellular increase of ROS concentrations is originated or affected by mitochondrial damage.

2.5. Cellular fate after treatment with ZnO NPs

One common question regarding nanotoxicity is related to the mechanism of cell death, which means whether cells die via necrosis, apoptosis, or autophagy-associated cell death. In most cases, apoptosis [45–48] or necrosis in conjunction with apoptosis [49,50] has been reported after the treatment

with ZnO NPs. It is evident from several reports that after ZnO nanoparticles treatment, apoptosis is induced through intrinsic or mitochondrial pathways [43,51]. However, in some cases, mitophagy [52] or autophagy [48,53] occurred. Mitochondria play an essential role in determining the cellular fate after ZnO treatment. They can be directly involved in ROS generation, or they can be one of the first targets of ROS generated somewhere else inside the cell. In addition to mitochondria, the nucleus of a cell may sustain eternal damage after ZnO NPs treatment. Intracellular signaling cascades regulate the fate of cells in the end. These cascades, most likely through the mitochondrial pathway, initiate controlled apoptosis, or they can try to repair the sustained damage. Membrane leakage necrosis is also possible in the case of an uncontrolled increase in ROS.

2.6. ZnO NPs as innovative anti-tumor agents

Zinc oxide nanoparticles are promising candidates as novel anti-tumor agents have been evident during the past years. Several studies have been published that demonstrate the toxicity of ZnO NPs against tumors and reported that ZnO NPs retain selective anti-cancer characteristics *in vitro* that can aid in separating target the cancer cells to healthy tissue [53–62].

The selective toxicity mechanism of ZnO NPs against tumor cells is still debatable. Different factors have been proposed to play an important part in the mechanism of cytotoxicity that delivers the better killing of tumor cells by ZnO nanoparticles. One hypothesis is the high metabolic activity of the characteristically fast-dividing tumor cells [53,63] is responsible for the preferential killing of tumor cells. Another hypothesis is the easy dissolution of ZnO NPs in the acidic tumor microenvironment originating from the Warburg effect. In addition, the negatively charged membrane of cancer cells favors the interaction with the positive surface charge of ZnO nanoparticles [64].

In addition to the possibility of using ZnO NPs as an individual therapeutic agent, there exists the option to combine them with established methods of standard therapies such as radiotherapy and chemotherapy. Furthermore, it has also been proposed that as the combinational therapy, ZnO nanoparticles can be loaded with anti-cancer drugs to achieve additive or synergistic effects of both treatments. Initial studies show favorable results regarding combining ZnO nanoparticles with daunorubicin, doxorubicin, cisplatin, or paclitaxel [65–69].

Owing to the photocatalytic activity of ZnO NPs, it can also be favorable the combination of ZnO nanoparticles treatment with irradiation. The irradiation might be UV light, visible light used in photodynamic therapy (PDT), or gamma-irradiation used in radiotherapy. Several *in vitro* experiments have shown promising findings [65–71]. Because of the irradiation energy, the cytotoxicity of ZnO NPs increases which might be due to an increased ROS generation. It has already been shown that g-irradiation improves the antimicrobial activity of ZnO NPs [72], which is another indication that the combination of some kind of irradiation may increase the anti-cancer effects of ZnO NPs.

Numerous recent reviews on the anti-cancer property of ZnO NPs have shown their vast prospective in biomedical applications [73,74]. Hemocompatibility of nanoparticles must be ensured to pave the way for translational research of ZnO NPs in clinics. This comprises their compatibility with erythrocytes, coagulation system, and the release from the immune system, which allows adequately long circulation times to reach the tumor site. The protein corona may affect active or passive targeting through the EPR effect to the tumor site [74]. In vivo studies were conducted with zinc oxide nanoparticles, mainly evaluating tissue distribution and circulation time. Intraperitoneal administration of ZnO NPs was done in mice models. It was observed that the nanoparticles had a quite broad tissue distribution and tended to accumulate in the spleen, lung, liver, kidney, and heart. After the injection, zinc serum levels reached maximum values in 6 h and remained high until 72 h. Elevation of zinc level in the brain was not observed, which suggested that the blood-brain barrier effectively blocks the nanoparticle's entry into the brain [75]. Similar biodistribution of intravenously injected ZnO NPs in mice was observed. ZnO NPs were found to be quickly removed from the bloodstream and gathered in the spleen, lung, kidney spleen, and liver. As an oxidative stress indicator, 8-oxo-20 -deoxyguanosine (8-oxo-dG) level in urine was found to be raised after ZnO NPs treatment, and pathological alterations were observed in the liver and lung [76]. Another report also found the changes in blood values and confirmed the existence of oxidative stresses [77].

2.7. Conventional drug delivery system

In a conventional drug delivery system, drugs are taken by the patients by injections or by oral and are not loaded into the carriers. Consequently, this traditional drug delivery system has specific problems. The main problem is that the drug is released rapidly (burst drug release) in a short

duration of time after being taken by the patient's body. This leads to the high drug concentration in vivo, which generally produces side effects in the patient. Moreover, this burst drug release at an early stage of drug administration results in a fast decrease in drug concentration in vivo in a short time, which is lesser than that required for effective treatment; this means the time of treatment of the drug is significantly shortened, as shown in Figure 2.2.

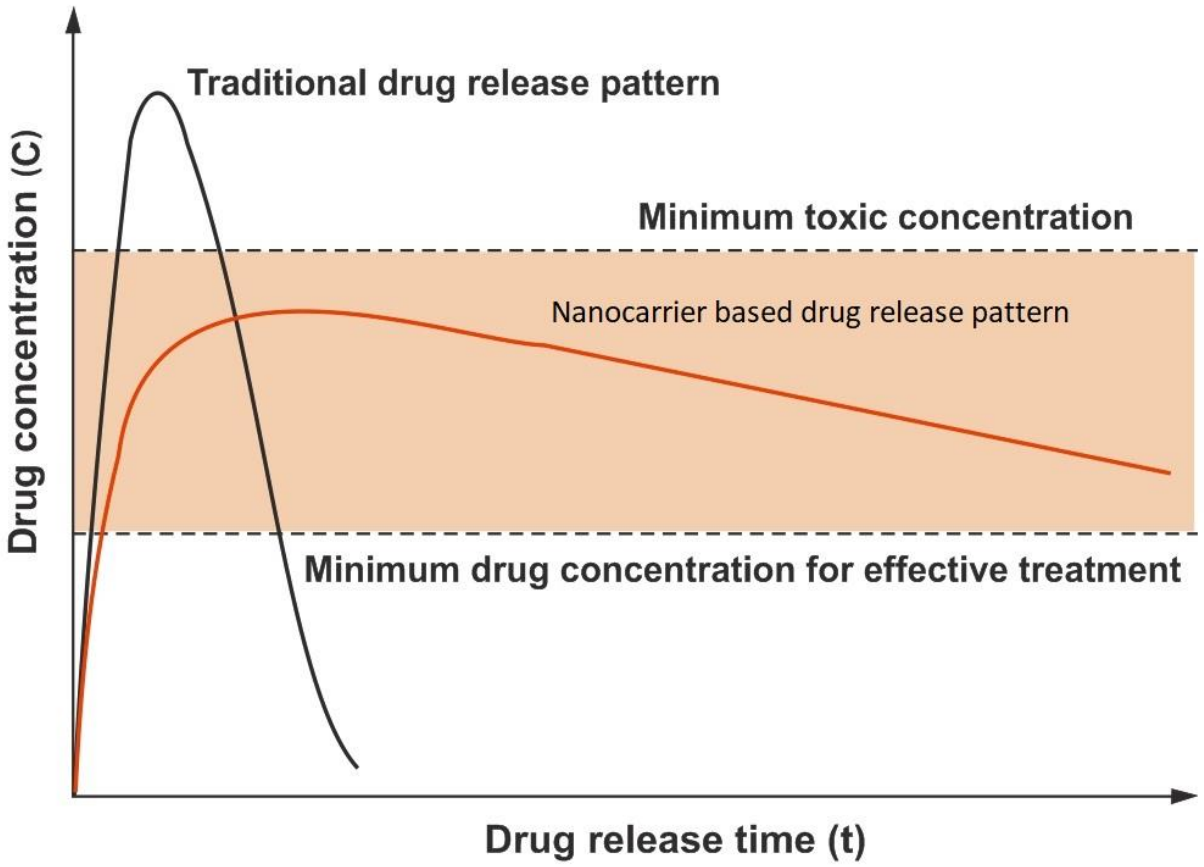

Figure 2.2: Comparison of the drug release patterns by the traditional drug delivery system and the nanocarrier drug delivery system.

Commercially available chemotherapeutics are non-targeted and cause severe toxicity in healthy vital organs such as the liver, heart, and kidney [78–80]. Furthermore, the consumption of appropriate drug concentration at the tumor site is limited because of the existence of drug resistance and the high drug efflux capacity of the cancer cells [81,82]. Consequently, side effects due to the nonspecific accumulation of these drugs are unavoidable. Thus, due to the low effect of conventional therapies

at the tumor site, it is extremely important to find new therapeutic targets which have the potential for selective killing of cancer cells without being toxic to the normal tissues.

2.7.1. Nanocarrier-based drug delivery system

The nanocarrier-based drug delivery system in which the drug is loaded onto nanocarriers is entirely different from the conventional drug delivery system without drug carriers. The drug molecules interact with the carrier material in the nanocarrier drug delivery system. Thus, as the patient takes the nanocarrier drug delivery system, the drug is released from the nanocarrier slowly and lasts for a long time. This results in controlled and sustained drug release.

In the early phase, the drug is released with a comparatively large speed, and the drug concentration reaches above the minimum concentration necessary for effective treatment. After that, the drug is continuously released to maintain the drug concentration needed for effective treatment. Hence, the nanocarrier-based drug delivery system has a prolonged and sustained drug release time which can avoid the side effects of the traditional drug delivery system, as presented in Figure 2.2.

Drug nanocarriers should present the following functions:

1) Preventing drugs from being degraded by enzymes during circulation in vivo
2) Extending the drug circulation time to increase its bioavailability
3) Eluding the early and burst release of drugs to decrease side effects
4) Supporting the sustained drug release to prolong the action time of drugs
5) Recognizing the active targeting delivery of drugs, enhancing drug utilization, avoiding drug side effects to normal body tissues and organs. Therefore, nanocarriers reduce the dosage of drugs, control the release of the drug, and prolong drug release time. These carriers also increase the drug bioavailability, reduce damage caused by the drugs to normal tissues, increase drug efficacy, and reduce side effects [83].

2.7.2. ZnO nanoparticles for targeted drug delivery

ZnO NPs have been considered a potential candidate for targeted drug delivery owing to their ease of synthesis, cost-effective precursors, biocompatibility, and cellular internalization via endocytosis [84]. Another distinctive benefit of ZnO NPs is that they can be available in different nanostructure forms such as nanorods, nanosheets, nanospheres, nanobelt, and quantum dots [85].

The numerous kind of interactions involved in nanoparticles-mediated targeted drug delivery are ligand-receptor recognition, coulombic and hydrophobic interactions [86]. In addition, to control the release process, different responding conditions have been employed; these comprise temperature [87], pH [88], and light [89]. As pH values in tumor tissues are significantly lower than those in normal tissues and blood, pH-responsive drug delivery systems have special advantages in their suitable operation and simple design. As a kind of pH-responsive drug carrier, ZnO nanomaterials were proposed first in 2010 [90], and these materials have been developed rapidly in the past years [91–93].

ZnO NPs show reduced toxicity and enhanced biocompatibility towards the body's normal cells, being zinc as a trace element in the body. ZnO NPs dissolute rapidly to Zn^{2+} ions at lower pH of as 5.5 which is similar to the acidic tumor microenvironment. It enables ZnO NPs to show the cytotoxic effect on tumor cells through ROS explosion, lipid peroxidation, mitochondrial dysfunction, DNA damage, and end with apoptosis [94].

2.8. Doxorubicin (DOX)

Doxorubicin (DOX) has been considered one of the most effective chemotherapeutic anticancer drugs of the past 50 years. Doxorubicin has shown great treatment potential for several cancer types such as breast cancer [95], Kaposi's sarcoma [96] and ovarian carcinoma [97]. DOX is regarded as one of the most effective chemotherapeutic drugs approved by the Food and Drug Administration (FDA) [98]. DOX can combat rapidly dividing cells and slow disease progression, and it has been widely recognized for several decades. Doxorubicin is a nonselective class I anthracycline drug, owning sugar and aglyconic moieties. The aglycone is composed of a methoxy carbonyl group following the substituent tetracyclic ring with quinine-hydroquinone adjacent groups. The sugar element (daunosamine) is attached to one of the rings via a glycosidic bond composed of a 3-amino-2,3,4-trideoxy-L-fucosyl moiety [99]. DOX is limited only by its toxicity on noncancerous cells in the human body. The high efficacy of DOX is also accompanied by high systemic toxicity toward healthy tissues. Doxorubicin is highly toxic, especially to the heart and the kidneys, limiting its therapeutic applications. Therefore, new drug-delivery strategies for DOX are urgently needed. To reduce the toxicity of Doxorubicin, targeted delivery of the drug through zinc oxide nanoparticles is an alternative choice for breast cancer therapy.

2.9. An overview of ZnO based Doxorubicin delivery systems

The applications of ZnO NPs as drug delivery systems are described in various research reports [91,93,100–106]. So far, most of the researchers have used several ZnO NPs-based smart drug delivery systems for the targeted delivery of doxorubicin in cancer cells. Muhammad et al. [91] studied the use of ZnO quantum dots (QDs) as a pH-responsive system. This system was pore-blocker of doxorubicin (DOX)-loaded mesoporous silica nanoparticles (MSN). Mitra et al. [100] developed the porous ZnO nanorods functionalized with folic acid for targeted and pH-responsive delivery of Doxorubicin. The nano rods -loaded with DOX demonstrated higher cytotoxicity compared to that of the free drug due to effective intracellular uptake in MDA-MB-231 cells.

Zhang et al. [93] developed a biocompatible and biodegradable core-shell ZnO@polymer nanocarrier for pH-responsive DOX release in human glioblastoma U251 cells. DOX-loaded ZnO@polymer quantum dots can effectively cross the U251 cell membrane through endocytosis and decompose within the endosomes or lysosomes, leading to the release of DOX. Tan et al. [101] developed a novel nanohybrid based on ZnO@ poly(N-isopropylacrylamide) for temperature and pH-responsive release DOX. They used N-isopropylacrylamide as a thermally responsive material that undergoes shrinkage of structure upon heating which leads to the DOX release from its surface. Also, low pH enables the dissolution of ZnO core, and as a result, trapped DOX is released.

Cai et al. [102] reported hyalurolic acid (HA) functionalized ZnO quantum dots for pH-responsive delivery of DOX in A549 cells. DOX was loaded onto the surface of ZnO quantum dots. Release of the DOX via rupture of the metal-DOX complex occurred because of the dissolution of ZnO NPs in the acidic intracellular environment. It was found that HA functionalized ZnO-QD-DOX exhibited higher cytotoxicity than non-functionalized ZnO-QD-DOX due to improved cellular uptake.

Zheng et al. [103] established a core-shell nanocarriers (ZnO-DOX@ZIF-8) using mesoporous zinc oxide as core and microporous zeolitic imidazolate frameworks (ZIF-8) as a shell for pH-responsive delivery of DOX. The mesoporous ZnO core worked as a drug storage reservoir, while ZIF-8 functions as a stable shell that avoids premature drug release at physiological pH. ZnO-DOX@ZIF-8 was internalized by A549 cancer cells, and DOX was released by ZnO dissolution and ZIF-8 decomposition under acidic intracellular conditions. Also, ZnO-DOX@ZIF-8 displayed synergistic anticancer activity by ROS generation due to ZnO.

Dine et al. [104] utilized the fluorescent ZnO-copolymer core-shell quantum dots using ZnO QDs as core and the copolymer of oligo (ethylene glycol) methacrylate (OEGMA) and 2-(2-methoxyethoxy) ethyl methacrylate (MEO2MA) as a shell for thermoresponsive and pH mediated DOX delivery system. The polymeric shell encapsulated the drug and delivered it under the influence of stimuli. The DOX-loaded ZnO-copolymer QDs exhibited higher cytotoxic effects in HT29 cells than free DOX because of effective cellular uptake and DOX release into cytosol due to ZnO QDs dissolution at physiological temperature. Nevertheless, the higher cytotoxicity of DOX-loaded ZnO-copolymer QDs under heating conditions can be ascribed to the improved DOX release through a phase change of copolymer from expanded to breakdown state.

Yang et al. [105] developed an arginine-glycine-aspartate (RGD) peptide-conjugated ZnO nanoparticles drug delivery system for targeted cancer therapy. DOX was loaded onto ZnO NPs surface. Following up taken by the U87MG cells, ZnO-based nanocarrier exhibited a pH-responsive drug release.

Chen et al. [106] developed a biodegradable and pH-responsive mesoporous silica nanoparticles (MSN) based drug delivery system capped with ZnO quantum dots. After loading DOX inside the mesopores of MSN, ZnO QDs sealed the pores of MSN through a covalent bond. After the internalization into 4T1 cells, the ZnO QD lids were dissolved quickly in the acidic intracellular compartment, which led to the DOX release into the cytosol. The developed ZnO QD capped MSN-based drug delivery system presented a synergistic anticancer effect in 4T1 cells.

2.10. State of the art syntheses of zinc peroxide nanoparticles (ZnO_2 NPs)

This study focused on zinc peroxide nanoparticles' anti-cancer activity. A new, simple, reproducible, and fast synthesis approach was developed in a previous study (see section 2.12). According to the literature, various synthesis approaches have already been established.

Bai et al. synthesized ZnO_2 nanoparticles by using a green hydrothermal technique. An aqueous solution containing only ZnO powder and a 30 % H_2O_2 solution was autoclaved in a Teflon-lined stainless steel autoclave. The obtained particles were found to have an average diameter of 12 nm obtained through the XRD spectrum, and it was observed that the reaction temperature from 80 °C to 140 °C was essential for attaining pure cubic phase nanoparticles [107].

Drmosh et al. [108] produced zinc per oxide nanoparticles via laser ablation method. A zinc plate was irradiated through an Nd-YAG laser (wavelength of 355 nm). This resulted in the production of ZnO_2 nanoparticles with a diameter of 3-4 nm. They utilized different surfactants such as Cetyltrimethylammonium bromide (CTAB) and Sodium dodecyl sulfate (SDS) and examined their influence on the morphology and the particle size.

Sun et al. [109] developed a sol-gel synthesis method. The starting materials were zinc acetate dihydrate and 30 % hydrogen peroxide dissolved in water. A 35W Xenon lamp was used to initiate the production of ZnO_2. The lamp had a comparable energy distribution as normal sunlight, which was desirable to convert the precursor zinc acetate to zinc peroxide. The zinc acetate dihydrate and 30 % hydrogen peroxide mixture were irradiated for 6 h with continuous stirring to get a ZnO_2 precursor sol with an average particle size of 68 nm. After 48h of aging, sol was baked at 40 °C overnight. This resulted in a fine ZnO_2 powder after crushing. It was also possible to change the obtained product by changing the parameters like reaction time and temperature. Moreover, it was observed that by raising the sintering temperature over 200 °C, the zinc peroxide was transformed into pure zinc oxide with high crystallinity.

Chen et al. [110] used an organometallic precursor to synthesize zinc peroxide nanoparticles. They used $ZnCl_2$ dissolved in Tetrahydrofuran (THF) containing 1-octylamine and $Mg(C_6H_{11})Cl$. This solution was baked at 323 K for two days, followed by adding H_2O_2 which helped in dispersing the precipitate. The acquired product was separated by centrifugation and dried at room temperature. The particle size was found to be 3.1 nm.

Toib et al. [111] developed zinc peroxide nanoparticles by a simple oxidation-hydrolysis-precipitation approach. They utilized zinc acetate as starting precursor along with H_2O_2 as an oxidizer. Water was used as a hydrolysis source and solvent. Moreover, nanoparticles were stabilized by using the surfactant polyethylene glycol 200 (PEG 200). The reaction was conducted for two hours at room temperature. The precipitates of zinc peroxide were obtained by adding Sodium Hydroxide resulting in a colorless to a yellowish solution. It was observed that the particle size varied with the content of PEG 200 and it was changed from 193 to 19 nm.

Yang et al. [112] established another simple and green synthesis method by using hydrozincite ($Zn_5(CO_3)_2(OH)_6$) powder as a precursor, which was oxidized with a 30 wt% hydrogen peroxide solution. The reaction was continued for 24 to 72 hours. The formed ZnO_2 precipitates were separated by centrifugation. The particle size was found to be between 3.1 to 4.2 nm, which was

calculated by the Scherrer equation. However, TEM images exhibited mainly nanoparticle aggregates. It was also observed that the reaction conditions mentioned above were only valid for the hydrozincite precursor, and experiments performed with zinc oxide as precursor did not result in zinc peroxide particles.

2.11. Properties and common applications of zinc peroxide nanoparticles

Zinc peroxide crystallizes in cubic structure comprises an array of uneven octahedral containing a zinc ion (Zn^{2+}) at its center. This octahedral is surrounded by four oxygen ions (O-) placed at the each corner of the polyhedron. Furthermore, the interatomic distance between two oxygen atoms is 1.47 Å long. This typical structure causes local charge disbalance of sites, causing a structural variability towards temperature. This phenomenon describes the comparatively low decomposition temperature (around 190 °C) determined through thermogravimetry [113–116].

Also, zinc peroxide has a band gap of 3.3 to 4.6 eV, which makes this material motivating for semi conductor applications. Additionally, zinc peroxide can decompose in an aqueous acidic medium into Zn^{2+} ions and hydrogen peroxide (H_2O_2) [117,118]. This property makes zinc peroxide nanoparticles appropriate for biomedical applications [119].

Ali et al. [120] designed and characterized ZnO_2 NPs as a novel antimicrobial, anti-keratinase, anti-elastase, and anti-inflammatory materials fighting against polymicrobial multi-drug resistance (MDR) pathogens of burn wound infections. Their findings provided scientific confirmation to support the clinical applications of ZnO_2 NPs. These nanoparticles are potent candidate for the development of an anti-inflammatory agent. In vivo histopathological results indicated that ZnO_2-nanoparticles might be effective as proficient antimicrobial agents against *A. niger and P. aeruginosa* inhabiting burn wounds. However, further investigations are still required on human volunteers having skin burns to endorse the effectiveness of ZnO_2 NPs as a novel antimicrobial drug in wound healing, particularly after the successful treatment of ZnO_2-NPs in the burn wounds of the trial animal models.

2.12. Dynamic underwater chemistry for the synthesis of size-tailored zinc per oxide nanoparticles

Elbahri et al. [121] utilized dynamic underwater chemistry for the synthesis of size-tailored zinc per oxide nanoparticles for the first time. They have demonstrated the Leidenfrost dynamic chemistry

taking place in an underwater overheated restrained zone as a novel tool for the tailored generation of zinc per oxide nanoclusters (Figure 2.3). These nanoparticles were investigated regarding their cytotoxicity on different healthy and cancer cell suspensions. Their research could lead to the utilization of dynamic green nanochemistry in the facile and scalable synthesis of size-tailored nanoparticles for cancer applications. They have explored the potential of synthesized monodisperse ZnO_2 particles in treating complex diseases such as cancer. The related studies have proved that nanoparticles cytotoxicity against cancer cells is influenced not only by the size but also by the metabolic activities of the cells. Accordingly, they executed a series of early experiments to find out the impact of ZnO_2 nanoparticles synthesized by Leidenfrost dynamic chemistry on the survival of various cancer cells as well as normal, healthy cells.

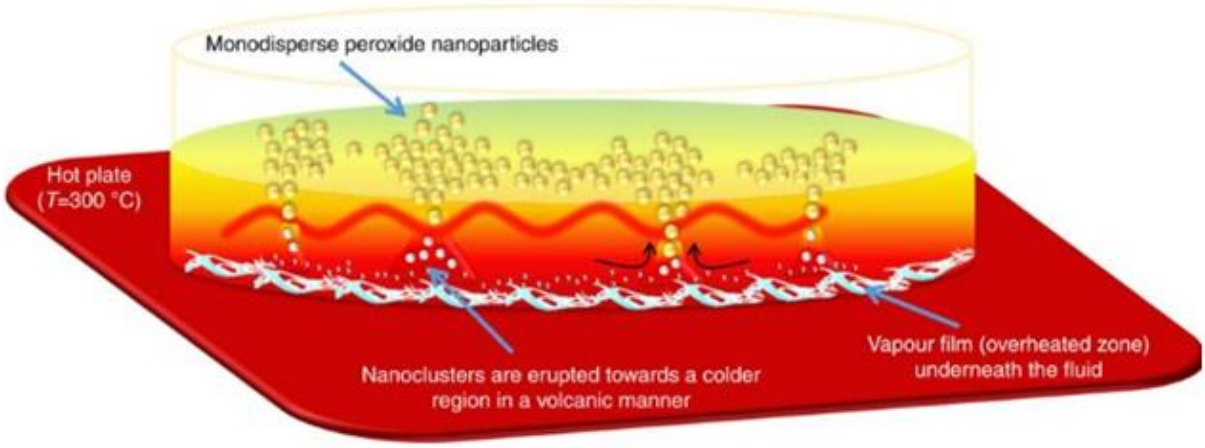

Figure 2.3: The schematic shows that when nanochemistry occurs at the overheated zone, the formed nanoparticles assembled as nanoclusters erupt towards the much colder region for further growth. This tendency can be controlled and utilized for tailoring the size [121].

Primarily, they have explored the influence of ZnO_2 nanoparticles of different sizes on cancer cells (U937 lymphoma cells, leukaemic Jurkat T cells). They have also investigated the effect of zinc peroxide nanoparticles on adherent tumor cell lines (Panc89 (human pancreatic adenocarcinoma), HT29 (human colorectal carcinoma), and L929Ts (murine fibrosarcoma)) in comparison to healthy peripheral blood mononuclear cells (PBMCs). Concentration and size-dependent cytotoxicity profiles for the aforementioned cell lines were determined. Loss of membrane integrity was measured as the indicator of cell death, determined by uptake of membrane-impermeable dye—propidium iodide. The results obtained for the suspension cells and adherent cell lines are shown

in Figure 2.4 (a–f). As can be seen in the figures, the cytotoxic behavior of the ZnO_2 nanoparticles mainly depends on the particle size and the cell type used in the experiment.

With cell suspensions such as U937, Jurkat and PBMCs, the particle of size 126 nm produced a more prominent toxic effect and triggered more cell death than the 426 nm-sized particles (Figure 2.4 a–c). However, for adherent cells such as HT29 and Panc89, the smaller nanoparticles presented a more significant toxic effect at concentrations above 200 µg/ml. At concentrations below or equal 200 µg/ ml, the particles of size 426 nm were found to produce a more cytotoxic effect. For the cell suspension murine L929Ts, the larger particles were more toxic to the cells irrespective of the concentration of nanoparticles. 426 nm sized ZnO_2 nanoparticles were less toxic to healthy PBMCs when compared with L929Ts or U937 cells. However, for HT29, Jurkat, and Panc89 cells, the cytotoxic effect produced by both (126 nm and 426 nm-sized) nanoparticles was equivalent to that for the PBMC cells (Figure 2.4 a, d, e versus b).

Overall, their experiments showed that ZnO_2 nanoparticles have the potential to kill cancer cells by both apoptotic and non-apoptotic mechanisms. The efficiency of damaging the cells seemed to depend on the particle size and type of the inspected cancer cell. It was also notable that healthy PBMCs were inclined to the negligible cytotoxic impact of the 426 nm sized ZnO_2 nanoparticles at 50 µg/ml compared to specific cancer cells like L929Ts.

Considering the cytotoxic effect of these ZnO_2 nanoparticles against various cancer cells, here, in this study, we further investigated the cytotoxic effect of these nanoparticles on human breast cancer cells (MCF-7) and healthy fibroblasts (RMF-EG).

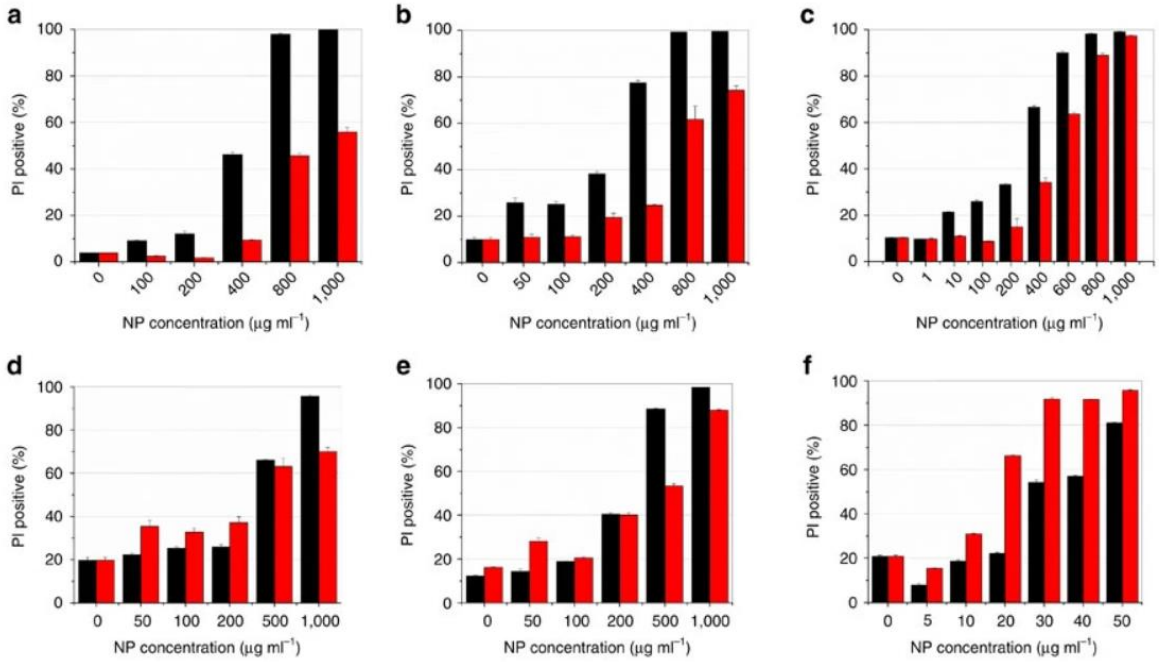

Figure 2.4: Cell mortality induced by cytotoxic effect of ZnO_2 nanoparticles. Flow cytometric analysis of cells (a) Jurkat ATCC, (b) PBMC, (c) U937, (d) HT29, (e) Panc89, (f) L929Ts stained with PI (PI-positive fraction) treated with the 126 and 426 nm ZnO_2 nanoparticles (black and red columns, respectively) at various concentrations for 24 h. '0' concentration represents blank samples containing the cell culture media but in absence of ZnO_2 nanoparticles [121]

2.13. Flame transport synthesis (FTS) of tetrapodal ZnO micro-nano structures

ZnO has main advantages of biocompatibility, cost-effective availability, and simple fabrication of different micro and nanostructures. The structure of ZnO in (Figure 2.5) has been utilized for various applications [122–124]. The ZnO tetrapods (T-ZnO) used in this work were synthesized by an already introduced flame transport synthesis (FTS) technique [125,126]. This technique gives the advantage of its (T-ZnO) versatile synthesis with dimensions ranging from nanoscale to microscale. T-ZnO can be scaled up (up to kilograms) very easily in a very effective manner. The T-ZnO particles produced by the FTS are shown in Figure 2.5.

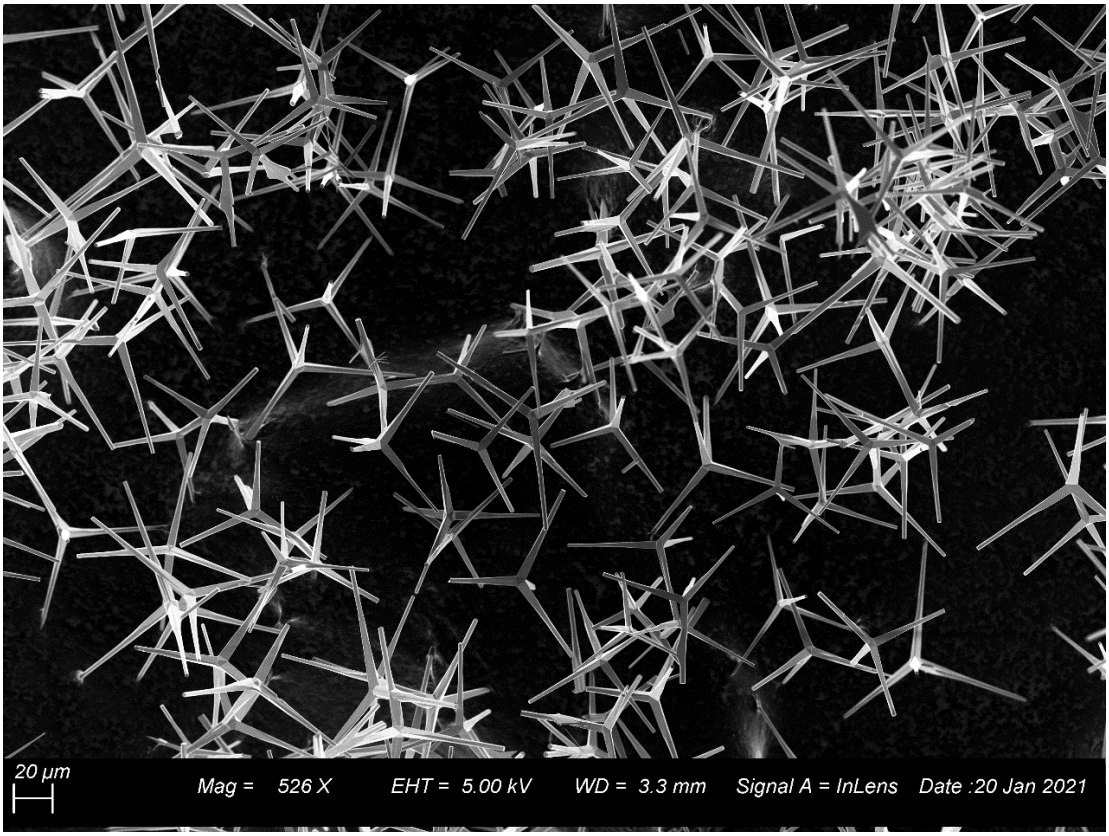

Figure 2.5: Three-dimensional T-ZnO particles produced by the Flame Transport Synthesis (FTS)

These T-ZnO have already revealed their potential for the strong blocking capability of viral (herpes simplex virus type-1 and type- 2 (HSV-1 and HSV-2)) entry into the cells [127,128]. The presence of T-ZnO decreased the viral entry into cells because some of the viruses are trapped by T-ZnO. Illumination of these structures with UV light enhanced their virus trapping ability and thus, an additional decrease in viral entry into the cells was detected [127,128]. Trapping of HSV-1 and HSV-2 by T-ZnO has been shown to prevent HSV-1 and HSV-2 infections *in-vitro*. Thus, T-ZnO seems to be a very promising prophylactic agent for preventing HSV-1 and HSV-2 infection *in-vivo* [127–129]. Therefore, cytocompatibility of these T-ZnO for different biomedical applications is a generally crucial issue that must be examined in detail.

To get a better understanding of the parameters that affect the cytotoxicity of T-ZnO in-vitro, Papavlassopoulos et al. [130] performed a detailed analysis of different material properties (crushing and oxygen pre-treatment) as well as various cell culture conditions that can affect the tetrapods biocompatibility using the human dermal fibroblasts (NHDF) as target cells. Main cell culture

conditions that can influence the tetrapod's toxic potency are cell to cell contact, cell density, age of the cells, and stage of cell growth of NHDF. In the current study, we further investigated the cytotoxic effect of T-ZnO (as prepared, crushed, and O_2-treated) on human breast cancer cells (MCF-7) and healthy fibroblasts (RMF-EG) by using ApoLive-Glo™ Multiplex Assay.

2.14. MCF-7 Breast Cancer Cells

In cancer research, cell lines are widely used in many aspects, particularly as *in vitro* models and seem to be a key component for the molecular diagnosis of breast cancer [131]. MCF-7 cells represent a very important candidate for breast cancer because they are used worldwide in research for estrogen receptor (ER)-positive breast cancer cell experiments. MCF-7 is the cell line that has been proliferated for many years by many groups [132]. It has proved to be a suitable model cell line for breast cancer research, including the investigations regarding anticancer drugs [133]. Over time, MCF-7 produced more useful knowledge data for patient care than any other breast cancer cell line [134]. MCF-7 is a non-invasive and poorly-aggressive cell line [135], which is considered to have low metastatic potential. Though frequently treated as a single entity, the human breast MCF-7 consists of numerous individual phenotypes, which constitute merely small proportions of the total population. These phenotypes may vary in receptor expression, gene expression profile, and signaling pathway. Despite variations in the proliferation rate of each phenotype, a balance between multiple phenotypes is maintained during progressive culturing of the line, possibly by some signaling cooperation.

2.14.1. Uses of MCF-7

Because MCF-7 cell line holds many ideal features, particularly to the mammary epithelium, they are very advantageous for in vitro breast cancer studies. These valuable features include the ability of MCF-7 cells to process estrogen in the form of estradiol via estrogen receptors in the cell cytoplasm, which makes MCF-7 an estrogen receptor (ER) positive cell line. MCF-7 is also a HER2 negative and progesterone receptor-positive cell line. MCF-7 cells are commonly used in research related to estrogen receptor (ER)-positive breast cancer cell experiments and several subclones representing different classes of ER+ tumors with receptor's varying expression levels.

2.14.2. Characteristics of MCF-7

MCF-7 cells are sensitive to cytokeratin along with holding estrogen sensitivity. They are intolerant to endothelin, vimentin, and desmin. MCF-7 cells are epithelial-like and grow in monolayers. The cell line can form domes and process estradiol through cytoplasmic estrogen receptors when grown in vitro. It is found that even though MCF-7 cells are easy to proliferate, they are usually a slow-growing population. Typically, MCF-7 doubling time is 30-40 hours. With a typical size of 20-25 microns, MCF-7 cells are pretty large adherent cells [136].

2.14.3. Cell culture

MCF-7 human breast cancer cells are usually seeded in T75 flasks with 1×10^6 cells/flask. They are grown in low glucose Dulbecco's modified Eagle's medium (DMEM) containing 2 mM glutamine, 10 % fetal bovine serum (FBS), 1% penicillin/streptomycin, and 0.01 mg/ml insulin. These cells need to be incubated in a 5 % CO_2 atmosphere at 37 °C. The medium renewal should be performed two times a week. Also, cells should be passaged weekly at a sub-cultivation ratio of 1:3.

2.14.4. Stability of MCF-7

Originally, MCF-7 cell line was defined as having a karyotype comprising 85 chromosomes. Today's MCF-7 cell line has a modal chromosome number of 82. Moreover, genetic inconsistencies are also present between the MCF-7 cell line from the ATCC cell line and Michigan Cancer Foundation.

2.15. RMF-EG cells

A fibroblast is a particular type of connective tissue cell present in tendons, skin, and other tough tissues of the body secreting collagen. They can be grown in a laboratory and thus studied for genotypes and phenotypes mainly related to diseases. Fibroblasts are principal active cells of connective tissues. Fibroblasts are flat, large, elongated (spindle-shaped) cells (Figure 2.6) having processes spreading out from the cell body ends. The nucleus of the cell is flat and oval. Fibroblasts generate tropocollagen, the portent of collagen, and an amorphous gel-like matrix that fills the spaces between fibers and cells in connective tissue. Fibroblasts display a significant role in the wound healing process, and this action is considered to be regulated by cells

called fibrocytes located in the tissue stroma. As a result of tissue injury, fibroblasts transfer to the damage site, depositing new collagen and assisting wound healing.

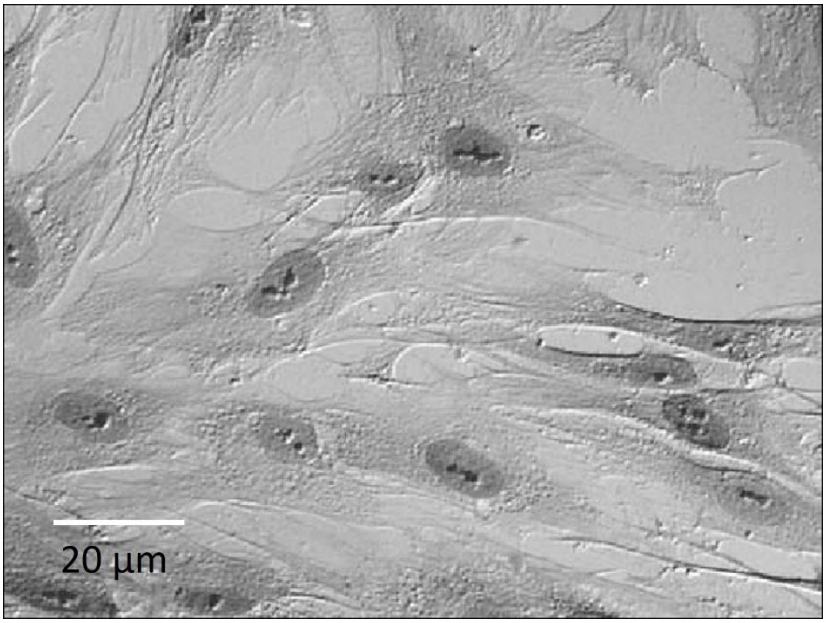

Figure 2.6: A microscopic image of elongated spindle-shaped human breast fibroblasts of size around 30-35 µm (RMF-EG) taken at ×40

Mammary fibroblasts (MF) or RMF-EG create constituents of the stromal extracellular matrix of the mammary gland. More significantly, these stromal extracellular matrix adjusts the differentiation and proliferation of mammary epithelial cells by inducing their gene expression. Furthermore, mammary fibroblasts show their part in engaging macrophages for immune surveillance, which is associated with a supportive mammary microenvironment for tumor cell progression. This progression recommends that MF play an exciting, helpful part in breast cancer invasion and development.

Chapter 3: Theory of Materials and Methods

This section provides a theoretical background on the analytical methods employed within the given work. Further extensive information on the following topics is discussed: Scanning Electron Microscopy, RAMAN Spectroscopy, X-ray diffraction analysis, UV-visible spectroscopy, Transmission Electron Microscopy, optical microscopy, microplate reader, and flow cytometry.

3.1. ApoLive-Glo™ Multiplex Assay for cell culture

The ApoLive-Glo™ Multiplex Assay combines the chemistry of two assays to evaluate viability and caspase initiation actions inside a single assay well. The first part of the assay assesses the cell viability's protease marker activity. The living-cell protease activity is constrained to cells that are viable and intact and is evaluated by using a cell-permeant, fluorogenic, peptide substrate (glycyl-phenylalanyl-amino fluorocoumarin (GF-AFC). This substrate can enter intact cells, where it is cleaved by the live-cell protease action to produce a fluorescent signal proportionate to the number of living cells (Figure 3.1). This protease of the living cell becomes inactive upon integrity loss of cell membrane and outflow into the contiguous culture medium [137]. The assay second part utilizes the Caspase-Glo® Assay technology to identify caspase-3/7 activation (a key biomarker of apoptosis). However, this second part is beyond the scope of the current study.

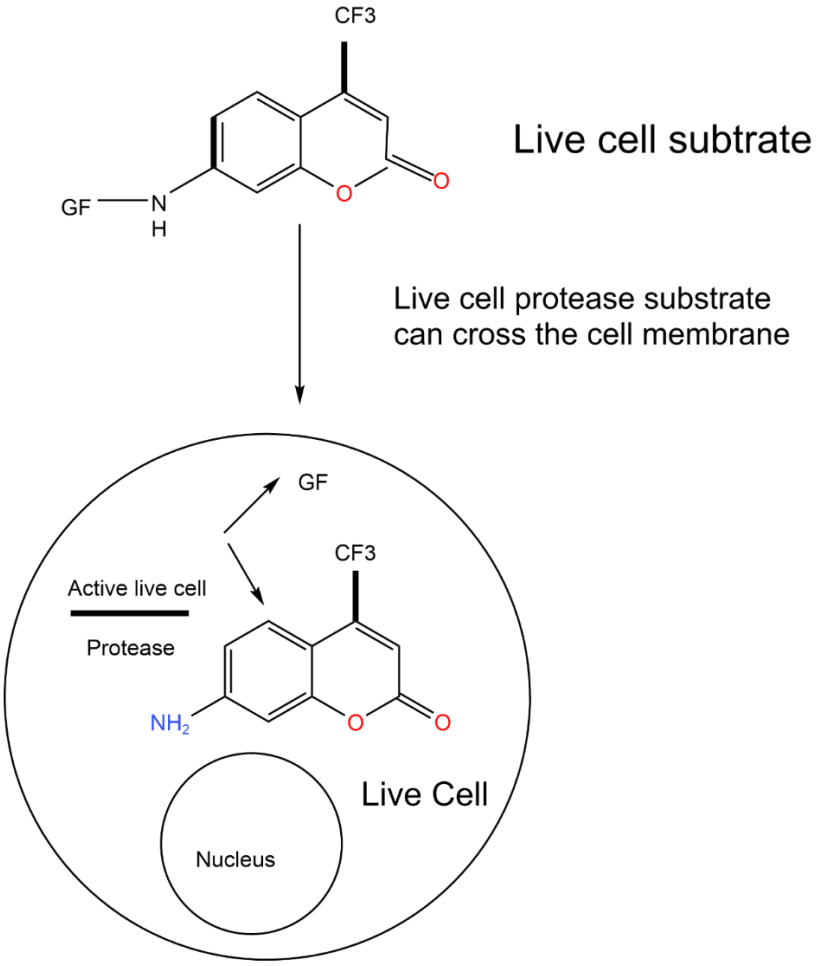

Figure 3.1: Cell viability assay chemistry. The cell-permeant substrate enters the cell, where it is cleaved by the live-cell protease activity to produce the fluorescent AFC.

3.1.1. Advantages of the ApoLive-Glo™ Multiplex Assay:

• **Measurement of viability and apoptosis inside the same sample well:** Precise determination of the cell death mechanism in less time with a smaller amount of sample.

• **Ease of implementation**: The assay procedure contains a simple sequential "add-mix-read" format (Figure 3.2).

• **Normalization of caspase data with viability control**: The caspase activity to viable cells ratio is advantageous to normalizing the cell numbers and determining the extent of caspase activation.

• **Flexibility and ease of automation**: The volumes of all assay components could be scaled to meet quantity needs, and the assay is responsive to automation in 96- and 384-well plates.

• Make known cell death even if the window of caspase activity is missed

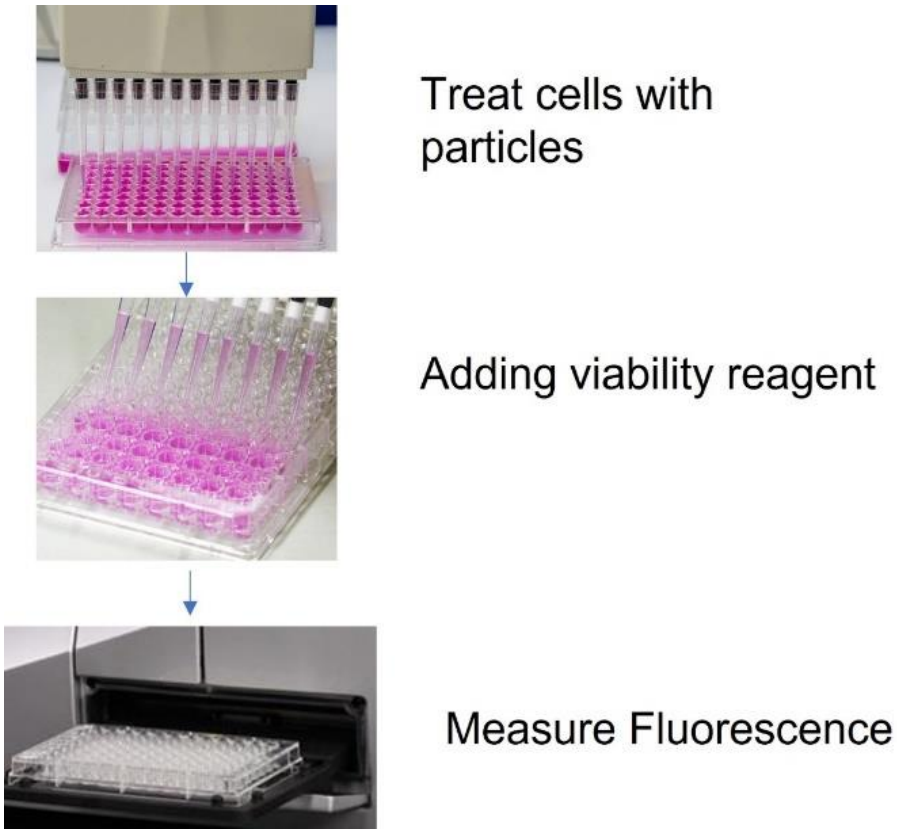

Figure 3.2: Schematic diagram of the ApoLive-Glo™ Multiplex Assay. Cell viability fluorescence is measured at $400_{Ex}/505_{Em}$.

3.1.2. Reagent preparation and storage

- Transfer the GF-AFC Substrate contents into assay buffer
- For 96-well plates, transfer 10 µl of the substrate into 2 ml of assay buffer
- For 384-well plates, transfer 10 µl of the substrate into 2.5 ml of assay buffer
- Mix the Assay Buffer comprising substrates contents by resuspending with micropippet until the substrate is thoroughly dissolved. This mixture is referred to as the viability reagent. The viability reagent can be used within 24 h after preparation and can be stored at room temperature. Unused viability reagent can be stored at 4 °C for 7 days without significant activity loss.

3.1.3. Controls

No-Cell Control: This control comprises the preparation of triplicate wells with medium but without cells to work as the negative control.

Untreated Cells Control: This control comprises the preparation of triplicate wells with untreated cells (without ZnO micro and nanoparticles) to serve as vehicle control.

Protocol

- 17.5 µl of viability reagent was added to all wells and briefly mix by orbital shaking (300–500 rpm for ~30 seconds).
- Well plates were incubated for 30 min and 60 min at 37 ºC.
- Fluorescence was measured at the following wavelength set: $400_{Ex}/505_{Em}$

The excitation and emission settings were set on a TECAN microplate reader (Infinite® 200 PRO) to excitation at 400 nm/emission at 505 nm.

3.2. Zinc ion release from ZnO and ZnO_2 micro and nanostructures

When ZnO nanoparticles interact with the cancer cells, they are taken up by the cell through endocytosis. Nanoparticles enter the cell through phagocytosis and pinocytosis bounded by endosomes and lysosomes. With the decreased pH level inside the cancer cell, the ZnO dissolution rate increases rapidly, causing lysosomal destabilization [138]. The pH of the early endosome is relatively low (around 6.3). It further drops to pH 5.5 in the late endosome. A rapid dissolution rate of ZnO at pH 4.7 at the lysosome causes lysosome destabilization. This destabilization suggests that a low pH value is necessary for the release of zinc ions. Hence the zinc ion release in blood or extracellular fluid (pH value of 7.4) is not favorable [26]. This process results in an increased release of zinc ions inside the cancer cell. The rise in intracellular zinc concentration induces zinc-dependent protein activity disequilibrium, resulting in their cytotoxicity towards the cancer cells. Increasing zinc ions also increases Reactive Oxygen Species (ROS) concentration, leading to cytotoxicity towards cells via oxidative stresses [22]. This selective cytotoxicity of ZnO against cancerous cells in *in vitro* conditions makes them a promising anticancer agent. The above findings motivated us to estimate zinc ions release from T-ZnO and ZnO_2 NPs to evaluate their anticancer activity.

3.2.1. UV-vis spectroscopy for determination of zinc ions

Among the suitable techniques for metal ions quantification, atomic absorption and emission spectroscopy and induce coupled plasma mass spectrometry are likely to be commonly employed [139]. Even though these techniques are sensitive and reliable, they have the limitation of being rather time-consuming (concerning sample preparation), costly (instrument acquirement and maintenance), and not always readily available [140,141]. Therefore, simple spectrophotometric techniques tending to be productive and cost-effective, are possible substitutes for those techniques requiring more sophisticated instrumentation.

Ultraviolet-visible (UV-vis) spectroscopy is a very significant analytical method in modern laboratories and has been widely used for many years. UV-vis spectroscopy is extensively applied to the solution form of metal complexes to determine metal concentration as a quantitative analysis method. The determination of trace metals by UV– vis spectroscopy usually depends on variations in the absorption spectrum of a chromophoric chelator upon binding the anticipated metal ion [142].

3.2.2. Zincon

Among the several reagents causing complexation-induced spectral changes, the formazan dye Zincon (Figure 3.3) is considered an excellent chromophore for quantifying zinc in an aqueous solution [142,143]. It is noteworthy that only one report [144] seems to belong to the utilization of Zincon as a spectrophotometric reagent for determining the metal content of a metalloprotein. A complete analysis was done to estimate the zinc ion content in different buffers containing zinc peroxide nanoparticles and tetrapodal zinc oxide in the current work. The influence of zinc ions on the absorption spectra of Zincon in its free and zinc-bound forms was estimated. As a consequence of this study, an optimized method that allows the facile determination of Zn^{2+} ions was obtained.

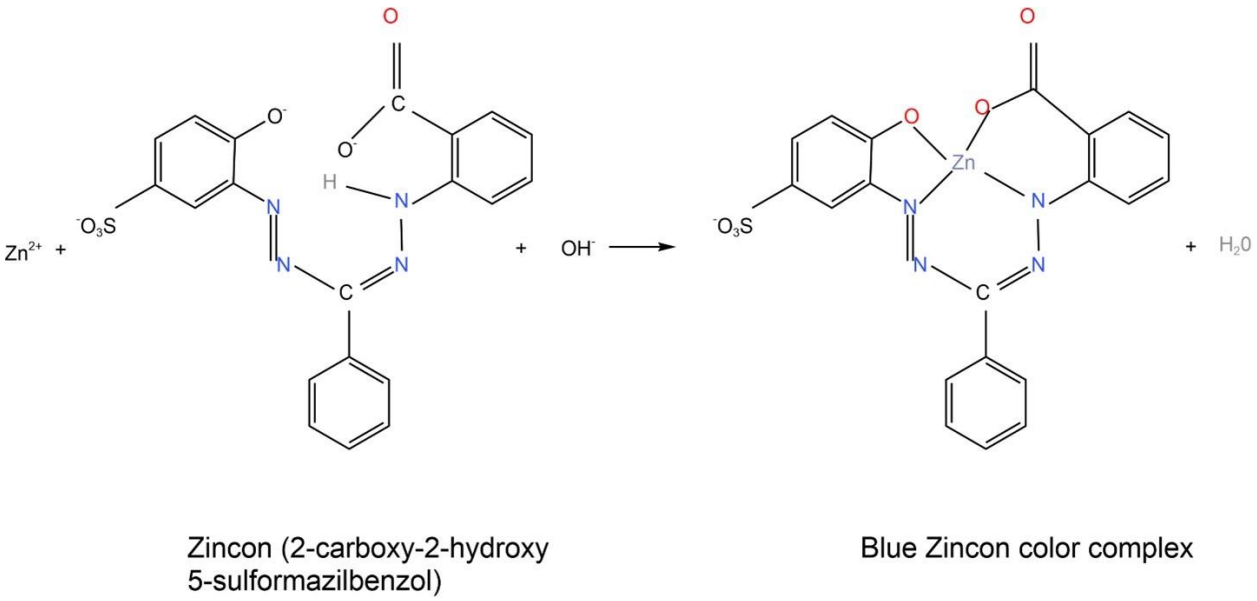

Figure 3.3: Structures of Zincon (2-carboxy-20 -hydroxy-50 -sulfoformazylbenzene) in its free and zinc-bound form.

3.3. Zinquin ethyl ester

Zn^{2+} ions release by ZnO_2 nanoparticles dissolution was estimated using flow cytometry, after labeling with Zinquin probe zinquin ethyl ester (Sigma Aldrich, Germany) (Figure 3.4), a UV excitable fluorescent zinc indicator (Ex 364 nm/Em 385 nm) [145]. Zinquin probe is a lipophilic compound that penetrates cell membranes and increases fluorescence signal upon binding Zn^{2+} ions.

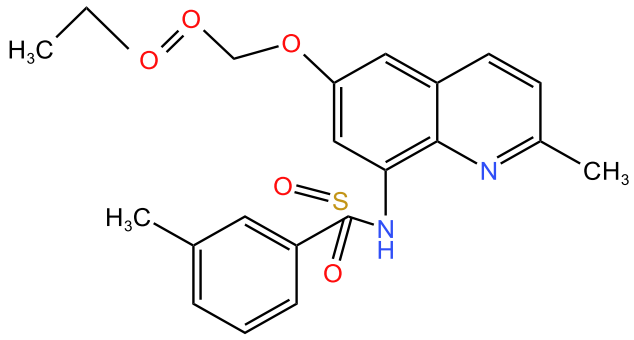

Figure 3.4: Chemical structure of zinquin ethyl ester

3.4. Flow cytometry

Flow Cytometry is a technique utilized to detect and measure chemical and physical characteristics of cells or particles population. In a typical procedure, cells or particles containing samples are suspended in a fluid and introduced into the **flow cytometer** instrument.

3.4.1. Purpose of flow cytometry

Flow cytometry offers a well-established methodology to identify cells present in solution. Most commonly, it is used for evaluating peripheral blood and other body fluids. Flow cytometry studies are used to identify and quantify immune cells and characterize hematological malignancies. Flow cytometer can measure cell size, granularity, DNA gene expression, intracellular proteins, and surface receptors. One of the key advantages of the flow cytometric process is its ability to perform the above-mentioned measurements quickly. They can calculate from three to six properties quantitated in a single sample for around 10,000 cells in less than one minute.

One of the main principles of using flow cytometry is its capability to investigate the complete cell cycle and evaluate DNA content in different phases. The monitoring process of the cell cycle's natural events provides information for disease diagnosis and therapy prognosis. The various phases of the cell cycle reveal altered DNA content and other irregularities, pointing out the presence of tumors or signs of advanced cell death. A specified flow cytometry software is used to store data expressions in a computer during analysis. Flow cytometry data are usually reported in two ways: **a dot plot or a histogram**.

3.4.2. Fluorescence-activated cell sorting (FACS)

Fluorescence-activated cell sorting (FACS) is a specific type of flow cytometry. It offers a method to sort a cell's heterogeneous mixture into two or more containers based on each cell's specific light scattering and fluorescent characteristics. It is different from flow cytometry because it provides unique characterization versus merely counting and sorting cells.

3.4.3. Multicolor flow cytometry

Multicolor flow cytometry is a valuable technique for examining mixed populations of cells, for example, blood and tissue cells in animal and human samples. Typically, a particular cell type is marked with fluorescent dye (markers) such as fluorophore, or propidium iodide. The capability

for using various fluorescent markers simultaneously allows the identification of different cell types, along with functional markers that can further characterize each sample. Different wavelengths of light emitted from the laser are used to measure these fluorescent markers and dyes.

Every marker is excited at a specific wavelength of light to distinguish them using multiple markers. Adjusting a distinctive staining panel from 4 to 6 colors to up to12 colors must be proceeded in an organized manner to attain effective parameters in a staining panel.

3.4.4. Applications of flow cytometry

Flow cytometry is essential in numerous clinical areas such as diagnosis, systemic disease (static or progressive), and treatment plans. Nowadays, researchers are very eager to learn more about the complications of certain diseases and conditions than ever before. It has directed to a rapid change in diagnosing patterned and radically improved medical methodologies to treat diseases, for instant, cancer.

3.5. Scanning electron microscopy (SEM)

Scanning electron microscopy (SEM) is a technique in which only a milligram quantity of material is used to determine particle size, shape, and texture. In SEM, a fine beam of electrons scans across the investigated sample in a series of parallel tracks. The electrons interact with the sample and generate numerous different signals, which can be identified and displayed on a cathode ray tube screen. Since the depth of focus is much greater than that of the light microscope, information on a surface texture can be produced. However, it is hard to generate a particle size distribution using SEM because only a few particles can be seen in the viewing field at one time. However, SEM used with other techniques, such as laser diffraction, provides valuable additional information on sample texture.

3.5.1. Working principle

The interaction of the high-energy electron beam with the sample produces signals of different types. These signals are obtained from specific emission volumes within the sample and are helpful in studying many characteristics of the sample like microstructure morphology, crystallography, and chemical composition.

Working of SEM

Creation of electron beam

Free electrons are generated at the cathode, which is a tungsten filament, and then accelerated through an electric field towards the sample at high speed.

Electron optics

Various lens systems are used to control the beam. These consist of charged coils to generate the magnetic field through which electrons are deflected. The condenser lenses and aperture have the function of bundling the beam, and the use of several lenses improves quality. The beam is deflected finally through the scanning coils and focused on a sharply defined point via objective (Figure 3.5).

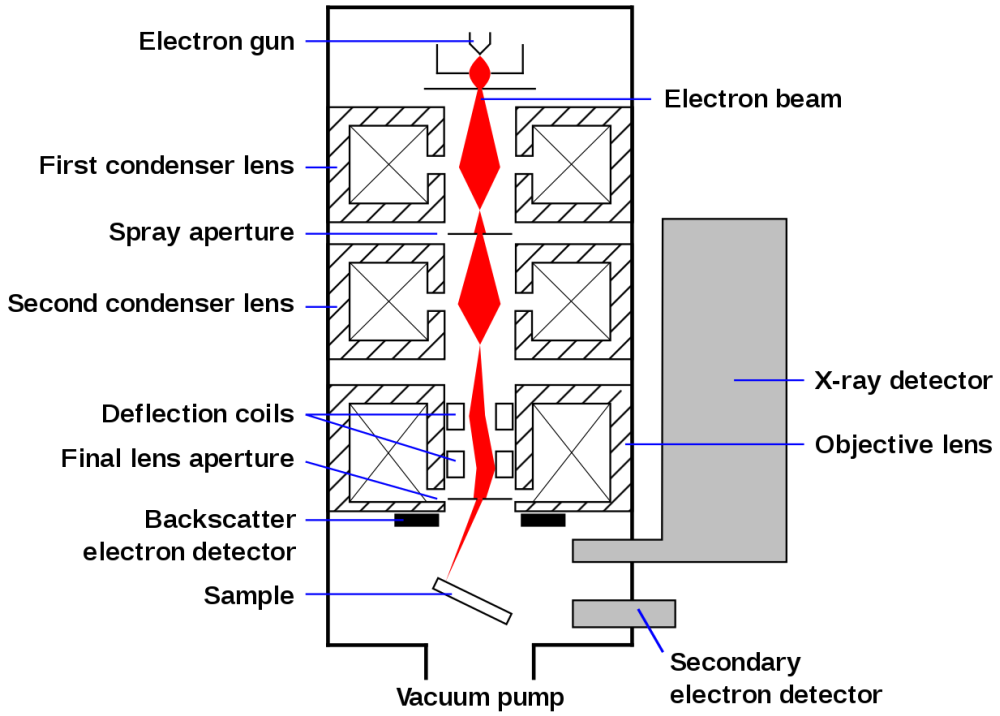

*Figure 3.5: Schematic and working of scanning electron microscope**

Interaction with probe

When the electron beam strikes the sample, various types of interactions occur. The interactions between the primary electron beam and specimen produce signals of different types, including secondary electrons, back scattered electrons, characteristics X- rays, auger electrons, and other photons of various energies [146]. Depending on the information to be collected, detectors of different types are used. By using the various signals produced, microscopic images are formed. The signal is detected and converted into an electrical signal which is amplified and then fed to the grid of a synchronously scanned cathode ray tube (CRD) display. The scan of the beam spot over the specimen surface results in a one-to-one correspondence between the picture points on CRT screen and the points of the specimen. Amplified signal modulates the brightness of CRT. As a result, variations in the strength of the detected signal cause variations in brightness on CRT screen (contrast on the micrograph) and an image of the specimen.

**This image was borrowed from Schema MEB (en) - Scanning electron microscope - Wikipedia, which is licensed under Creative Commons — Attribution-ShareAlike 4.0 International — CC BY-SA 4.0*

3.5.2. SEM modes

Back scattered electrons

As a result of the interaction of electrons with the specimen, two types of scattering mechanisms (elastic and inelastic scattering) occur. Elastic scattering of incident electrons by the nuclei of the atoms results in high energy back scattered electrons, and these back scattered electrons provide the atomic number contrast. They thus can provide qualitative information on compositional uniformity. Under appropriate conditions, these also provide crystallographic information. Inelastic scattering gives a variety of signals, such as secondary electrons emission, auger electrons, characteristic X-rays, cathode luminescence, and thermal effects.

Secondary electron imaging

Secondary electrons are low-energy electrons with energies less than 50 eV that originate within a few nanometers from the surface of material entered by a primary electron beam. This imaging mode is used for topographic features of solid surfaces and for analyzing the electric and magnetic fields present in the material.

Characteristic X-rays

These are emitted due to electronic transitions between the inner–core levels used to analyze a particular chemical element.

Electron acoustic modes

CC (charge -collection) and CL (cathode luminescence) modes provide the micro characterization of electronic properties of semiconductor and semiconductor devices. CL provides a contactless and nondestructive characterization tool in microanalysis. At the same time, in CC mode, electrical contacts are applied to a semiconductor device which allows the monitoring of electrical signal in the external circuit. Electron acoustic mode is used to detect the subsurface defects in solids [147].

3.5.3. Applications of SEM

- SEM has a variety of applications in several scientific and industry-related fields, especially where the characterization of solid materials is beneficial.

- It provides morphological, compositional, and topographical information. In addition, it can detect and analyze surface fractures, examine the surface contamination, reveal the spatial variations in chemical compositions, and provide qualitative chemical analysis.
- SEM has technological applications such as semiconductor inspection and assembly of microchips in computers.
- SEM is an essential research tool in nanotechnology, medical and forensic science and metallurgy.

3.6. RAMAN spectroscopy

RAMAN spectroscopy (RS) is a spectroscopic technique that uses a laser source to produce inelastic scattering of monochromatic light. During the interaction between light and specimen, the frequency of photons in monochromatic light alters through inelastic scattering.

Figure 3.6 shows the Raman system consists of four main components:

- A laser as an excitation source
- Specimen illuminating system and light assembly optics
- Selector of wavelength also known as filter
- A detector (An array of photodiodes)

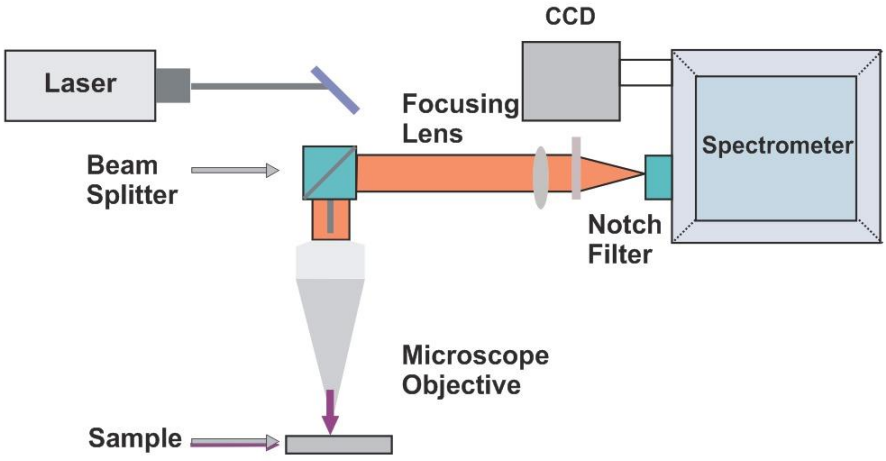

Figure 3.6: Schematic diagram of the sample, incident light and collection optics in the Raman spectrometer.

RS is an important fingerprint identification tool that differentiates the functional groups and chemical bonds of materials. Raman can be employed in qualitative and quantitative evaluation of chemical, biological, polymeric, and semiconducting materials. In the current research, RS is mainly used for investigating the chemical composition of different zinc oxide structures. In general, Raman Spectroscopy is also used for studying molecular vibration and rotation, which is primarily important in identifying the structure of material and molecular dynamics.

The sample absorbs laser light photons and reemits the photons of frequency moving up or down compared to the source monochromatic frequency. This phenomenon is called the Raman Effect. RS also detects the change in polarizability of a molecule. The Raman Effect is also correlated with the molecular deformations in an electric field (E), which is illustrious by molecular polarizability (α). The laser beam could be an oscillating electromagnetic wave with electrical vector E. After interacting with the specimen, it induces electric dipole moment $P = \alpha E$ resulting in the deformation of molecules. Due to periodic deformation, a vibration of molecules with characteristic frequency U_m starts. Energy levels and transitions are linked to the Raman result: Laser-made, monochromatic light of infrared, ultra-violet, or visible frequency can be used as an

excitation source. In predictable Raman Spectroscopy, visible lasers of Kr+, Ar+, He-Ne, Nd: YAG, or diode are used to stimulate the molecules to high-energy "virtual" excitation states. The Raman result occurs when light focusing on a molecule interacts with the electron cloud and the bonds of that molecule. The impulsive Raman Effect is a type of light scattering in which a photon excites the molecule from the ground state to a virtual energy state. When the molecule deexcites, it emits a photon and then returns to a varied vibrational or rotational state.

The energy difference between the original state and excited state leads to a frequency shift of emitted photons away from the excitation wavelength. That is, the fundamental principle is the incident monochromatic laser beam depolarization through oscillations of molecules. The incident light beams interact with the molecular bonds and their electron clouds. More than 90 % of the laser light is transmitted, which was initially directed towards the sample. A small light extent is elastically scattered, known as Rayleigh-Scattering.

As can be seen from Figure 3.7, the frequency or energy state of the molecules will not change. The process of inelastic scattering is referred to as Raman-scattering. All molecules execute definite oscillations in their initial state. Because of inelastically scattered photons, the molecules lose or gain some energy, altering the initial state to a virtually intermediate energy state. As soon as the molecule is relaxed, it is dropped down to a different exciting energy state due to which a photon is emitted.

If a molecule gains some energy by attaining a higher energy level than the initial energy level, a change in frequency occurs, and the frequency of scattered photons will be lesser than $\nu_0 - \nu_m$. This process is referred to as Stokes-Scattering. Nevertheless, Anti-Stokes-Scattering is caused by a higher frequency than $\nu_0 + \nu_m$ along with the higher energy of the scattered photons. This process is only probable if the molecule resides in a higher energy state before the photon collisions. The energy difference between the incident and the scattered photon is called the Raman frequency shift, representing each molecule. The photon energy after Rayleigh-Scattering is:

$$\mathbf{E = h\nu_0} \qquad \mathbf{(3.1)}$$

In the case of Rayleigh Scattering, the molecule is excited to any virtual state then the molecule is relaxed back to its original state. Lastly, the photon is scattered elastically, leaving with its original energy. In the case of Stokes Scattering, the molecule is excited to any virtual state. Afterward, the

molecule is relaxed back to a higher vibrational state than initially. The photon leaves with energy hν-ΔE and is scattered inelastically.

In Anti-Stokes Scattering, the molecule is excited in any virtual state. Afterward, it is relaxed back to a lower vibrational state with a loss of energy hν+ΔE and is scattered elastically (Figure 3.7)

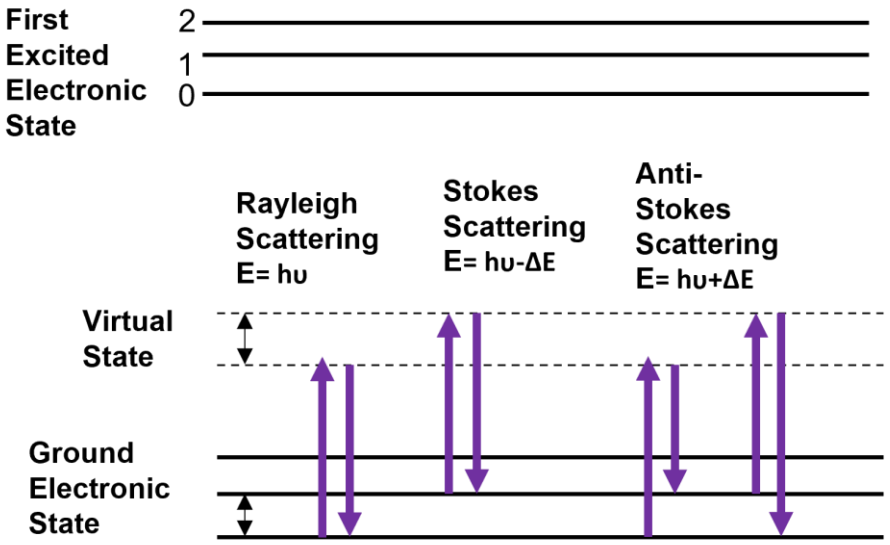

Figure 3.7: Three types of scattering by a molecule excited by a photon with energy E = hν. The most common transitions are marked with bold arrows.

3.7. Ultraviolet and visible spectroscopy

In ultraviolet and visible spectroscopy, the absorption of radiations in the ultraviolet and visible region of the electromagnetic spectrum is recorded. The ultraviolet region ranges from 10 nm to 400 nm and is subdivided into two regions: the near-ultraviolet region (200-400 nm) and the far-ultraviolet region (10-200 nm). The range of the visible region is from 400 to 800 nm. Ultraviolet and visible spectroscopy is used for detecting the presence and elucidating the nature of the multiple conjugated bonds or aromatic rings [148].

3.7.1. Origin of UV- visible spectra

The origin of UV-visible absorption spectra is electronic transition within a molecule. As a result of these transitions, electrons promote from the ground state to the higher energy states. These are

electronic transitions caused by the absorption of radiation energy in UV-visible regions of the electromagnetic spectrum [148]. The energy difference between the two states is

$$E = h\nu \quad \text{(3.2)}$$

Also

$$E = E_1 - E_2 \quad \text{(3.3)}$$

Where E_1 = energy of ground state

E_2 = energy of excited state

The total energy of the molecule is the sum of electronic, vibrational, and rotational energies.

$$E_{total} = E_{electonic} + E_{vib} + E_{rotational} \quad \text{(3.4)}$$

UV absorption involves only electronic transitions from low to high energy states, but its spectrum does not contain a single discrete line but a broad absorption band. The reason is that vibrational and rotational transitions also accompany electronic transitions, and the energy required for these transitions is much less, and a broad band appears.

3.7.2. Instrumentation & working of UV-visible spectrometer

The function of UV- visible spectrometer is to compare the intensity of the transmitted radiation with incident UV-visible radiation. Most UV-visible spectrometers are double-beam instruments and consist of components shown in Figure 3.8.

3.7.3. Radiation source

The most commonly used radiation source in the UV region is a hydrogen discharge lamp. A deuterium lamp is used in its place when five times high intensity is required. A second light source, a tungsten filament, is used when absorption in the visible range (400-800 nm) is to be determined.

3.7.4. Monochromator

Its function is to disperse the radiation from the source into their separate wavelengths. Usually, the dispersing element is a prism or grating. The dispersed radiation is divided into two parallel beams of equal intensity by a beam divider. One beam passes through a transparent cell containing the sample solution and is called sample beam. The second beam passes through an identical cell containing the solvent and is called reference beam.

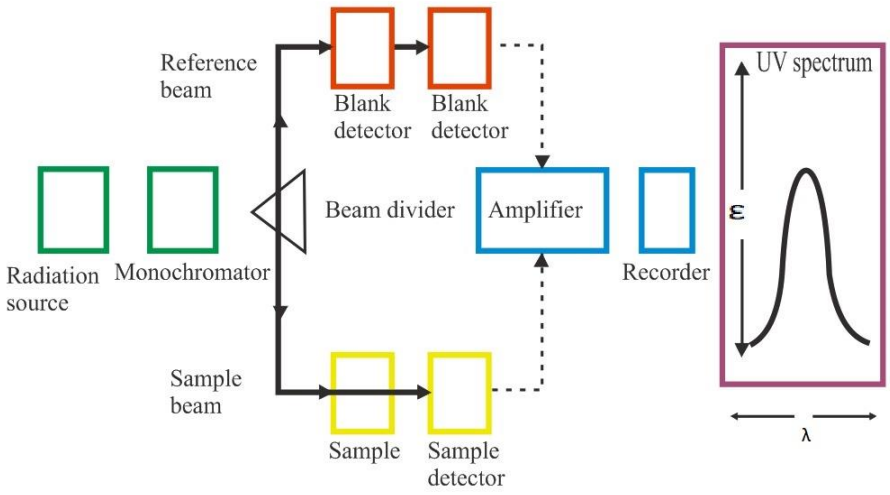

Figure 3.8: UV-visible spectrometer working

3.7.5. Detectors

Detectors have photocells or photomultiplier tubes that generate the voltage proportional to radiation energy striking them.

3.7.6. Amplifier & recorder

Balancing electronic amplifier subtracts the absorption of the solvent from that of the solution electronically. The recorder records the spectrum as a plot of the wavelength of absorbed radiations against absorbance or molar absorptivity [148].

3.7.7. Absorption laws and molar absorptivity

UV-visible spectrometer records the UV or visible spectrum as a plot of wavelengths of absorbed radiations versus the intensity of absorption in terms of absorbance (optical density), which is denoted by **A**, or molar absorptivity **ε**, as defined by Lambert-Beer law. Lambert's law is defined *as "The fraction of incident monochromatic radiation absorbed by a homogeneous medium is independent of the intensity of incident radiation."* Beer's law is defined as: "*The absorption of monochromatic radiation by a homogeneous medium is proportional to the number of absorbing molecules*."

From the above two laws, the remaining variables give Lambert-Beer law in the form of the equation:

$$\log_{10} Io_{o}/\mathrm{I} = A = \varepsilon cl \ldots\ldots\ldots\ldots\ldots\ldots\ldots\ldots\ldots \quad (3.5)$$

I_o is the intensity of incident radiation, I is the intensity of radiation transmitted through the sample solution, c is the concentration of the solute (mole per liter), and l is the path length of the sample (cm). The molar absorptivity of an organic compound is constant at the given wavelength. The intensity of an absorption band in the UV or visible spectrum is usually expressed as the molar absorptivity at maximum absorption (ε_{max}). The wavelength of maximum absorption is denoted by λ_{max} [148].

3.8. X-ray diffraction (XRD)

XRD is a versatile, non-destructive technique used to identify the crystalline materials, how many phases are present, and in how much quantity. Lattice constant and system can also be analyzed very quickly using the powder diffraction method.

X- rays were discovered by the German physicist Roentgen in 1985. These are electromagnetic radiations of very short wavelength as compared to light. The X-rays used in diffraction have wavelength ranging from 0.5-2.5 Å. In the complete electromagnetic spectrum, X-rays occupy the region between gamma and ultraviolet rays [149].

3.8.1. Principle of X-ray diffraction

The basic principle behind the X-ray diffraction process is constructive interference of X-rays. Constructive interference occurs when path difference between the scattered wave and incident wave is an integral multiple of the wavelength of the incident beam. As shown in Figure 3.9, when monochromatic and parallel X-ray beams with a wavelength and angle of incidence are diffracted by the set of planes oriented in a specific direction, sharp peaks corresponding to the inter planner spacing *d* are produced when the Bragg's condition is satisfied

$$2d\sin\theta = n\lambda \ldots\ldots\ldots\ldots\ldots\ldots\ldots\ldots\ldots\ldots\ldots \quad (3.6)$$

Where *n* is an integer gives the order of reflection.

3.8.2. Methods of X-ray diffraction

Diffraction can occur whenever the Bragg law is satisfied. Bragg law can be satisfied by varying either λ or θ during the experiment. The ways in which these quantities are varied distinguish the three diffraction methods:

1) Laue method

2) Rotating crystal method

3) Powder method [149]

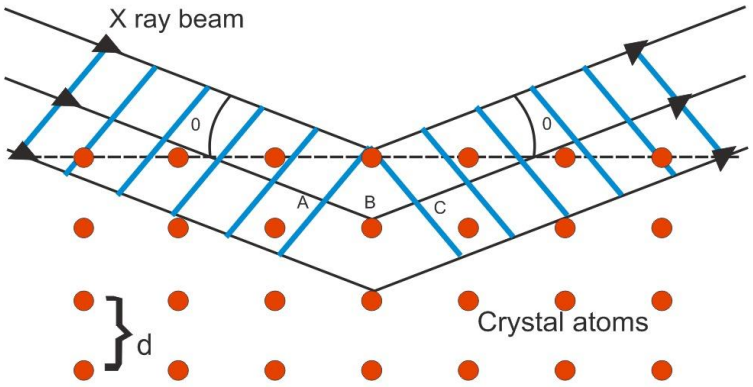

Figure 3.9: Bragg's law reflection

3.8.3. Basic components of X-ray diffractometer

The experimental geometry used in the powder diffraction method is illustrated in the Figure 3.10. The three basic components of an X-ray diffractometer are X-ray source, specimen, and detector. All three components lie on the circumference of a focusing circle. The angle between the plane of specimen and X-ray source is Bragg angle (θ). The angle between the projection of the source and the detector is 2θ. The X-ray diffraction patterns produced with this geometry are known as θ-2θ scans. In θ-2θ geometry, the X-ray source is fixed, and the detector moves through the range of angles. The radius of the focusing circle increases as the angle 2θ decreases. The diffractometer circle in Figure 3.10 is different from the focusing circle centered at the specimen, and both the X-

ray source and detector lie on the circumference of this circle. The radius of the diffractometer circle is fixed. The diffractometer circle is also called the goniometer circle. The goniometer is the central component of an X-ray diffractometer and contains the specimen holder. It has arms to which the X-ray source and detector are mounted [150].

3.8.3.1. The X-ray source

X–rays are produced by directing an electron beam of high voltage at a metal target anode inside an evacuated X-ray tube. An X-ray tube contains a source of electrons, a high accelerating voltage, and a metal target.

Suitable operating voltages depend on the target metal, and they should be above the critical excitation potential for knocking out *k* electrons. For molybdenum target, the operating voltage is 50 to 55 kV; for the copper target, it is 25 to 40 kV. Copper is the most frequently used target, and operating conditions are 40 kV and 30 mA [150].

3.8.3.2. The specimen

A thin layer of powder is spread onto a planer substrate, such as a glass microscope slide, and exposed to the X-ray beam in a typical X-ray diffraction experiment. In a powder or polycrystalline material, the grains are often randomly oriented. Some grains will always be oriented in a favorable direction to allow diffraction from a specific set of lattice planes. Each set of lattice planes in the crystal having spacings d_1, d_2, d_3 ,……will diffract at different angles θ_1 ,θ_2, ,θ_3 …….. in such a way to satisfy Bragg′s law. The intensity of the diffracted beam at each of these angles is detected, and the X-ray diffraction pattern is formed [150].

3.8.3.3. Filters

For X-ray diffraction purposes, a monochromatic radiation is required, but the beam from X-ray tube contains a strong K_α line and a weaker K_β line and the continuous spectrum. The intensity of these undesirable components can be decreased relative to the intensity of K_α line by passing the beam through a filter that absorbs the K_β component much more strongly than K_α component due to an abrupt change in its absorption coefficient between these two wavelengths.

3.8.3.4. Counter

In the diffractometer, the intensity of a diffracted beam is directly measured by an electronic counter. Counters convert incoming X- rays into surges or pulses of electronic current in the circuit

connected to the counter. This circuit counts the number of current pulses per unit time, and this number is directly proportional to the intensity of X-ray beam entering the counter [149].

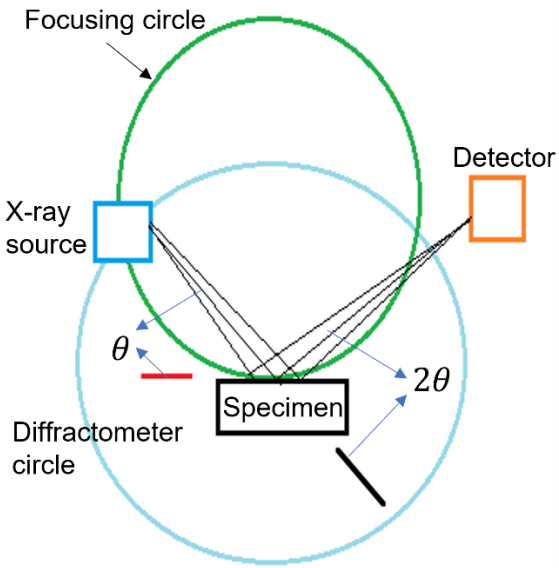

Figure 3.10: Components of X-ray diffractometer

A filter in the diffracted beam not only suppresses the K_β radiation but also reduces the background radiation originating in the specimen [149].

3.9. Transmission electron microscopy (TEM)

Transmission Electron Microscopy (TEM) is the most prevalent technique of characterization of nanomaterials in electron microscopy. The images and chemical information of nanomaterials at a spatial resolution equivalent to the atomic dimensions levels.

Upon the interaction of the electron beam with the sample, the beam is converted into elastically or inelastically scattered electrons. The distance ratio among the sample, the objective lens, and the image plane is considered to be magnified by the lens. Both TEM and SEM illustrate the size in micrometer or nanometer range, degree of dispersion and aggregation, and the material's heterogeneity. In comparison with SEM, TEM offers more advantages by providing good quality spatial resolution and analytical measurements. The TEM could measure the precise particle size

of either bright or dark field images and also it provides details about the nanoparticles because it uses energetic electrons to provide information regarding compositional, morphological, and crystallographic features.

Diffraction, spectroscopy along with imaging are the three major techniques that can be observed in TEM. The classification and working principle of TEM are described in Figure 3.11 and Figure 3.12 respectively. TEM works under the principle of optical microscopy. The difference is that electrons replace photons, glass lenses are replaced with electromagnetic lenses, and images can be observed on a screen as a replacement for an eyepiece. One of the most important advantages of TEM is its powerful magnification and the provision of information about element and compound structures. Black-and-white images can be observed as output [151].

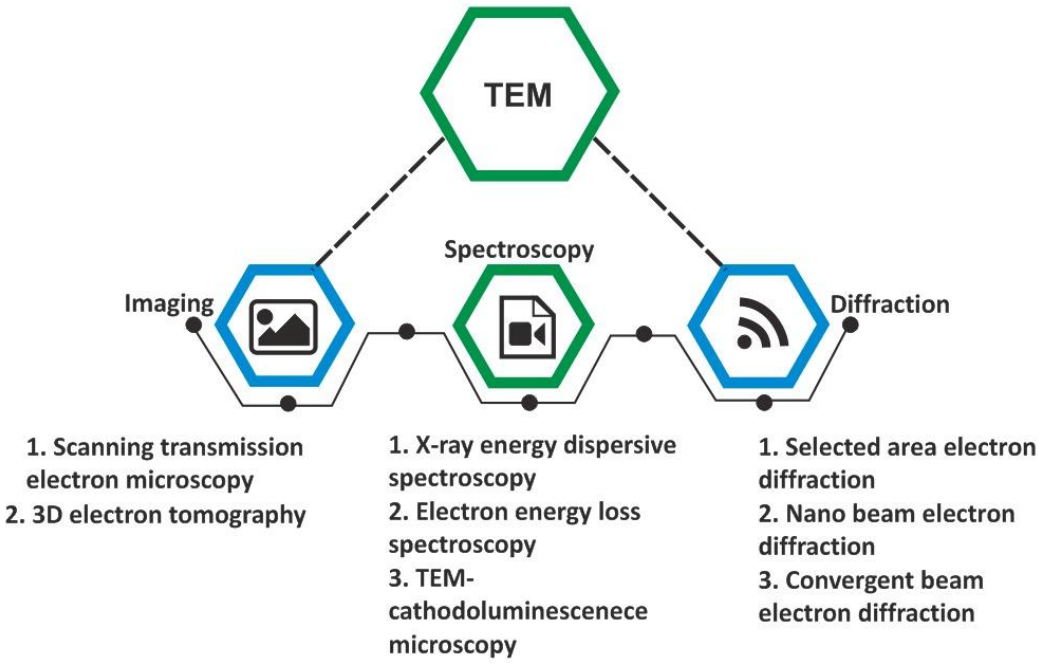

Figure 3.11: Classification of transmission electron microscopy

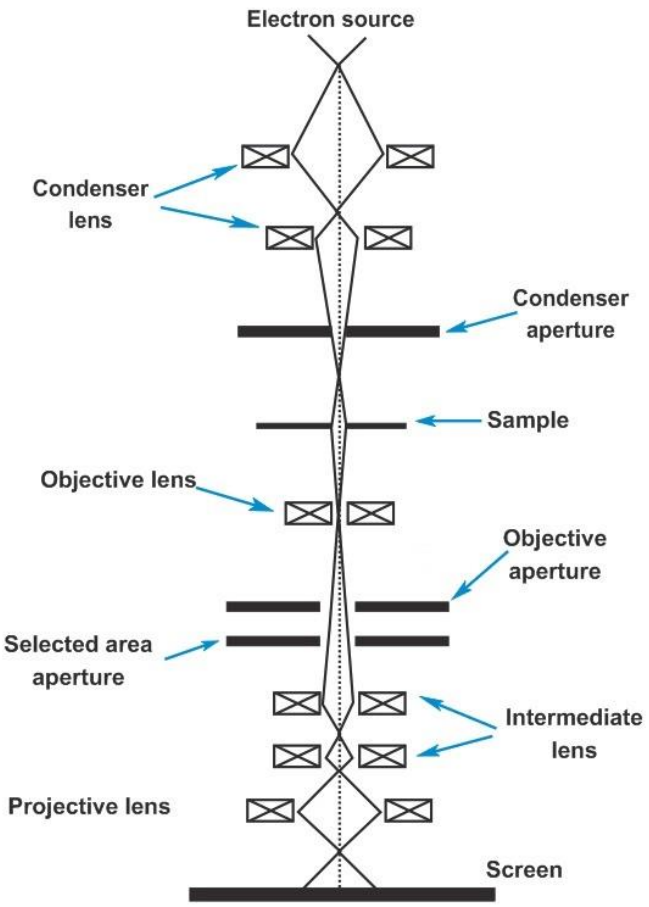

Figure 3.12: Working principle of transmission electron microscope

3.10. Energy dispersive X-ray analysis (EDX)

The energy dispersive X-ray spectroscopy is a technique used for elemental analysis and determination of the chemical composition of materials. EDX system is normally attached to an electron microscopy instrument such as scanning electron microscopy (SEM) or transmission electron microscopy (TEM). EDX is formulated on the emission of a specimen characteristic X-rays. The technique depends on the characteristic X-rays generation that discloses the identity of the elements present in the specimen [152]. A high-energy beam of charged particles (protons or electrons) is focused on the investigated sample. An electron falls from a higher binding energy electron level into the core hole, and X-rays having the energy difference of the binding energies of electron level are emitted. The results of EDX analysis provide a spectrum that presents the peaks associated with the elemental composition of the investigated sample. Moreover, elemental

mapping of the sample of interest can be generated with EDX method. EDX spectroscopic method is described in Figure 3.13. EDX analysis offers both semi-qualitative and semi-quantitative information [153]. In Figure 3.14, an example of the EDX spectrum of zinc peroxide nanoparticles are shown. The Cu and carbon signal peaks correspond to the sample holder.

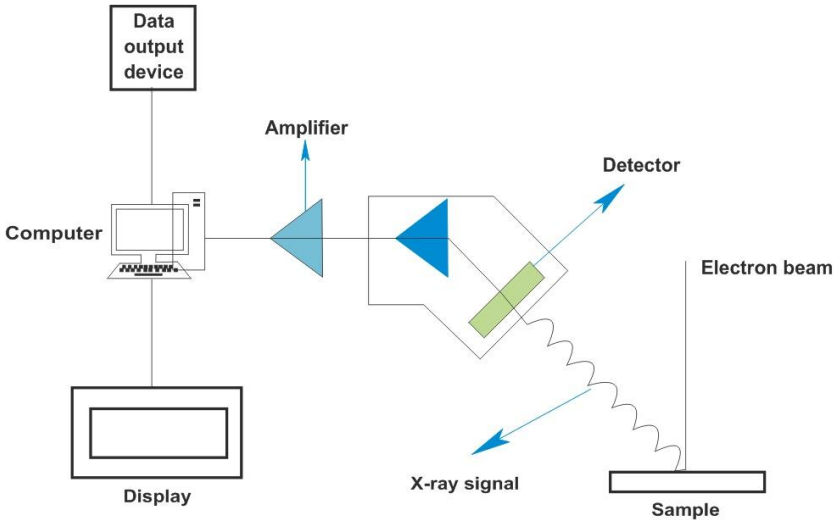

Figure 3.13: Energy dispersive X-ray spectroscopy schematic and working

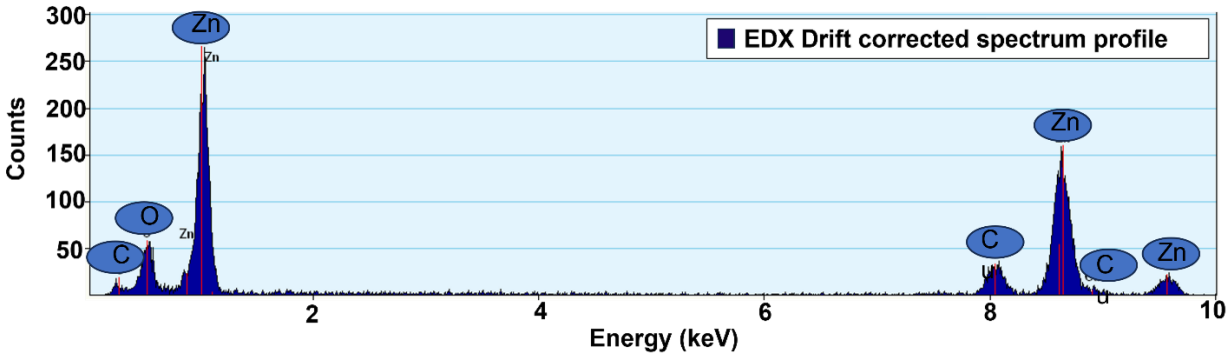

Figure 3.14: EDX spectrum obtained for synthesized zinc per oxide nanoparticles.

3.11. Techniques used in cell culture

3.11.1. Optical microscope

The optical microscope is a valuable instrument for observing cell culture and confirming that the cell culture process is proceeding properly.
An operator can visually observe the cultured cells using an optical microscope to evaluate their condition and determine whether to continue towards the next step in the culture process. The cultured cells applications are anticipated to continue developing in drug discovery, safety evaluation, and regenerative medicine.

Configuration and operation

A light microscope, also known as optical microscope, uses a system of one or a series of lenses for magnifying images of small samples with visible light. The lenses are placed between the sample and the viewer's eye to magnify the image to make a detailed examination of the samples. The objective lens is brought closer to the investigated sample to allow the light inside the microscope tube. This generates an enlarged and inverted image of the sample, which can be viewed through the eyepiece of the microscope (Figure 3.15).

Types of optical microscopes

There are various categories of light microscopes. They can differ from a very basic design to a highly complex design that provides high resolution and contrast. Some popular types of optical microscopes include the following:

- A simple microscope uses a single lens to magnify the sample image. This is analogous to a magnifying glass.
- A compound microscope utilizes a series of lenses for magnifying the sample to get a higher resolution image.
- A digital microscope can have simple or compound lenses, and a computer is utilized to visualize the image. There is no need for an eyepiece to observe the sample.
- Stereo microscope offers a stereoscopic image, which is beneficial for dissections.
- Inverted microscope: The sample can be viewed underneath through the inverted microscope, which is beneficial for examining liquid cell cultures.

Other optical microscopes include polarizing, petrographic, epifluorescence, phase contrast, and confocal microscopes.

Applications

Light microscopy offers several applications in different areas, including metallurgy, gemmology, and chemistry. It is one of the minimum invasive techniques for observing living cells for biological applications. The light microscope could be used to get the information about the cell's activity and to have a look at tiny structures.

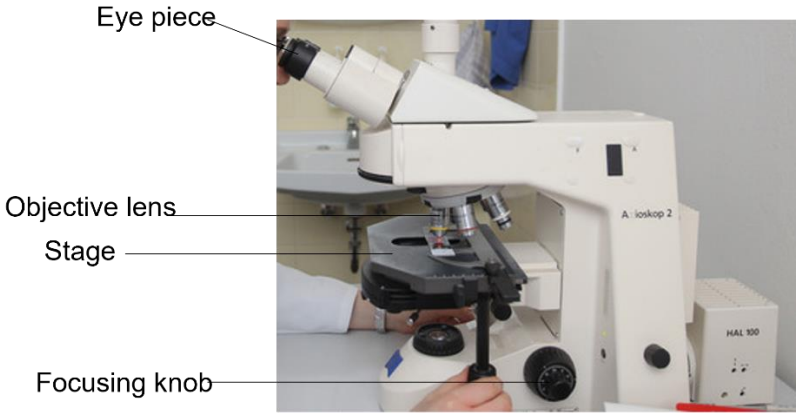

Figure 3.15:Components of Light Microscope taken at Oncology lab UKSH, Kiel

3.11.2. Microplate reader

A microplate reader is used to measure biological, chemical or physical reactions and properties of analyte inside the well of a microplate. A microplate comprises small wells in which separated reactions can occur. The analyte or the progression of biochemical processes convert into optical signals through these reactions. The microplate reader identifies these signals and consequently quantifies the parameter of interest.

Applications of microplate reader

A microplate reader is utilized for the quantification of numerous chemical or biological assays in a microplate. Currently, the obtainability of a plethora of reagent kits allows the utilization of a microplate reader in different fields and for various applications. In addition to biological and

pharmaceutical research, both in academics and industry, plate readers are currently being used in the food or cosmetics industry and environmental research.

Working principle of a microplate reader

Light signals produced by samples that have been pipetted into a microplate are detected by a microplate reader. The biological, chemical or physical reactions inside the sample result in optical properties of samples. Different optical changes are the result of different analytic reactions used for analysis. Absorbance, fluorescence intensity, and luminescence are the most common and most frequently used detection modes. In addition, advanced modes such as time-resolved fluorescence, fluorescence polarization, and AlphaScreen® are also offered by modern instruments.

Microplate measurements detect the light signals produced, converted, or transmitted through the sample. The signals are measured by a detector (Figure 3.16), generally a photomultiplier tube (PMT). This PMT converts photons into electricity which the microplate reader later quantifies. The output of the entire process is a number by which a sample is quantified.

Samples might need to be excited by the light at a specific wavelength subjected to the nature of the optical signal changes during a reaction. The light is generally provided by a light source (Halogen or Xenon flash lamp). The light generated by the lamp is carefully chosen by a specific excitation filter or monochromator (Figure 3.16). Filters are equally employed on the emission/detection side and are usually positioned between the detector and the sample to increase sensitivity.

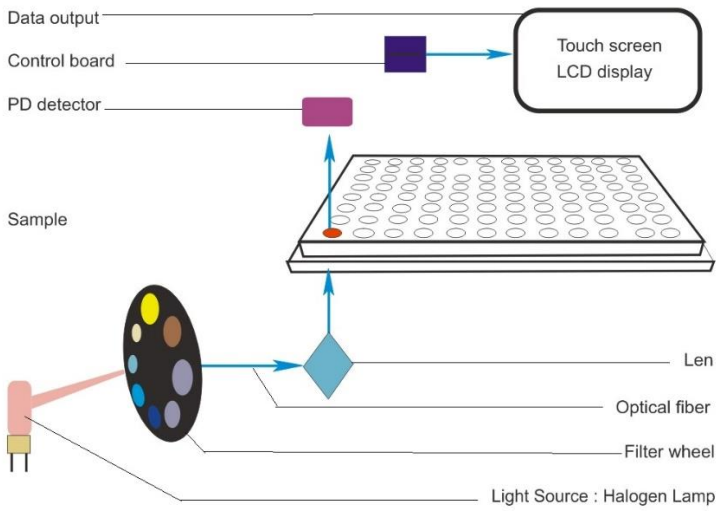

Figure 3.16: Schematic of working of microplate reader for cytotoxicity assays

3.11.3. Flow cytometery

The **ImageStream®^{X} Mark II Imaging Flow Cytometer** combines the sensitivity, speed, and phenotyping capacities of flow cytometry with microscopy's comprehensive functional and imagery insights. This instrument generates multiple high-resolution images of every cell directly in flow, containing brightfield and darkfield (SSC) and about ten fluorescent markers. It has sensitivity more than conventional flow cytometers.

System overview

The ImageStreamX MkII obtains up to twelve images instantaneously of every cell or object comprising scatter, brightfield, and multiple fluorescent images at rates of maximum 1,000 objects per second. The ImageStreamX MkII CCD camera uses time-delay-integration (TDI) detection technology. It allows up to 1,000 times additional signal from cells in flow compared to conventional frame imaging methodologies. Detection of velocity and autofocus systems sustain appropriate camera synchronization and focus during image attainment. The following Figure 3.17 demonstrates the working of ImageStreamX MkII.

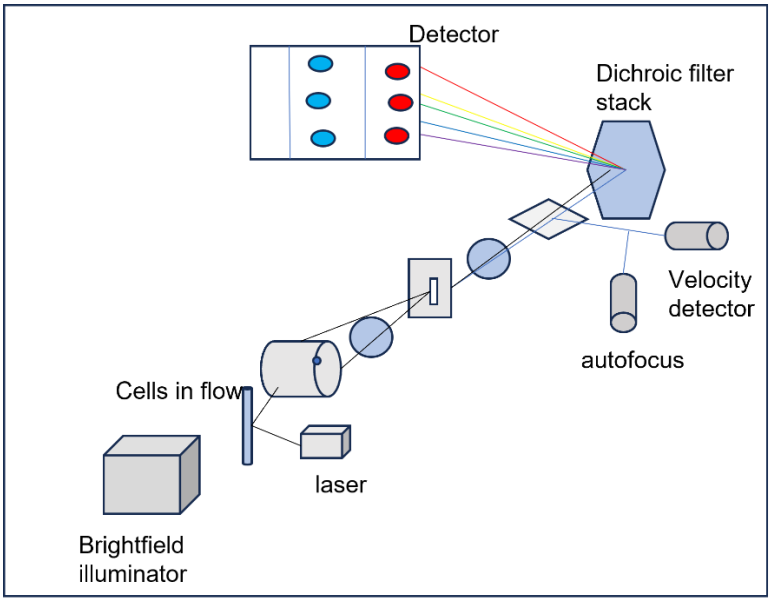

Figure 3.17: Trans-illumination of hydrodynamically focused cells done orthogonally by a laser(s) and a brightfield light source.

In Figure 3.17, an objective lens of a high numerical aperture (NA) collects fluorescence emissions, transmitted and scattered light from the cells. The collected light interconnects with the spectral decomposition element in the optical space. Light related to different band spectra leaves the decomposition element at different angles such that each band is focused onto six different physical locations of one of the two Charged Coupled Device (CCD) cameras with 256 rows of pixels. Consequently, the image of each cell is disintegrated into six discrete sub-images on each CCD chip based upon different spectral wavelengths. The two-camera system collects up to 12 images per object.

The CCD camera works in time delay integration (TDI) mode that electronically tracks the moving objects by moving the content of pixel from row to row down the 256 rows of pixels synchronized with the object (cell) flow velocity as measured by the velocity detection system. Pixel content is collected off the last row of pixels. Imaging in this mode allows for the collection of cell images without streaking and high fluorescence sensitivity.

Chapter 4: Materials and methods

This section provides a detailed explanation of materials synthesis and experimental cell culture methods employed within the given work. Further, the detailed information about the sample preparation and instrument's conditions for the following techniques: Scanning Electron Microscopy, RAMAN Spectroscopy, X-ray diffraction analysis, UV-visible spectroscopy, and Transmission Electron Microscopy is described.

4.1. Synthesis and Characterization of ZnO tetrapods and ZnO_2 NPs

The freestanding tetrapod-shaped ZnO structures (T-ZnO) with varying sizes were synthesized using the simple flame transport synthesis (FTS) technique [126]. Zinc peroxide spherical NPs (ZnO_2 NPs type 1 and type 2) were synthesized by Leidenfrost nanochemistry, as reported elsewhere [121]. Commercial ZnO nanoparticles (average size: 50 nm) were purchased from Sigma Aldrich (CAS No 8278-2).

Pre-treatments of T-ZnO

Cytotoxic behavior of ZnO might be influenced by the oxygen vacancies present in their structure. Papavlassopoulos et al. [154] have changed the content of oxygen vacancies in T-ZnO. A reduction of oxygen vacancies can be obtained by heating the tetrapods in an oxygen-rich environment, or the increase in vacancies can be attained with UV illumination of T-ZnO [154]. As soon as the oxygen vacancy content changes, it also affects the hydrophilicity of T-ZnO and their wetting behavior. Untreated normal conditions, T-ZnO is only slightly hydrophobic; however, it becomes more hydrophobic if heated in an oxygen-rich environment. Inversely, when the tetrapods are irradiated by UV light, they become super hydrophilic. The hydrophilic and hydrophobic behaviors of T-ZnO under different treatments were also proven by water droplet tests using contact angle measurements in a previous report [154]. For the current study, only O_2-treatment was performed by adding 3 g of T-ZnO powder in 10 % H_2O_2 solution and heated at 100 °C for 15 min. Tetrapods were observed to change their wetting behavior. More hydrophobicity was confirmed by the displacement of tetrapods from the bottom of H_2O_2 solution containing beaker to the top of the beaker. The oxygen-treated tetrapods were collected by filtration and dried at 80 °C for further use in cell culture experiments.

Crushed ZnO rods

To examine the effects of particle geometry and surface on cytotoxicity, crushing of ZnO tetrapods was executed with a hand mortar and pestle for 2 minutes. This has led to the formation of ZnO rods with improved surface area. In the crushing process, the arms of tetrapods get broken, and the resulting crushed powder approximately exhibited 1D ZnO- rod structure. Each broken rod further raises surface area equivalent to the two hexagonal area cross-sections at the broken end [154]. A small amount of as-prepared intact T-ZnO powder was dispersed in distilled water for crushing for the current experiments. Crushing was performed for 3 minutes by using an ultrasonic stick in this dispersion, resulting in finer ZnO rods.

Scanning electron microscopy (SEM)

For SEM (ZEISS ULTRA plus, 7 kV) characterization, both types of ZnO_2 NPs were dispersed in ethanol. Then 100 µl of particle suspensions were transferred to a small piece of a silicon wafer using a micropipette. For the SEM characterization of ZnO tetrapods, a small amount of powder was placed on a sticky carbon tape for investigation.

RAMAN spectroscopy

Micro-Raman spectra of T-ZnO (intact, crushed, and O_2-treated), ZnO_2 NPs (type 1 and type 2), and ZnO nanopowder (from sigma Aldrich) were measured with a Raman WITec Alpha 300 RA spectrometer. A 532 nm line from Nd-YAG laser was used for excitation.

X-ray diffraction

X-ray diffraction (XRD) spectra were taken by using a 3000 TT Seifert X-ray diffractometer unit. All measurements were taken with Cu Kα radiation with $\lambda = 0.154$ nm operating at 40 kV and 40 mA at ambient temperature. The measurements were performed over an angular range of 25–80°. A thin layer of all samples was deposited on a glass substrate for the measurements.

Transmission electron microscopy (TEM)

The ZnO_2 NPs of two different types were dispersed in butanol by stirring in a mortar. The dispersion was drop-casted onto Cu lacey TEM grids (Plano GmbH). An FEI Tecnai F30 STwin G^2 with 300 kV acceleration voltage was used for bright-field and dark-field TEM investigations. The dark-field images were acquired in scanning transmission electron microscopy (STEM) mode with a high-angle annular dark-field (HAADF) detector, which enables atomic number dependent *Z*-contrast as well as mass-thickness contrast. For energy dispersive X-ray (EDX) spectroscopy,

the microscope is equipped with a Si/Li detector (EDAX System). Particle size was measured from TEM bright-field micrographs using a custom-made script in Digital micrograph (Version 3.43, Gatan, Inc.).

4.2. Determination of cytotoxicity of ZnO_2 NPs and T-ZnO

Two different types of ZnO_2 NPs (average size 50-300 nm and 20-80 nm) were selected for the toxicity tests. In addition, the toxicity of tetrapodal ZnO microstructures (T-ZnO) with and without surface charge (O_2-treatment or etching) and structural changes (crushing) was also determined for comparison. Commercial ZnO nanopowder (average particle size = 50 nm) was used as a reference in all experiments. Experiments were performed with the same concentration range (0.001-10 mg/ml) of each particle type.

4.2.1. Cell culture protocol of MCF-7 cells

In vitro cytotoxicity assays were performed on breast cancer MCF-7 cell line. Cells were cultured in RPMI 1640 medium supplemented with 10 % Fetal Bovine Serum (FBS) and Penicillin/Streptomycin solution (100 units/ml penicillin, 100 µg/ml streptomycin). Cells were grown at 37 ℃ under a humidified atmosphere with 5% CO_2. In all experiments, cells were used from passage numbers P15–P25. As soon as cells reached the required confluency, they were seeded on flat-bottomed 96-well plates at a density of 17000 cells/well for 24 h. Then cells were treated with varying concentrations (0.001-10 mg/ml) of ZnO_2 NPs, commercial ZnO nanopowder, and T-ZnO (untreated, crushed, and O_2-treated). Before culturing with the cells, NPs and tetrapods were washed three times with sterilized water and sedimented by centrifugation at 13000 rpm. The sedimented particles were dried at 40 ℃ overnight, weighted, and then re-dispersed in culture medium through ultrasonication to make a stock solution of 10 mg/ml. All dispersions were ultrasonicated for 30 min to achieve homogeneity before a serial dilution over the desired range. Dilutions were added into seeded cell culture, and plates were incubated for 48 h and then centrifuged at 30 g for 5 min. The cells' Confluency was measured every 24 h using a NYONE® microscopic device. Cell culture supernatants were collected and replaced with 12.5 µl of fresh RPMI to perform ApoLive-GloMultiplex viability assay.

4.2.2. Assay Protocol

- 17.5 µl of viability reagent was added to all wells and briefly mixed by orbital shaking (300–500 rpm for ~30 seconds).

- Well plates were incubated for 30 minutes and 60 min at 37 °C.
- Fluorescence was measured at the following wavelength set: $400_{Ex}/505_{Em}$

The number of viable cells were measured using a TECAN microplate reader (Infinite® 200 PRO) using an excitation wavelength of 400 nm and emission wavelength of 505 nm.

4.2.3. Cell culture protocol of fibroblasts RMF-EG

In vitro cytotoxicity assay was also performed on fibroblasts (RMF-EG) using the protocol as mentioned above for MCF-7 cells with slight modifications. Cells were cultured in DMEM medium supplemented with 10 % fetal bovine serum (FBS) and Penicillin/Streptomycin solution. Cells were seeded on flat-bottomed 96-well plates at a density of 10000 cells/well for 24 h. In all experiments, cells were used from passage numbers P15–P25. The concentration range of particles was the same (0.001-10 mg/ml) as in the case of MCF-7 cells for the treatment of nanoparticles and tetrapods.

4.3. Zinc ion release from ZnO and ZnO_2 micro and nanostructures

4.3.1. Zn^{+2} ions release in different pH media

The release of Zn^{2+} ions from ZnO_2 NPs and T-ZnO was measured. Materials (1 mg/ml concentrations) were incubated at 37 °C at different pH values. Phosphate buffer saline (PBS) of pH = 7.4 and 7.2 and acetate buffer of pH = 5.5 were employed as release media to imitate normal blood/tissues and endosomal/ lysosomal compartments of tumor cells, respectively. After 24 h of incubation, the samples were centrifuged to remove the NPs. Finally, the supernatant was withdrawn to determine the concentration of released Zn^{2+} ions using a UV-visible spectroscopic method for the determination of zinc [155].

4.3.2. Sample preparation and measurement for zinc ion release

For producing a calibration curve, samples (1 ml total volume) were prepared by adding 25 µl of a series of stock solutions (10 µg/ml-600 µg/ml) of ZnO to 950µl of borax buffer (pH 9.0). Reagent blanks were prepared analogously by replacing the zinc stock solution with water. For determination of Zn^{2+} ions in the supernatants, 25 µl of each supernatant to 950 µl of borax buffer (pH 9.0). With the addition of 25 µL of the zincon stock solution (40 µM), complexation with the zinc ions was initiated. Absorption was recorded at 620 nm after incubating the samples for 5 min

to confirm the Zincon-Zn^{2+} complex formation (blue color in solution) on a BioChrom Ultrospec 2100 spectrophotometer (Cambridge, UK) using a cuvette with a 1-cm path length.

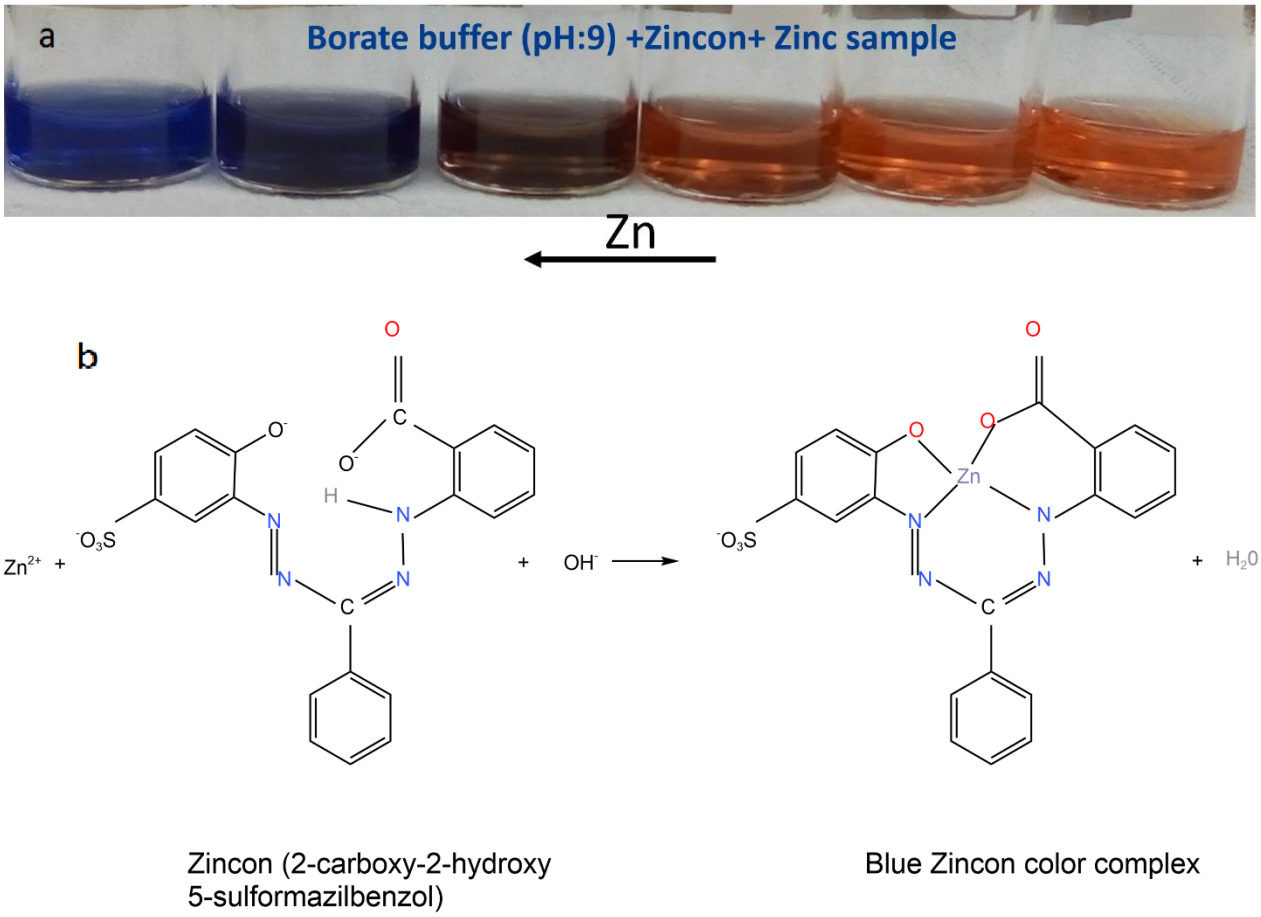

Figure 4.1: (a) Color changes in zinc stock solution after adding Zincon solution (b) Structures of Zincon in its free and zinc-bound form.

Zincon (40 µM) was exposed to Zn^{2+} five minutes before recording the absorbance at 620 nm. Values were obtained after subtraction of the blank (i.e., $[Zn^{2+}] = 0$) absorbance. All spectra were recorded in borax buffer (pH 9.0) at room temperature using Zincon at a final concentration of 40 µM.

4.4. Protocol for intracellular zinc ion measurement

MCF-7 cells (500,000 cells/well) were seeded in a six-well plate and were exposed to 1 mg/ml concentration of ZnO_2 nanoparticles for 2 h and 4 h. After each incubation time medium was

removed, and the cells were washed twice with Phosphate buffer saline (1× PBS) and labeled with 25 µM zinquin solution. Cells were incubated with zinquin solution for 30 min in the dark in a humidified incubator at 37 °C and 5 % CO_2 to allow cellular uptake. After 30 min, zinquin solution was removed, and cells were again washed with PBS to remove extracellular zinquin. Cells were harvested, trypsinized, and transferred to 1.5 ml Eppendorf tubes. Then all tubes were quick spinned, the medium was removed, and cell pellets were washed with PBS. For quantification of dead cells, Far-Red Dead Cell Stain (FRD) was diluted in PBS with a ratio of 1:5000. Cells were resuspended in this FRD solution and incubated at 4 °C for 20 min. Following centrifugation (5min, 20 °C, 30 g), stained cell pellets were washed again with PBS and resuspended in 50 µL PBS. 50 µL of 1 % Paraformaldehyde (PFA) was used for fixation for cells that were not stained with FRD. Then, samples were quantified by the flow cytometer (Image Stream®^{X} Mark II Imaging Flow Cytometer, Merck, Germany). Cells were titled as "zinquin positive" (with high zinc ion levels) when zinquin expression was more than the 90th percentile of the normal distribution of zinquin in the untreated control cells (zinquin negative having small zinc ion levels). Each treatment was executed in triplicate for each of three experiments.

4.5. Release of DOX from ZnO_2 NPs

The Doxorubicin (DOX) release experiments were performed by using a protocol similar to as described in literature [156]. A drug release system was prepared by suspending 10 mg of DOX-loaded ZnO_2 nanoparticles (**10-80 nm)** in 1 ml of buffer solutions (PBS pH 7.4 and acetate buffer pH 5.5) at 37 °C. All experiments were carried out in an orbital shaker with a frequency of 200 rpm. 0.5 ml of release medium was collected by centrifuge (13000 rpm, 10 min) at different time points (1 h, 6 h, 24 h, 48 h, 72 h). A TECAN cell counter device (Infinite® 200 PRO) was used to measure the absorbance at 480 nm at each time point. An equal volume of fresh buffer was added after each sampling and release experiment was continued. The cumulative release percentages of DOX were calculated according to the formula:

$$\text{Cumulative drug release (\%)} = \left(\frac{Drug\ release\ at\ time\ t}{\text{Initial drug loaded}}\right) * 100 \text{.....(4.1)}$$

4.6. Cell culture protocol of MCF-7 cells for bare and drug loaded ZnO_2 NPs

MCF-7 cells were cultured in RPMI 1640 medium supplemented with 10 % Fetal Bovine Serum (FBS) and Penicillin/Streptomycin solution (100 units/ml penicillin, 100 µg/ml streptomycin).

Cells were grown at 37 °C under a humidified atmosphere with 5 % CO_2. In all experiments, cells were used from passage numbers P15–P25. As soon as cells reached the required confluency, they were seeded on flat-bottomed 96-well plates at a density of 17000 cells/well for 24 h. Then cells were treated with varying concentrations (1 µg/ml- 10 mg/ml) of ZnO_2 NPs (20-80 nm-sized), and drug-loaded ZnO_2 NPs (20-80 nm-sized). Before culturing with the cells, NPs were washed three times with sterilized water and sedimented by centrifugation at 13000 rpm. The sedimented particles were dried overnight at 40 °C, weighted, and then re-dispersed in culture medium through ultrasonication to make a stock solution of 10 mg/ml. All dispersions were ultrasonicated for 30 min to achieve homogeneity before a serial dilution over the desired range. Dilutions were added into seeded cell culture, and plates were incubated for 48 h and then centrifuged at 30 g for 5 min. The Confluency of cells was measured after every 24 h using a NYONE® microscopic device. After centrifugation, cell culture supernatants were collected and replaced with 12.5 µL of fresh RPMI to perform ApoLive-GloMultiplex viability assay. The number of viable cells were measured using a TECAN microplate reader (Infinite® 200 PRO) as described in section 4.2.2.

Chapter 5: Results and discussion

This chapter discusses the most important results obtained from the experiments that are performed for the cytotoxicity of tetrapods and nanoparticle and their cellular uptake. The following subsections discuss different properties, including morphological and structural characterization corresponding to each particle type. The chemical structure and crystalline nature of the particles were confirmed by Raman spectroscopy and XRD techniques, respectively. Successful cell culture for cytotoxicity of all particles type and cellular uptake of zinc peroxide nanoparticles has been shown in this chapter. The zinc ions released from T-ZnO and ZnO_2 nanoparticles is also discussed.

5.1. Scanning electron microscopy

Figure 5.1 showed the SEM images of the different ZnO-based materials investigated in this study, namely ZnO_2 NPs (type 1 and type 2), ZnO tetrapods, and commercial ZnO powder. In the case of Figure 5.1 (a-b) (type 1 NPs), it can be seen that particles were not agglomerated, and complete separation has occurred. The NPs had a spherical shape. NPs in Figure 5.1 (c, d) (type 2 NPs) also substantiated the approximately spherical shape; however, the particle separation was not good enough as compared to type 1 NPs. At some points, particles were slightly agglomerated. Moreover, SEM images at higher magnification (Figure 5.1d) showed that the particles were held together, which might be due to weak physical forces. However, particles with size in the nano range were formed in the case of both types of ZnO_2. The morphology of ZnO tetrapods (T-ZnO) was also examined by Scanning Electron Microscopy. Figure 5.1(e) displayed the representative SEM images of typical ZnO tetrapods (T-ZnO) without any crushing or etching process. The ZnO tetrapods exhibit a 3D spatial shape with four hexagonal cylindrical arms narrowing towards their tips. These four arms are interconnected with a mutual dihedral angle via a central joint. The arms of T-ZnO typically have a diameter of 1-2 µm and 0.1-0.8 µm at their base (joint) and tip, respectively. The arm length is in the range of 15–30 µm (measured by using Image. J software). As the 3D structures of tetrapods were mostly destroyed during crushing, the broken arms can be seen in Figure 5.1(f) after the crushing process. Figure 5.1 (g) showed the SEM of commercial ZnO in the form of small agglomerates and separate nano-sized spherical particles.

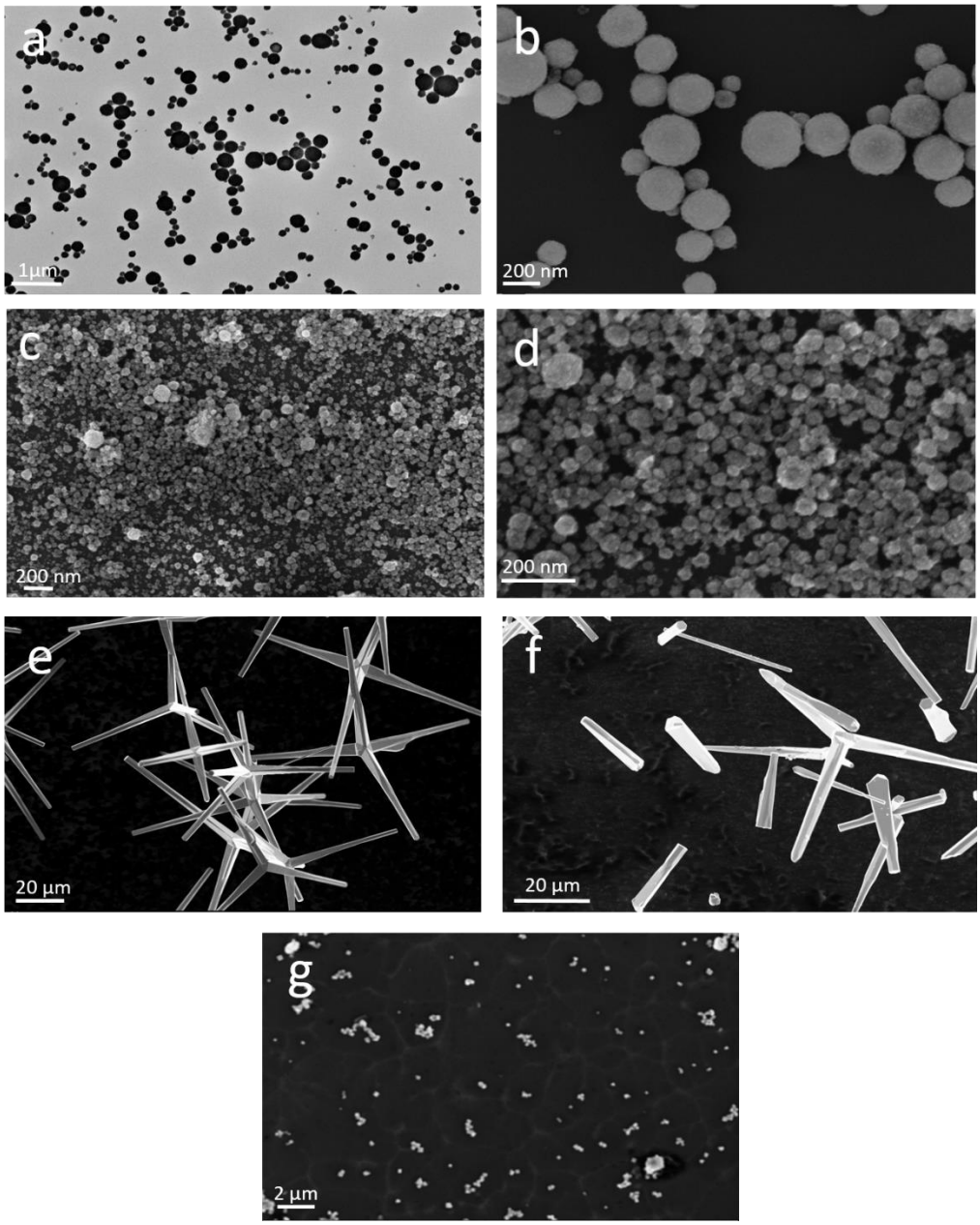

Figure 5.1:The Scanning Electron Microscope (SEM) images of the zinc peroxide nanoparticles (a-d) under higher magnification. For figures a-d, particles were formed with size in the nano range, and, the particle separation is good in type 1 nanoparticles (a, b). (e) SEM image of 3D tetrapodal zinc oxide (T-ZnO) powder. (f) SEM image of crushed tetrapodal zinc oxide (T-ZnO) at low magnification. Figure (g) shows the scanning electron micrograph of ZnO nanoparticles from Sigma Aldrich.

5.2. RAMAN spectroscopy

Figure 5.2 showed the room temperature micro-Raman spectra of untreated T-ZnO, crushed T-ZnO, O_2-treated T-ZnO, sigma ZnO NPs and ZnO_2 NPs in the range of 30–2000 cm^{-1}. All three tetrapodal ZnO (untreated, crushed, and O_2-treated) appeared with clearly defined peaks at ≈ 49.5 cm^{-1} and 389 cm^{-1}, characteristic of the wurtzite-type phase and can be attributed to E_2(low) and E_2(high) phonon modes [157,158]. The E_2(low) vibration mode is ascribed to vibrations of the zinc sublattice in ZnO, while E_2(high) is ascribed to vibrations of the oxygen. The small peaks at 286 and 335 cm^{-1} can be assigned to $2E_2$(low), E_2(high)-E_2(low), A_1(TO), and E_1(TO) phonon modes [159,160]. In the high-wavenumber region, a broad asymmetric peak appeared at ≈ 1,105 cm^{-1} in all three T-ZnO contained the contributions from second-order $2A_1$(LO) and $2E_1$(LO) phonon modes [157]. Figure 5.2 (green spectrum) shows the Raman spectra of commercial ZnO NPs. The basic phonon modes of commercial (sigma) ZnO have been obtained at 58.8, 286, 389 $cm^{-1,}$ and a doublet at 1,043 and 1,097 cm^{-1}. The Raman spectrum of ZnO_2 NPs (Figure 5.2, purple spectrum) showed that five signals were present at the positions of 95, 415, 839, 944 and 1,089 cm^{-1}. It can be observed from figure that some peaks display low intensity and have been found in other peroxides [161] and the peaks at 839 and 944 cm^{-1} are in agreement with the Raman spectra of nanocrystalline ZnO_2 [162]. A stretch mode of a O–O vibration is centered at 792 cm^{-1} [112].

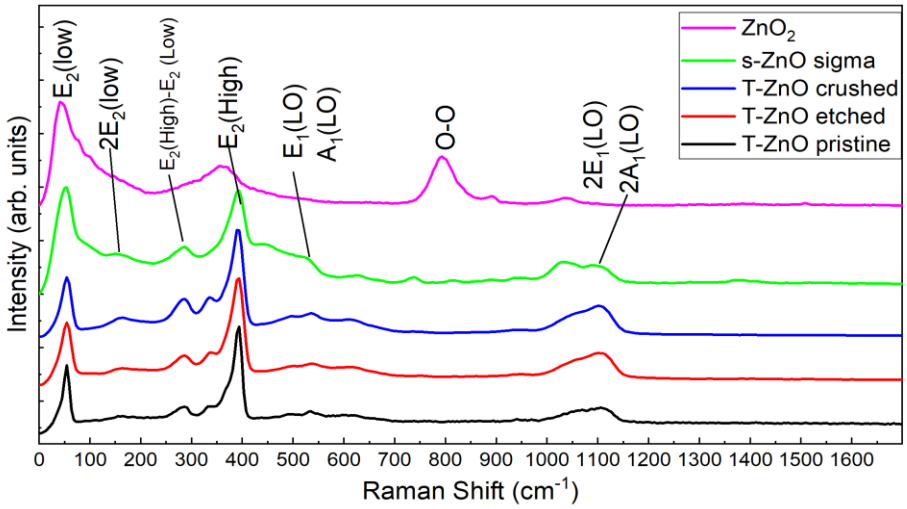

Figure 5.2: RAMAN spectra of ZnO tetrapods, commercial ZnO and ZnO_2 NPs

5.3. X-ray diffraction analysis of micro and nano ZnO and ZnO_2

Figure 5.3 showed the XRD patterns of untreated, crushed, and O_2-treated (etched) T-ZnO, Sigma ZnO, and ZnO_2 nanoparticles. Black, red and blue colors in Figure 5.3 depicted the crystal structure of ZnO tetrapods (untreated, crushed, and etched). The sharp peaks indicated that T-ZnO in all forms is highly crystalline.

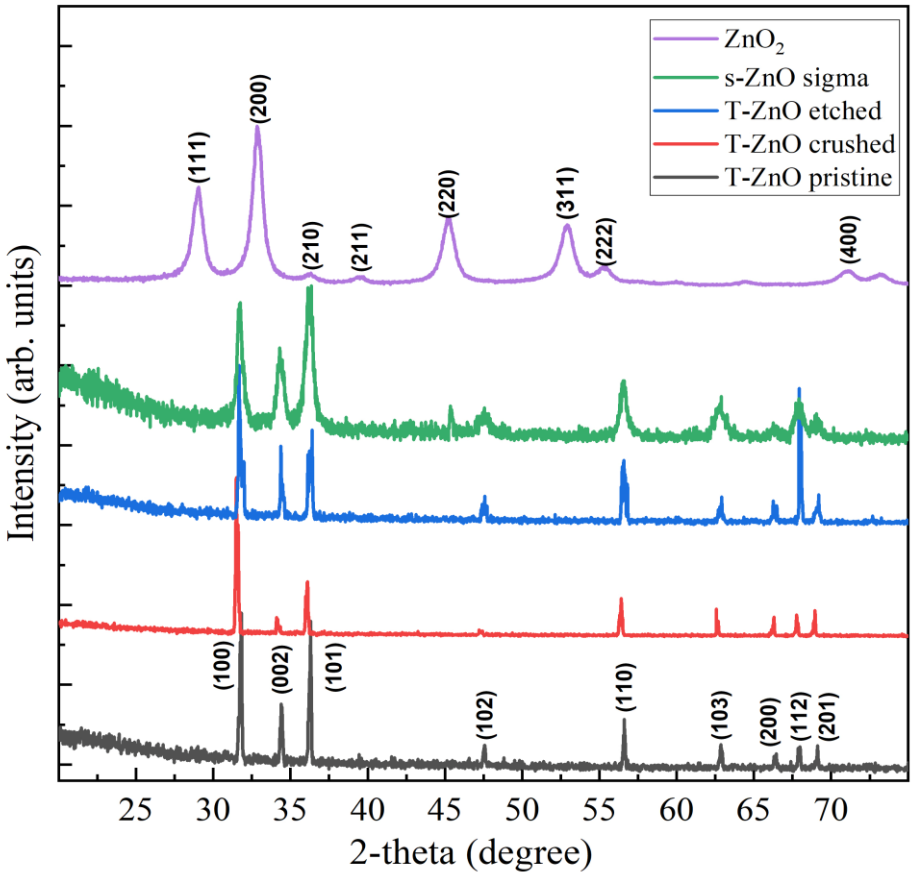

Figure 5.3: XRD patterns of T-ZnO (untreated, crushed, and etched), commercial ZnO, and ZnO_2 NPs.

There are characteristic peaks for as-prepared, crushed, and etched T-ZnO corresponding to (100), (002), and (101) planes at angles 31.77°, 34.4° and 36.2°, respectively. All the diffraction peaks agreed well with the peaks of the hexagonal wurtzite phase of ZnO with lattice constant of a = 0.325 nm and c = 0.520 nm when compared with JCPDS file [163]. Moreover, the tetrapods consisted of single phase of ZnO with no other impurity. The sigma ZnO (green spectrum

in Figure 5.3 exhibited the same peaks as tetrapods, with the difference that peaks in sigma nanopowder were broad in width as compared to tetrapodal zinc oxides. The purple spectrum showed the XRD pattern of ZnO_2 nanoparticles (Figure 5.3). This pattern depicted the crystal structure and phase purity of synthesized zinc peroxide nanoparticles. The XRD pattern revealed distinct reflections at 2θ = 31.79°, 36.87°, 53.0° and 63.0° (indexes: 111, 200, 220 and 311). These peaks matched well with the cubic structure ZnO_2 (JCPDS card No. 13-0311). The sharp diffraction peaks indicated the good crystallinity of nanoparticles. In addition, the absence of the ZnO characteristic reflection at 2θ =34.422° implied the solely formation of ZnO_2 nanoparticles [115].

5.4. Transmission electron microscopy of ZnO_2 NPs

The morphology and particle size of the ZnO_2 nanoparticles were also investigated through TEM. Bright-field images of the particles are given in Figure 5.4 a, b and c. The shape of the particles was found to be spherical. Particles had a range in particle size of approximately 50-300 nm (type 1) and 20-80 nm (type 2). In the case of 50-300 nm sized particles, good dispersion of nanoparticles on the TEM grid was observed (Figure 5.4 a). However, in the case of 20-80 nm sized particles, NPs were found to be mostly agglomerated (Figure 5.4 c), and distinct particles were rarely observed.

Electron diffraction (representative selected area electron diffraction (SAED) pattern given in Figure 5.4 d, confirmed the formation of ZnO. The diffuse intensity on concentric rings indicated a nanocrystalline structure. The extracted *d*-values of 2.608 Å and 1.913 Å can be assigned to (002) and (012) lattice planes of hexagonal ZnO (literature values: 2.6033 Å for (002) and 1.9111 Å for (012) [164] .

The Z-contrast of the STEM HAADF image combined with the EDX line scan data (Figure 5.4 e) supported the assumption that the particles were hollow. No significant change in chemical composition across the particle can be observed in the line scan. Quantification of EDX spectra acquired from the shell-region of the particle resulted in 54 ± 5 atomic % Zn and 46 ± 5 atomic % O. For spectra from the core region the quantification results in 49 ± 2 atomic % Zn and 51 ± 2 atomic % O. The differences in chemical composition are within the margin of error. The darker contrast in the center of the particles (STEM HAADF, Figure 5.4 e) consequently results from a lower effective thickness in the center of the hollow particle.

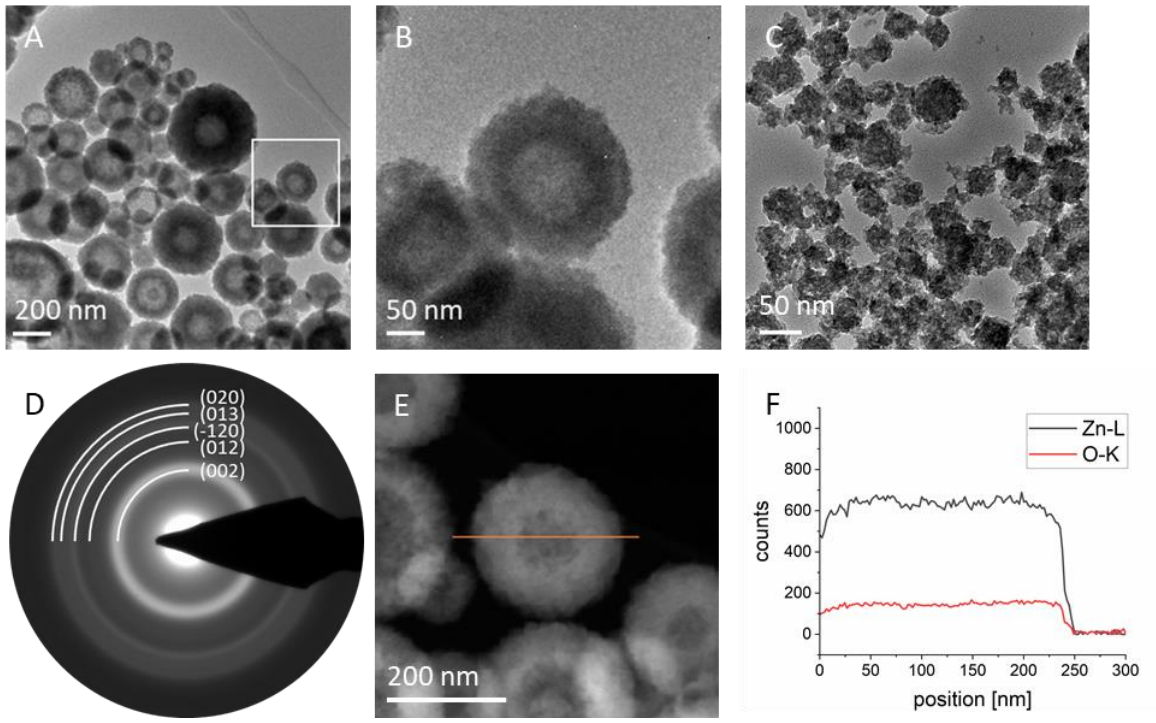

Figure 5.4: TEM images of unloaded nanoparticles with sizes of 50-300 nm and 20-80 nm are shown in TEM bright-field images (A) and (C), respectively. The area of the white square in (A) is depicted in (B) at a larger magnification for particle size in comparison with (C). The SAED pattern (D) indicates the presence of hexagonal ZnO phase. The orange line in the STEM HAADF image (E) marks the path of the EDX line scan. The counts for Zn and O from the line scan in (E) are plotted in (F). The 0 nm position in the plot is chosen to be the edge of the particle.

The Energy Dispersive X-ray Diffractive (EDX) study was performed for the zinc peroxide nanoparticles to be acquainted with the elemental composition. EDX spectra confirmed the presence of zinc and oxygen signals from zinc peroxide nanoparticles, as shown in Figure 5.5 (b, d). The elemental analysis of the nanoparticles yielded some Cu and Carbon signals which might come from Cu TEM grid and carbon support.

5.5. Transmission electron microscopy of DOX loaded ZnO_2 (20-80 nm) nanoparticles

The morphology and particle size of drug-loaded ZnO_2 nanoparticles were also investigated through TEM. Bright-field images and EDX spectra of the particles are given in Figure 5.6 (a-c). The drug loading did not affect the spherical shape and size of the particles. Particles had a range in particle size of approximately 20-80 nm.

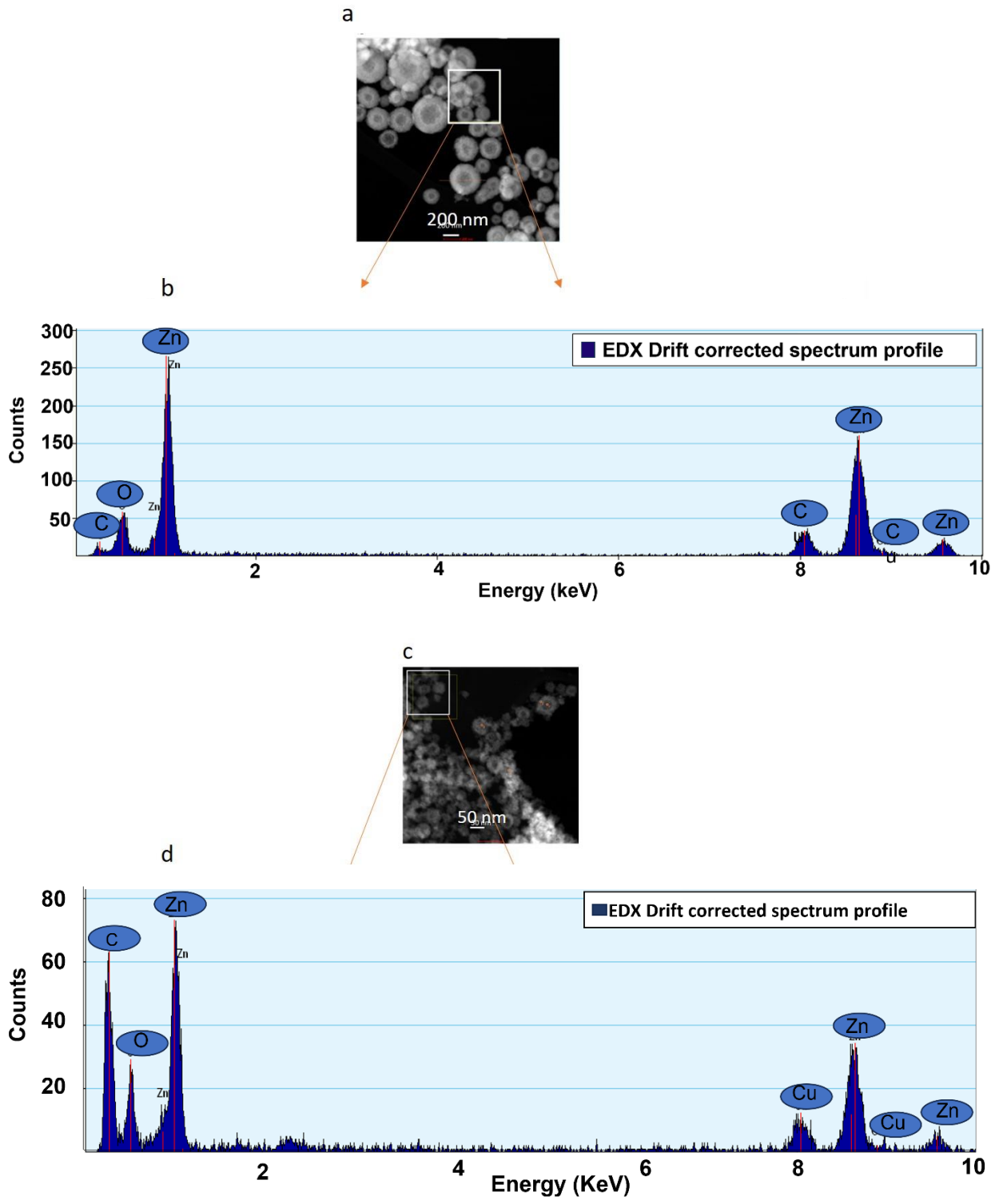

Figure 5.5: The EDX spectra of ZnO_2 nanoparticles with sizes of 50-300 nm (b) of the area of the white square in (a) and the EDX spectra of ZnO_2 nanoparticles with sizes of 20-80 nm (d) of the area of the white square in (c).

Like bare ZnO_2 particles, drug-loaded particles have the tendency to form hollow spheres (Figure 5.6 d). However, the EDX spectrum of drug-loaded nanoparticles did not show any element that is unique for the loaded drug (Figure 5.6 c).

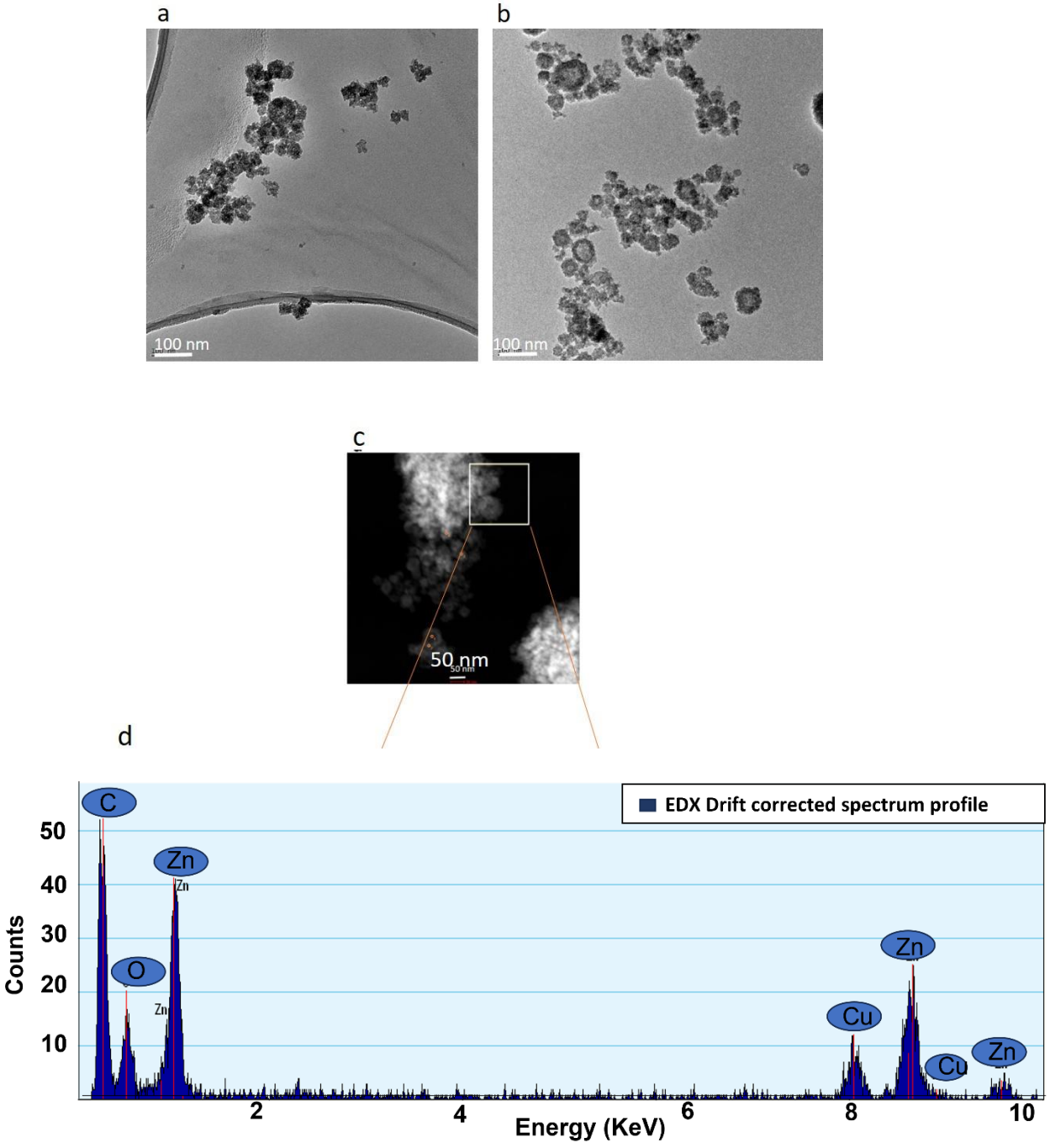

Figure 5.6: (a, b) TEM images of Doxorubicin-loaded nanoparticles with sizes of 20-80 nm are shown in TEM bright-field images (c,d). The EDX spectra of drug-loaded ZnO_2 nanoparticles with sizes of 20-80 nm (d) of the area of the white square in (c).

5.6. Cytotoxicity tests

Cytotoxicity of ZnO_2 and T-ZnO nanoparticles was performed by using the ApoLive-Glo™ Multiplex Assay. This assay measures the activity of a protease marker of cell viability. The live-cell protease activity is restricted to intact viable cells and is measured using a fluorogenic, cell-permeant peptide substrate (glycyl-phenylalanyl-amino fluorocoumarin; GF-AFC). The substrate enters intact cells, where it is cleaved by the live-cell protease activity to generate a fluorescent signal proportional to the number of living cells.

5.6.1. Cytotoxicity tests of ZnO_2 NPs and T-ZnO for MCF-7 and RMF-EG fibroblasts

The obtained results of ZnO_2 nanoparticles for the MCF-7 and RMF-EG fibroblasts cell lines are shown in Figure 5.7 a–b, respectively. ZnO sigma nanoparticles were used as a reference for both cell types. It can be seen from Figure 5.7 that the cytotoxicity of the nanoparticles mainly depends on the cell type used and the particle size. With MCF-7 cell suspensions, all particle types and sizes created a more pronounced toxic effect and caused more cell death than RMF-EG cell suspensions (Figure 5.7 a–b).

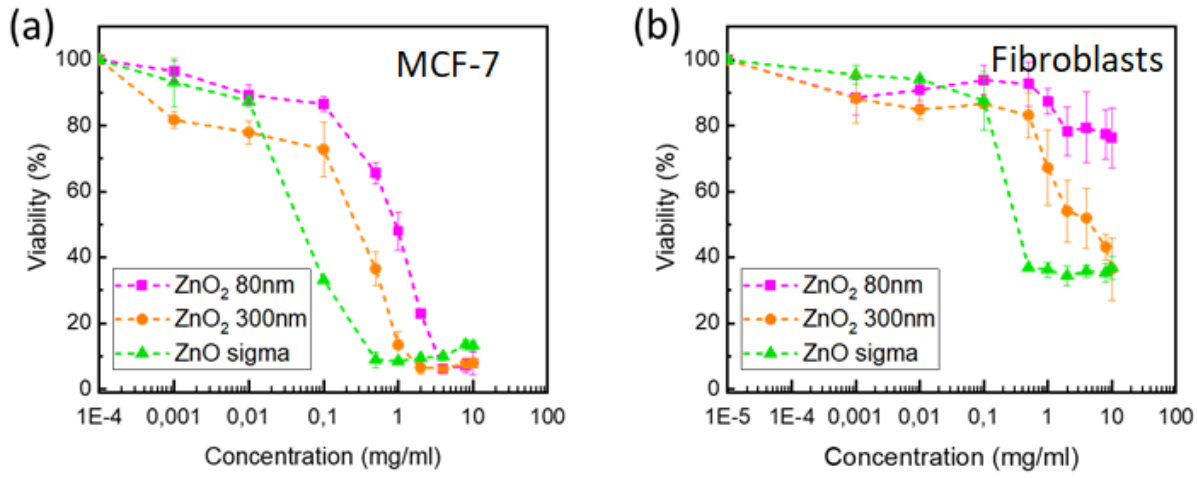

Figure 5.7: Effect of ZnO_2 nanoparticles (a) on cell viability of human breast cancer cells (MCF-7) (b) on normal fibroblasts determined by ApoLive-GloMultiplex Assay. Passage number: P15–P25. Seeded cell numbers: 17000 cells/cm^2 for MCF-7 and 10,000 cells/cm^2 for RMF-GE; Particle concentration: 0.001–10 mg/ml; duration of treatment: 48 h. Each symbol represents the mean ±SE of n=3 independent experiments with three-fold determinations.

In the case of MCF-7 cells, the obtained results (Figure 5.7 a) for ZnO_2 nanoparticles showed that particles of both sizes demonstrate an initial gradual decrease in percentage cell viability up to a concentration of 0.1 mg/ml followed by a rapid drop in the range 0.1-2.0 mg/ml. After this decline, both particles exhibited nearly constant cell viability values (approximately 7-12 %). Furthermore, 50-300 nm sized particles produced a slightly more toxic effect (IC50 =0.3 mg/ml) than the particles of size 20-80 nm (IC50 = 0.7 mg/ml). These findings showed a contradiction with the results reported for other cancer cells [121], such as Jurkat and U937 for which small particle size of ZnO_2 caused more cell death.

The cytotoxic concentration range of commercial ZnO is close to the cytotoxic range of both ZnO_2 particles, with a difference that commercial ZnO produced a significant toxic effect at values of 0.1 and 0.5 mg/ml (Figure 5.7 a). However, below or above these concentrations, the curve of commercial ZnO followed the trend of ZnO_2 nanoparticles. The mean IC50 value obtained for commercial ZnO was found to be 0.042 mg/ml, which is comparable with the IC50 values reported in other studies (in the range of 0.02–0.05 mg/ml) for spherical ZnO nanoparticles [47,165] .

In the case of RMF-GE, ZnO_2 (20-80 nm) nanoparticles showed an overall lower toxic effect (Figure 5.7 b), and fibroblasts showed around 76 % viability at the highest concentration of 10 mg/ml. However, the 50-300 nm-sized ZnO_2 nanoparticles showed a higher toxic effect at concentrations above 0.5 mg/ml. Cell viability of 50-300 nm-sized particles was 36.7 % at 10 mg/ml, which is sufficiently higher than the cell viability (7.9 %) of MCF-7 cells at 10 mg/ml. This means that 50-300 nm-sized particles also affect RMF-EG less than MCF-7; however, the effect is higher than 20-80 nm-sized ZnO_2. Commercial ZnO showed a pronounced toxic effect on fibroblasts at concentration of 0.5 mg/ml and above (Figure 5.7 b). After this decline, the cell viability of fibroblasts remained constant between 0.5-10 mg/ml concentration.

5.6.2. Cell culture of tetrapods (T-ZnO) for MCF-7 and RMF-EG fibroblasts

The cytotoxicity of T-ZnO exhibit different profiles compared to spherical nanoparticles, as shown in Figure 5.8. For MCF-7 cell suspensions (Figure 5.8 a), all types of tetrapods displayed almost negligible cytotoxicity for a concentration range of 0-1.0 mg/ml; after that, a slow reduction in cell viability was observed. As shown in Figure 5.8 a that O_2 treatment (etching) and crushing of tetrapods have led to some changes in their cytotoxic behavior. Crushed T-ZnO reduced the viability of MCF-7 relatively more than O_2-treated (etched) and untreated (intact) T-ZnO. Around

30% of the cells were viable for a maximum concentration of 10 mg/ml of crushed tetrapods. While intact and etched tetrapods displayed 45 % and 60 % cell viability, respectively, at the highest tetrapods concentration (10 mg/ml). Interestingly, for fibroblasts cell suspensions (Figure 5.8 b), all types of T-ZnO (crushed, Intact and etched) showed almost the same cytotoxic behavior as that for MCF-7. Crushed T-ZnO displayed 36.9 % viability at 10 mg/ml. Intact and O_2-treated T-ZnO showed 45.3 % and 66.9 % cell viability at 10 mg/ml concentrations.

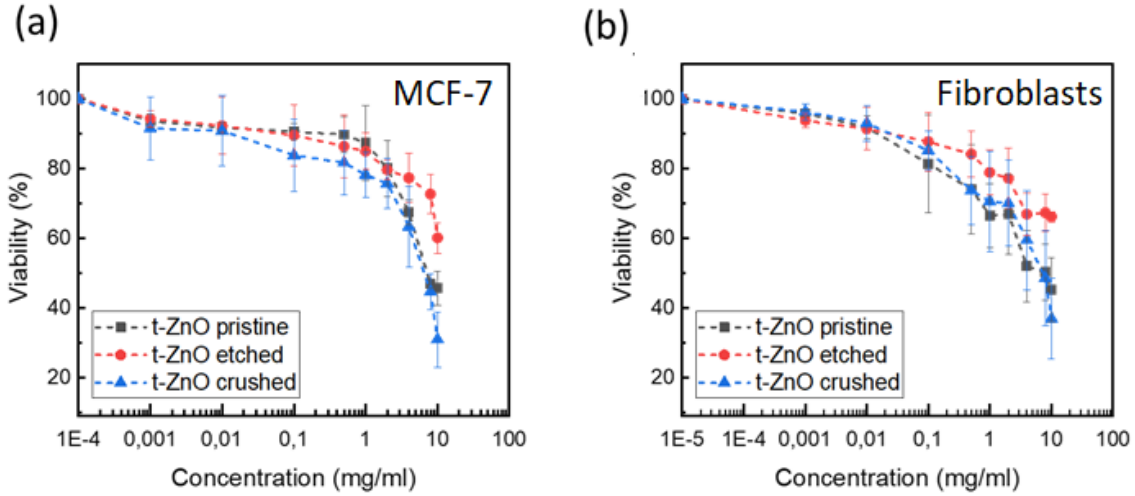

Figure 5.8: Effect of ZnO tetrapods (a) on cell viability of human breast cancer cells (MCF-7) (b) on normal fibroblasts determined by ApoLive-GloMultiplex Assay. Passage number: P15–P25. Seeded cell numbers: 17,000 cells/well for MCF-7 and 10,000 cells/well for fibroblasts; Particle concentration: 0.001–10 mg/ml; duration of treatment: 48 h. Each symbol represents the mean ±SE of n=3 independent experiments with three-fold determinations.

Overall, by comparing the cytotoxicity of T-ZnO with sigma ZnO and ZnO_2 NPs, we found that the cytotoxic potency of ZnO tetrapods was clearly lower than those of spherical NPs for both MCF-7 as well as for RMF-EG.

5.6.3. Discussion (Cytotoxicity tests)

The generation of reactive oxygen species is the one reason for the cytotoxicity of ZnO_2 nanoparticles. In general, the generation of more reactive oxygen species with decreasing nanoparticle size is expected [121]. However, the opposite was true for ZnO_2 particles' toxicity towards RMF-EG (Figure 5.7 b). This may be described by the fact that cytotoxicity depends on the cell type in addition to nanoparticle characteristics. In the case of MCF-7 cells, it was found

that ZnO_2 particles of both sizes reduced the cell viability by inducing oxidative stress without any significant difference in the same concentration range (0.001–10 mg/ml). This also showed that the cytotoxicity of nanoparticles depends on the target cells' type.

As far as cytotoxicity of T-ZnO is concerned, a possible reason for cell toxicity of all types of T-ZnO is the presence of needle-like sharp kinks of tetrapods which may damage the cell membrane, thereby causing cell death.

As demonstrated in Figure 5.8, Table 1, and Table 2, crushed T-ZnO exhibited higher cytotoxic effect than untreated tetrapods in both MCF-7 and RMF-EG. Multiple mechanisms can describe this: Breaking of tetrapod arms and increasing surface area after crushing, supported by recent studies on cytotoxicity of nano and micro-sized ZnO structures towards different cells [166]. Another reason might be the existence of more defected sites in crushed/broken areas due to a lack of high symmetric crystal direction [130].

Table 1: Impact of nanoparticles and ZnO tetrapods (T-ZnO) on IC50 values for MCF-7 cells

Sample	**20-80 nm ZnO_2**	**50-300 nm ZnO_2**	**Sigma ZnO**	**Untreated T-ZnO**	**Crushed T-ZnO**	**Ethched T-ZnO**
IC50 (mg/ml)	0.730	0.182	0.042	6.404	6.272	Not reached

Table 2: Impact of nanoparticles and ZnO tetrapods (T-ZnO) on IC50 values for RMF-EG cells

Sample	**20-80 nm ZnO_2**	**50- 300 nm ZnO_2**	**Sigma ZnO**	**Untreated T-ZnO**	**Crushed T-ZnO**	**Ethched T-ZnO**
IC50 (mg/ml)	Not reached	0.8794	0.1673	7.822	7.52	Not reached

Our results also suggested that inducing surface reactivity by O_2 treatment (etching) also affects the cytotoxic behavior of T-ZnO. According to previous reports, O_2 treatment of ZnO switches its

wetting behavior from hydrophilic to hydrophobic [167,168] as a result of passivation of oxygen vacancies. The negative surface charges of ZnO are neutralized by this O_2 saturation which may lead to the lower solubility of neutralized T-ZnO, which decreases its bioavailability. In the current case, for MCF-7 and RMF-EG, O_2-treated T-ZnO displayed lower cytotoxicity due to reduced solubility in the cell culture medium. However, a previous study of T-ZnO cytotoxicy on normal human dermal fibroblasts (NHDF) cells by Papavlassopoulos et al. [130] reported that no significant changes in cytotoxicity occurred after O_2 or UV light treatment of ZnO structures. Again, this could be attributed to the cell type used and the applied cell culture system.

A comparison of cytotoxicity of nanosized spherical particles (ZnO_2 and ZnO) with T-ZnO clearly indicated that for MCF-7 cells, spherical NPs exhibited higher cytotoxic potency than those of T-ZnO. This can be supported by the fact that nanoparticles owing to their small size can be easily internalized by cells. NPs enter cells through clathrin-independent endocytosis and then end up in the acidic lysosomes of the cells. In the lysosomal section, they dissolve to release the Zn^{+2} ions [169,170] causing cell death. In contrast to nanoparticles, T-ZnO cannot be taken up by cells due to nano-micro scale dimensions. Thus, they cannot exhibit direct intracellular cytotoxic effects, and cell death is caused by cell membrane damage due to sharp tetrapods arms.

Taken together, these findings led to the presumption that changes in materials size, surface properties, and cell type used might have been responsible for their variable cytotoxic effects. Among these six ZnO materials, ZnO_2 of size 20-80 nm gave the most effective desired result i.e., effective against MCF-7 cells and showed minimal toxicity to normal fibroblasts (RMF-EG) cells. Thus, 20-80 nm particle size was used in further experiments.

5.7. Zinc ion release from ZnO and ZnO_2 micro and nanostructures

When ZnO NPs interact with the cancer cells, first they are taken up by the cell through endocytosis. NPs enter the cell through phagocytosis and pinocytosis bounded by endosomes and lysosomes. As the pH level inside the cancer cell decreases, ZnO dissolution rate increases rapidly, causing lysosomal destabilization [138]. The pH of early endosome is relatively low (around 6.3). It further drops to pH 5.5 in late endosome at pH 4.7. This suggests that low pH value is necessary for the release of zinc ions. Hence the zinc ion release in blood or extracellular fluid (pH value of 7) is not favorable [26]. This process results in an increased release of zinc ions inside the cancer cell. The increase of zinc ions also increases reactive oxygen species (ROS) concentration, leading to

cytotoxicity towards cells via oxidative stresses [22]. This selective cytotoxicity of ZnO against cancerous cells in in vitro conditions makes them a promising anticancer agent.

5.7.1. Zn^{+2} ions release in different pH media

ZnO_2 NPs and T-ZnO dispersed in PBS and cell culture medium with pH 7.4 and 7.2, respectively, were adopted to estimate Zn^{+2} ions release in the normal physiological environment. Acetate buffer (pH 5.5) was used to estimate Zn^{+2} ions release in lysosomal section of the cancer cell. Figure 5.9 showed that both ZnO_2 NPs (20-80 nm and 50-300 nm) and T-ZnO released around 360-380 µg/ml of Zn^{2+} ions at pH 5.5. No significant difference was found in the released amount of zinc ions from spherical particles and tetrapods at specific pH value. It can also be seen in Figure 5.9 that ZnO_2 NPs and T-ZnO (feeding concentration 1 mg/ml) can release Zn^{2+} ions in the cell culture medium (pH 7.2) and PBS (pH 7.4) in a very low amount and reached a concentration of around 9-11 µg/mL after 24h of incubation. In comparison, the solubility of all types of particles in lysosomes-mimicking medium (pH 5.5) was significantly higher (Figure 5.9), resulting in around 360 µg/ml-380 µg/ml Zn^{2+} concentration. These results suggested that the release of Zn^{+2} is strongly pH-dependent, and the size and shape of particles did not seem to affect the release under these experimental conditions.

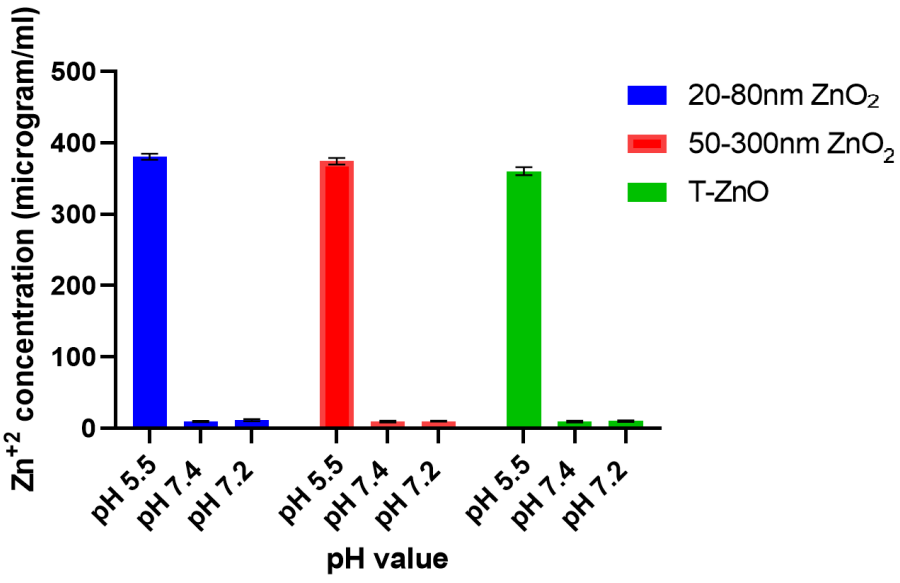

Figure 5.9: Release of Zn^{2+} ions from different ZnO structures in buffer solutions and culture medium at pH 7.4, 5.5 and 7.2.

5.8. Assessment of zinc ions released into MCF-7 cells

Figure 5.10 a showed the single-staining of zinquin uptake study by the MCF-7 cells. It can be seen in the figure that when there is no particle treatment, the staining intensity of zinquin is only 11527 a.u. The zinquin intensity dramatically increased after the 2h of incubation with ZnO_2 nanoparticles (20-80 nm) to 37,280 a.u. After 4 h of incubation, the zinquin intensity was around 32,834 a.u which is a bit less than 2h incubation but still much higher than with no particle treatment.

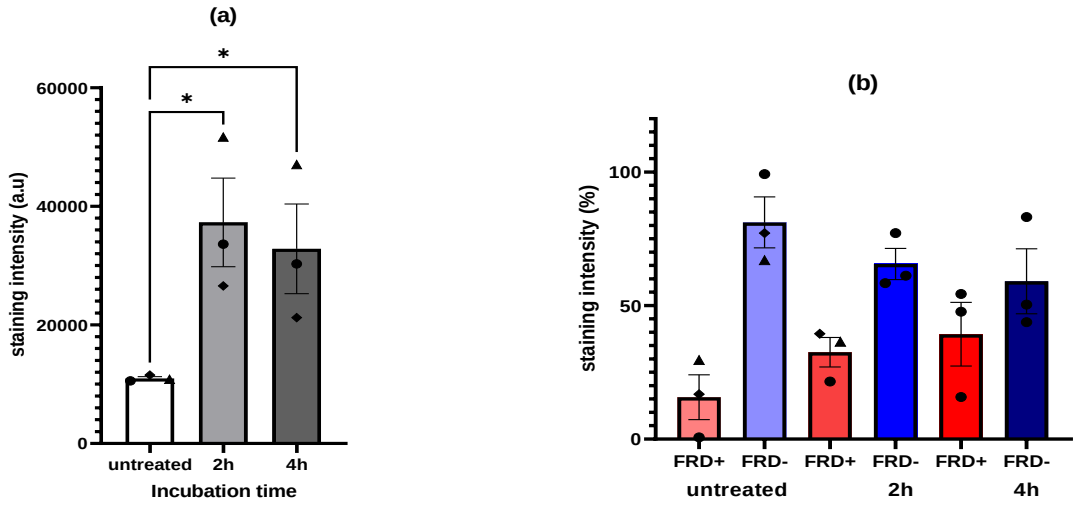

Figure 5.10: (a) Staining intensity of zinquin alone without and with ZnO_2 nanoparticles treatment for 2h and 4h (b) Percentage dead (FRD+) and alive cells (FRD-) compare without and with ZnO_2 nanoparticles treatment for 2h and 4h.

This increase in staining intensity of zinquin after 2 h and 4 h of ZnO_2 incubation is due to the intracellular release of zinc ions and subsequent cell death. The slightly low zinquin intensity for 4 h treatment time as compared to 2 h might be due to the penetration of some amount of zinquin out of the cells after 4h due to damaged cell membranes of dead cells. Figure 5.10 b showed the staining intensity percentage of FRD+ (dead cells) and FRD- (living cells) of untreated cells and ZnO_2-treated cells for 2h and 4h. The intensity of dead cells (FRD+) for untreated cells is very low (around 15 %). However, the intensity of alive cells (FRD-) was as high as 81.16 % for untreated cells. After 2 h of treatment with ZnO_2 nanoparticles, it can be seen that dead cell intensity was increased up to 32.5 % while the intensity of living cells dropped from 81.16 % to 65 %. This confirmed the cell death increase after incubation of ZnO_2 nanoparticles due to intracellular Zn^{+2}

ions release. After the 4 h of incubation, a further dead cell intensity increase of up to 40 % was observed while the living cells intensity further decreased to 59 %. These results indicated that the incubation of cells with 1 mg/ml of ZnO_2 nanoparticles preceded the cell death of MCF-7 cells.

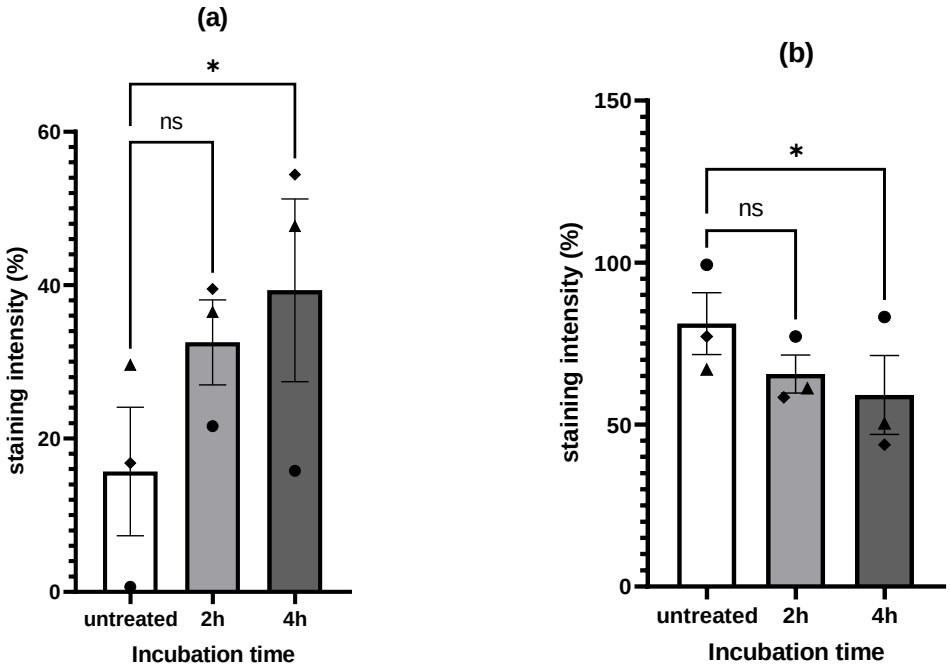

Figure 5.11: (a) Percentage dead cell (FRD+ staining intensity) compare of untreated and ZnO_2-treated cells for 2h and 4h (b) percentage alive cell (FRD- staining intensity) compare of untreated and ZnO_2-treated cells for 2 h and 4 h.

Figure 5.11 (a , b) depicts the percentage of dead cells and alive cells comparison. It was observed in Figure 5.11 a that the untreated cells have only 15 % of dead cell (FRD+) intensity which was increased after 2 h and 4 h of incubation with ZnO_2 nanoparticles. The percentage of alive cells presented the opposite behavior, i.e., the percentage intensity of alive cells decreases after the 2 h and 4 h treatment of ZnO_2 nanoparticles.

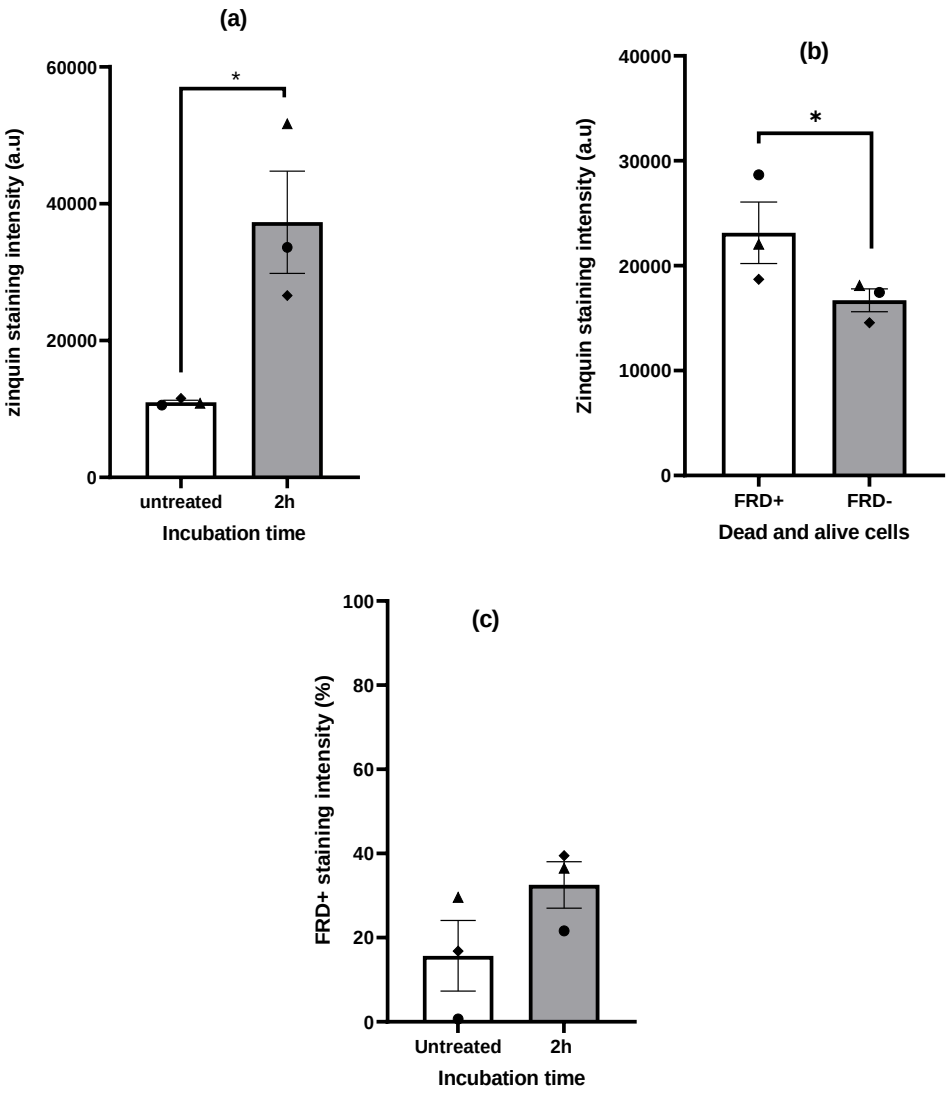

Figure 5.12: (a) Uptake of ZnO_2 particles in terms of staining intensity of zinquin for untreated and after 2 h of incubation with NPs (b) Staining intensity of zinquin for dead (FRD+) and alive (FDR-) cells (c) Percentage of staining intensity of dead (FRD+) cells with (2 h incubation) and without ZnO_2 NPs treatment.

The uptake of ZnO_2 NPs was studied with no particle treatment and at 2 h of time interval in terms of staining intensity of zinquin (Figure 5.12 a). Cells treated with the particles for 2 h showed higher uptake than cells with no ZnO_2 NPs treatment. The staining intensity of zinquin (indicating the presence of zinc ions inside cells) with no particle treatment displayed a staining intensity of 11527 a.u. However, cells treated with ZnO_2 particles for 2 h, showed the average zinquin staining intensity of 37,280 a.u, which depicted the higher intracellular zinc ions concentrations after 2h incubation.

Figure 5.12 b showed the zinquin staining intensity for FRD+ (dead cells) and FRD- (alive cells). It can be seen in the figure that in case of dead cells (FRD+), the staining intensity of zinquin (23137 a.u) is higher than that of alive (FRD-) cells (16705 a.u) after 2 h of incubation with ZnO_2 nanoparticle. This means that the dead cell percentage after nanoparticle treatment is higher than that of live cells.

The percentage of dead cells compared to no particle treatment after 2 h of incubation with particles is shown in Figure 5.12 c. The number of dead cells were investigated by measuring the percentage of staining intensity of dead cells (FRD+). Figure 5.12 c showed that the percentage dead cell increased gradually after 2 h of NPs treatment. The untreated MCF-7 cells exhibited 15 % staining intensity of dead cells (FRD+). Treatment with ZnO_2 NPs for 2 h has led to a significant increase (32 %) in FRD+ intensity.

5.8.1. Rise of intracellular Zn^{2+} precedes cell death

In order to correlate intracellular Zn^{2+} ionic release to cell death, dynamic confocal microscopy was applied. Two different dyes (zinquin and FRD) were used to track the Zn^{2+} release and cell death for these experiments. A dose of 1 mg/ml of the zinc peroxide nanoparticles (20-80 nm) was used in experiments to estimate the intracellular Zn^{2+} concentration. Figure 5.13 and Figure 5.14 showed the representative confocal images of the dissolution of ZnO_2 NPs inside MCF-7 cells after 2 h and 4 h of incubation. Figure 5.13 (a–d) showed the intracellular zinc ion release inside the cells over time. After 2 h and 4 h of exposure to ZnO_2 nanoparticles, the ZnO_2 was dissolved, releasing ionic zinc (Zn^{2+}) (Figure 5.13 c,d). This release of ionic zinc (Zn^{2+}) was accompanied by an increase in the intensity of Zinquin (purple) inside the cells, which was clear after 2 h of exposure (Figure 5.13 c). This rise in intracellular zinc is correlated to cell death, as indicated by FRD (red) penetration into the cells (Figure 5.14 b, c). FRD release was always preceded by zinquin release or co-occurred as Zinquin release. Analysis of the cells after exposure to the ZnO_2 showed that 32 % of cells in the imaging field died as early as 2 h exposure, and almost 40 % of cells died after 4 h of exposure (see Figure 5.10, Figure 5.11 and Figure 5.12). Analysis of the confocal data shown in Figure 5.13 and Figure 5.14 was used to produce representative intensity bar graphs of Zinquin and FRD. The bar graphs of Zinquin and FRD from the cells exposed to the ZnO_2 NPs showed an sharp rise in Zinquin intensity over a time period of 2 h (Figure 5.10 a) and a gradual increase in FRD+ once a significant concentration of Zn^{2+} is reached (Figure 5.10 b). On the other hand, the untreated control MCF-7 cells imaged under the same conditions did not show any increase in

intracellular Zn^{2+} during the confocal imaging experiments. This confirmed that the Zn^{2+} indicator did not fluoresce over either 2 h or 4 h, in the absence of zinc (Figure 5.13 a, b, Figure 5.14 a).

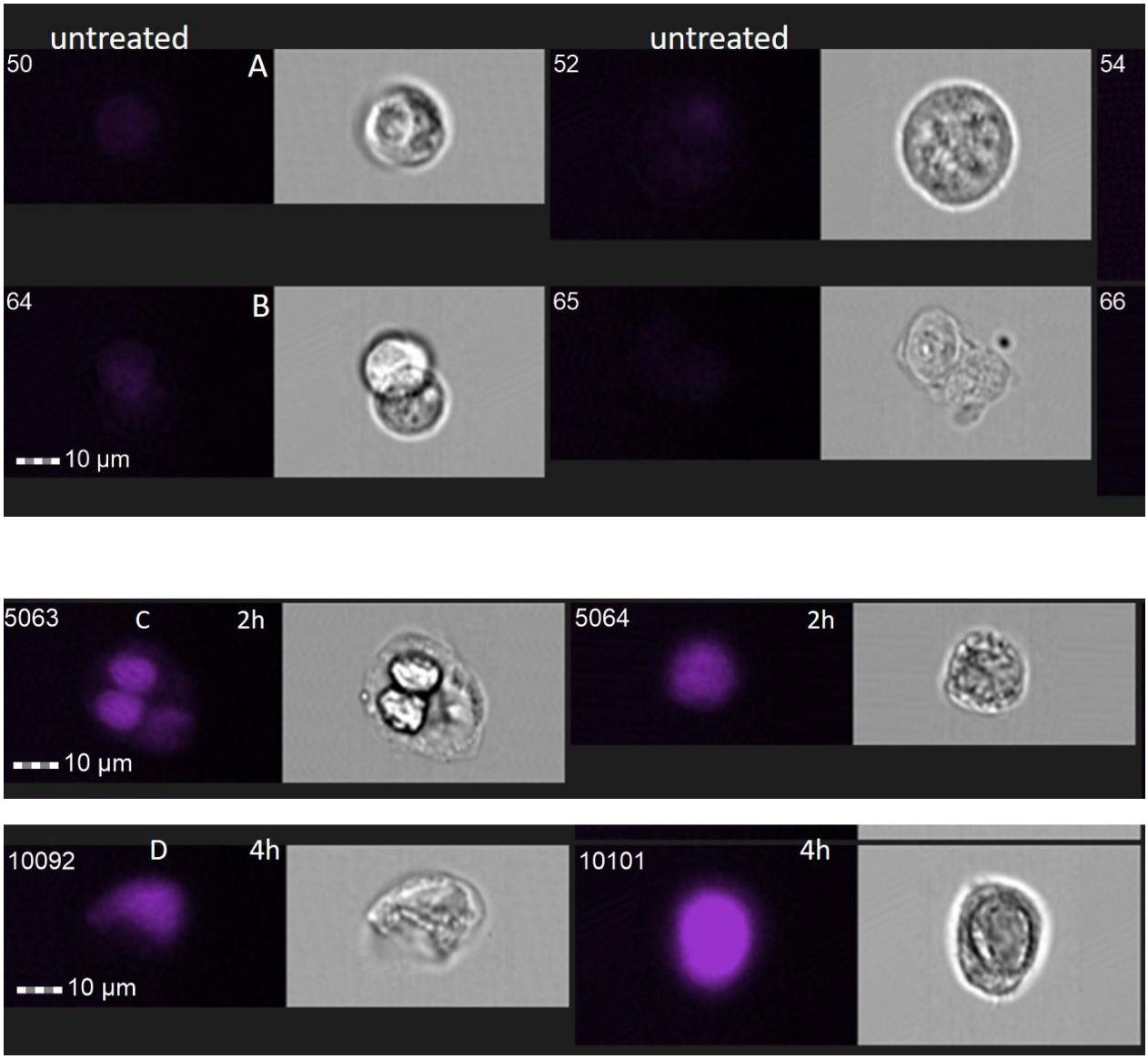

Figure 5.13: (a–d) Bright field and confocal images of MCF-7 cells untreated (a, b) and exposed to 1mg/ml ZnO_2 NPs (c, d) showing the release of Zn^{2+} inside the cells over time (2 h and 4 h) as indicated by the increase in the intensity of the Zn^{2+} indicator, zinquin.

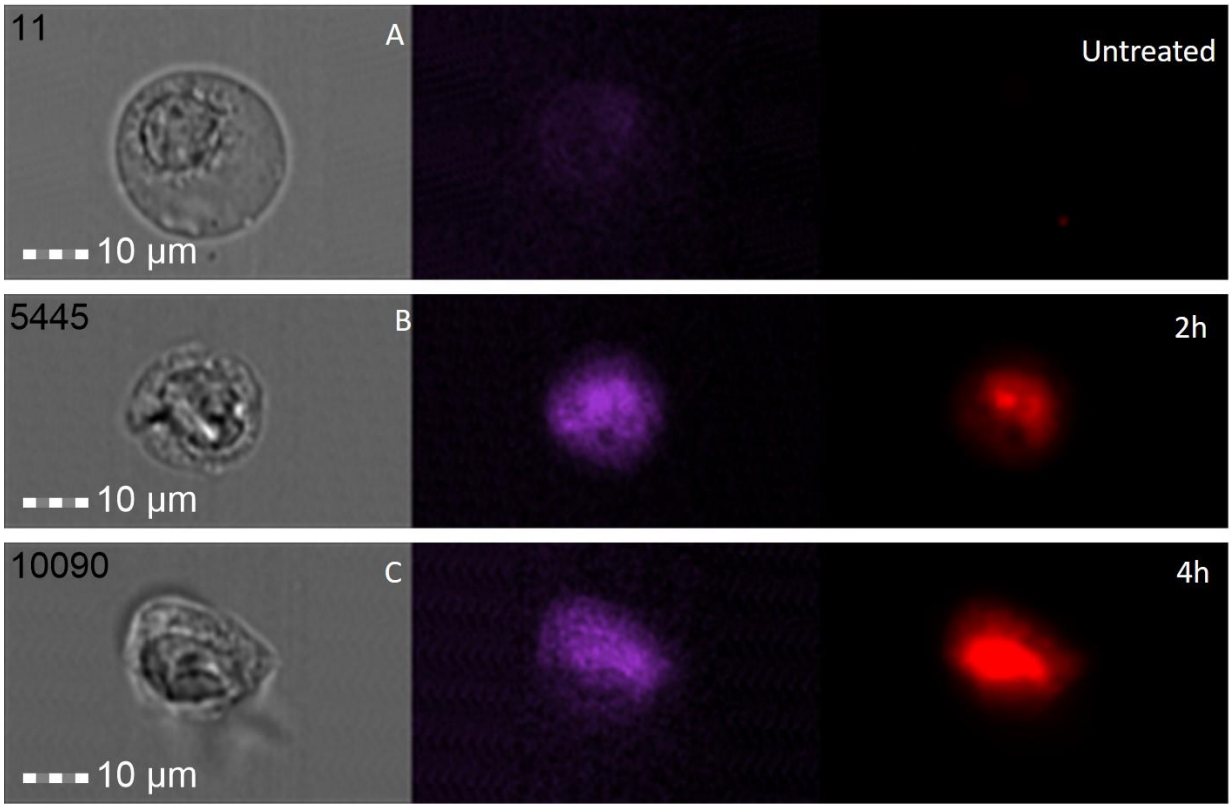

Figure 5.14: (a–c) Bright field and confocal images showing MCF-7 cells (a) untreated and exposed to 1 mg/ml of the ZnO_2 NPs led to the release of Zn^{2+} inside the cells over time; (b) 2 h and (c) 4 h, as indicated by the increase in the intensity of the Zn^{2+} indicator, Zinquin (purple). Toxic levels of Zn^{2+} ions inside the cell subsequently resulted in cellular penetration of FRD (red), indicating the loss in viability and cell death.

5.8.2. Discussion (Zn ions release into MCF-7 cells)

The agents targeting and killing cancer cells are of great importance. ZnO_2 NPs are attractive compared to other nanomaterials due to their selective killing of cancer cells [121]. The data from the current study showed that bare ZnO_2 nanoparticles were toxic to MCF-7 breast cancer cells. These findings are in line with previous work presenting that the release of Zn^{2+} ions, following incubation of ZnO nanoparticles with MCF-7 cells, initiates the production of reactive oxygen species, destroying the plasma membrane [58]. For the first time, the results also demonstrate that ZnO_2 NPs are internalized by MCF-7 cells and show toxicity at 1 mg/ml dosage of particles after 2 h and 4 h of exposure, respectively. The more significant toxicity of the ZnO_2 NPs could be attributable to a greater amount of particles internalization (and hence Zn^{2+} ion release). This finding of the ZnO_2 NPs to effectively kill MCF-7, accounts for a high percentage of breast cancer

mortality due to the nonexistence of effective therapies [171], will open new possibilities for ZnO_2 in cancer therapy.

Only a few reports exist on the cellular uptake of ZnO nanomaterials [172,173]. In one study, confocal microscopy has presented that ZnO NPs fragments are internalized by caveolae-mediated uptake in BEAS-2B cells, and Zn^{2+} ions have been shown to accumulate inside the lysosomal compartment of RAW 264.7 cells [174]. Lin et al showed that ZnO NPs with the dosage of 12 μg/ml were agglomerated in endosomes in bronchoalveolar carcinoma-derived cells (A549) after 24 h of exposure [175]. Hong et al. successfully directed fluorescent ZnO nanowires to tumors in vivo by targeting the integrin αvβ3 receptors [176] . But whether the wires were internalized by the cells was not highlighted. Basmah A. Othman. et al showed for the first time (using a Zn^{2+}ion sensitive dye) that an increase in intracellular Zn^{2+} leads to cell death in the MDA-MB-123 cells after exposure to ZnO nanoparticles [177]. Dissolution investigations of bare ZnO nanoparticles without cells in the confocal imaging buffer at pH 7.4 indicated that zinc ion release was <9 μg/ml. Hence, increased intracellular Zn^{2+} on bare ZnO NPs exposure was possible due to the acidic dissolution of ZnO nanoparticles inside the intracellular vesicles and the local Zn^{2+} ions release.

In this thesis, ZnO_2 nanoparticles presented a time-dependent increase in dead cell concentration (Figure 5.14 b, c) and (Figure 5.11 a). ZnO_2 NPs showed a gradual increase in intracellular zinc ion dissolution and ultimately the increase in dead cells. This indicated that ZnO_2 nanoparticles' toxicity in MCF-7 is due to a pH-triggered, intracellular release of Zn^{2+} ions. The ZnO_2 nanoparticles are assumed to be taken up by the MCF-7 cells through clathrin-independent endocytosis. These NPs then end up in the cells' acidic lysosomal (low pH) section, where they disintegrate to release the zinc ions [169,174,178].

5.9. pH-responsive drug release profile of ZnO_2 NPs (20-80 nm)

The cytotoxic medication doxorubicin (DOX) has been employed in traditional cancer therapy. Still, it has severe side effects as the processes it exhibits are usually shared by both cancerous and normal cells. As a result, both types of cells are destroyed by cytotoxic medications [65]. ZnO NPs are considered as one of the most effective theranostics agents for cancer treatment. DOX-loaded ZnO NPs have already been evaluated on MCF-7 cell lines, and results indicated their higher cytotoxicity and DOX released in a controlled manner [65].

The percentage release of doxorubicin (DOX) from ZnO_2 nanoparticles (20-80 nm) was measured in different pH values at several time intervals (Figure 5.15) using Ultraviolet–visible (UV-vis) spectrophotometric method. Two different pH values (endosome pH 5.5, physiological pH 7.4) were taken to experiment. It can be seen that 87.6 % drug was burst released within a period of 24 h at pH 5.5. This can be attributed to the rapid dissolution of ZnO_2 NPs in an acidic environment [24]. In comparison, only 14.6 % release occurred at pH 7.4 after 24 h. After this initial brust, ZnO_2 particles showed the extended drug release up to 72 h. After 72 h, the particles showed 90.7 % and 7.3 % drug release at pH 5.5 and 7.4, respectively. These results are in line with our results of Zn^{+2} ions release study in buffer solutions of different pH (section 5.7.1).

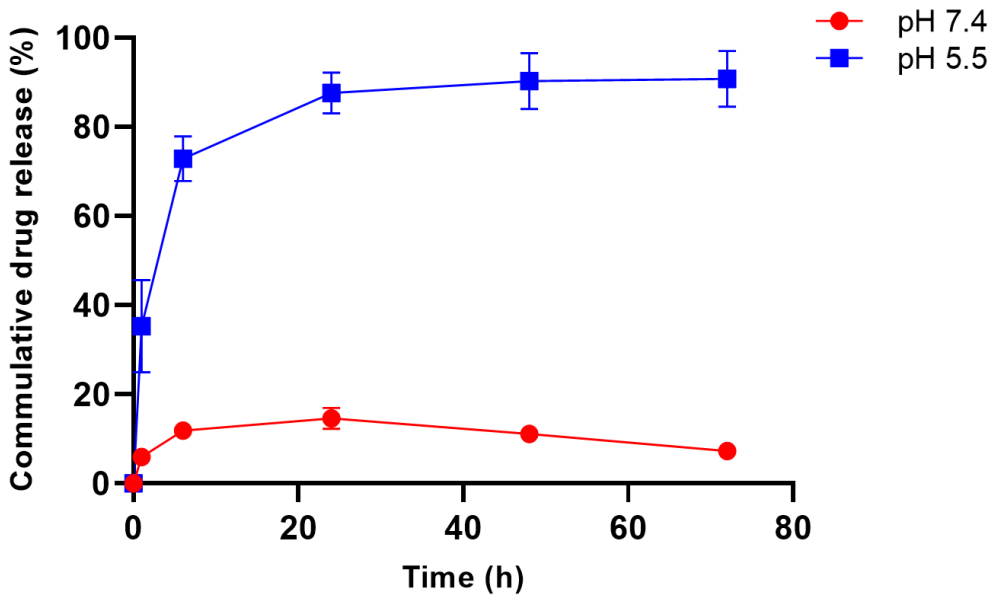

Figure 5.15: Cumulative drug release profile of drug loaded ZnO_2 nanoparticles (20-80 nm).

These results indicated that DOX-loaded ZnO_2 NPs exhibited a typical sustained drug release profile over a 72 h time at 37 °C (Figure 5.15). Also, ZnO_2 nanoparticles could be effectively used as a pH-responsive drug delivery system for DOX.

Since the in vivo tumor places and inside endosome/lysosome of cells exhibit acidic microenvironment (pH 4.5-5.5) whereas the bloodstream is neutral, the DOX release at acidic environment can reduce the risk of damaging normal cells during the in vivo circulation of

intravenously injected nanoparticles. Once the nanoparticles accumulate at the tumor site by the EPR effect, the low pH in the endosome and lysosome will benefit on-demand drug release.

5.10. Impact of bare and drug-loaded ZnO_2 NPs (20-80 nm-sized) on cell viability of MCF-7 cells

Figure 5.16 showed the effect of 20-80 nm-sized bare and DOX loaded ZnO_2 NPs concentration (0.001–10 mg/ml) on MCF-7 cell viability. For bare and drug-loaded NPs, the cell viability reduced significantly (from ~98 % to ~6 %) when particle concentration increased from 1 µg/ml to 10 mg/ml.

A difference can also be seen in the percentage cell viability profile of bare and drug-loaded ZnO_2 nanoparticles. It can be seen in Figure 5.16 that there is a significant decrease in cell viability (around 36 %) at the concentration of only 10 µg/ml in the case of drug-loaded nanoparticles. This may be due to the fact that the drug is also taking part in the cytotoxicity, and there exists a combinational effect of drug and zinc ions on MCF-7 cells at the concentration of 10 µg/ml and above. However, the bare nanoparticles showed cytotoxicity mainly due to only zinc ions and the generation of reactive oxygen species (ROS), as discussed in section 5.6.3.

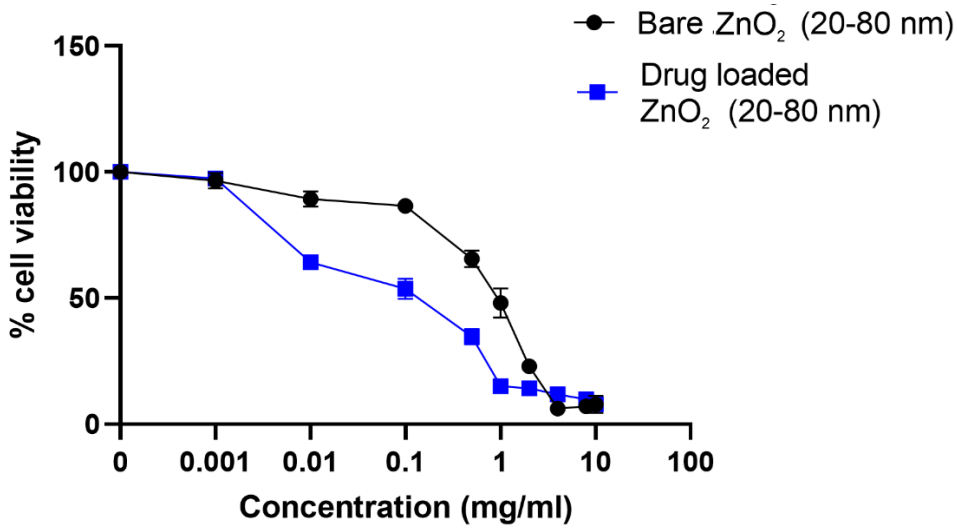

Figure 5.16: Effect of 20-80 nm-sized ZnO_2 nanoparticles (bare and drug-loaded) on cell viability of human breast cancer cells (MCF-7) determined by ApoLive-GloMultiplex Assay. Passage number: P15–P25; seeded cell numbers: 17,000 cells/well; particle concentration: 0.001–10 mg/ml; duration of treatment: 48 h. Each symbol represents the mean ±SE of n=3 independent experiments with three-fold determinations.

These results depicted that ZnO_2 nanoparticles have inherent cytotoxic activity as the cell viability was reduced to around 52 %, at the concentration of 1 mg/ml and around 97 % at 10 mg/ml. Further, it has also been found when the ZnO_2 NPs are loaded with highly active anticancer drug DOX, their activity is significantly increased at low concentrations due to synergistic effect of both cytotoxic agents, i.e., ZnO_2 nanoparticles and DOX. This can also be ascribed to the intracellular release of the DOX even at low ZnO_2 concentrations.

Summary and outlook

In this study, the cytotoxicity of different micro and nanostructured ZnO and ZnO_2 materials was successfully evaluated through a series of experiments. The study has demonstrated that different sized nano ZnO_2 and micro and nano ZnO structures exposed to MCF-7 cancer cells can exert dose-dependent cytotoxicity in vitro. ZnO_2 NPs (20-80 nm) showed more cytotoxicity towards MCF-7 cancer cells as compared to normal fibroblasts RMF-EG. Furthermore, our findings showed that changes in T-ZnO properties by oxygen treatment or crushing lead to a slight change in their cytotoxic behavior. However, other properties like particle morphology and size, shape, and surface area play a significant role. It has also been demonstrated that the ZnO_2 and ZnO NPs (spherical) used in the present study are more toxic to MCF-7 breast cancer cells compared to tetrapodal T-ZnO. The cellular uptake experiments proved the potential of ZnO_2 NPs as a platform capable of delivering a local dose of zinc ions intracellularly. Moreover, ZnO_2 nanoparticles of size 20-80 nm could be effectively used as a pH-responsive drug delivery system for the anticancer drug Doxorubicin.

One potential limitation of this drug delivery system is the release of almost 15 % drug at normal physiological pH of 7.4. This means that some amount of drug can release during the blood circulation process. At present, only the bare nanoparticles without any post-treatment or coating are used in the drug delivery system. However, the non-specific interaction between nanoparticles and blood plasma proteins occurs instantly after NPs enter the blood, resulting in the protein corona formation. These protein-coated nanoparticles then have to interact with the organs and cells. Consequently, the biological responses towards the NPs are changed.

Therefore, a future coating of albumin corona proteins on ZnO_2 NPs would present a very exciting challenge. This will ultimately prolong the blood circulation time and reduce the toxicity of the ZnO_2 NPs. The coating of albumin corona on drug-loaded particles would also potentially reduce the premature release of drug at physiological pH, which would be a useful strategy for optimizing the NPs-based drug delivery system.

Moreover, considering the absence of any relevant study about the toxicity of T-ZnO and ZnO_2 nanoparticles on breast cancer cells, future research on the cytotoxicity effects of aforementioned materials on other breast cancer cells, e.g., MDA-MB-231 would also be an exciting challenge.

Chapter 6: Bibliography

1. Lee, Y. & Thompson, D. H. Stimuli-responsive liposomes for drug delivery. *Wiley Interdiscip. Rev. Nanomedicine Nanobiotechnology* **9**, e1450 (2017).

2. Liu, J. *et al.* Collagenase-encapsulated pH-responsive nanoscale coordination polymers for tumor microenvironment modulation and enhanced photodynamic nanomedicine. *ACS Appl. Mater. Interfaces* **10**, 43493–43502 (2018).

3. Mura, S., Nicolas, J. & Couvreur, P. Stimuli-responsive nanocarriers for drug delivery. *Nat. Mater.* **12**, 991–1003 (2013).

4. James, H. P., John, R., Alex, A. & Anoop, K. Smart polymers for the controlled delivery of drugs–a concise overview. *Acta Pharm. Sin. B* **4**, 120–127 (2014).

5. Villanueva, M. E., Cuestas, M. L., Pérez, C. J., Dall, V. C. & Copello, G. J. Smart release of antimicrobial ZnO nanoplates from a pH-responsive keratin hydrogel. *J. Colloid Interface Sci.* **536**, 372–380 (2019).

6. Etheridge, M. L. *et al.* The big picture on nanomedicine: the state of investigational and approved nanomedicine products. *Nanomedicine nanotechnology, Biol. Med.* **9**, 1–14 (2013).

7. Min, Y., Caster, J. M., Eblan, M. J. & Wang, A. Z. Clinical translation of nanomedicine. *Chem. Rev.* **115**, 11147–11190 (2015).

8. Wagner, V., Dullaart, A., Bock, A.-K. & Zweck, A. The emerging nanomedicine landscape. *Nat. Biotechnol.* **24**, 1211–1217 (2006).

9. Pilati, D. & Howard, K. A. Albumin-based drug designs for pharmacokinetic modulation. *Expert Opin. Drug Metab. Toxicol.* **16**, 783–795 (2020).

10. Grewal, I. K., Singh, S., Arora, S. & Sharma, N. Polymeric nanoparticles for breast cancer therapy: A comprehensive review. *Biointerface Res. Appl. Chem* **11**, 11151–11171 (2021).

11. Matsumura, Y. & Maeda, H. A new concept for macromolecular therapeutics in cancer chemotherapy: mechanism of tumoritropic accumulation of proteins and the antitumor agent smancs. *Cancer Res.* **46**, 6387–6392 (1986).

12. Gerlowski, L. E. & Jain, R. K. Microvascular permeability of normal and neoplastic tissues. *Microvasc. Res.* **31**, 288–305 (1986).

13. Bertrand, N., Wu, J., Xu, X., Kamaly, N. & Farokhzad, O. C. Cancer nanotechnology: the impact of passive and active targeting in the era of modern cancer biology. *Adv. Drug Deliv. Rev.* **66**, 2–25 (2014).

14. Maeda, H. Toward a full understanding of the EPR effect in primary and metastatic tumors as well as issues related to its heterogeneity. *Adv. Drug Deliv. Rev.* **91**, 3–6 (2015).

15. Kołodziejczak-Radzimska, A. & Jesionowski, T. Zinc oxide—from synthesis to application: a review. *Materials (Basel).* **7**, 2833–2881 (2014).

16. Wang, Z. L. Nanostructures of zinc oxide. *Mater. today* **7**, 26–33 (2004).

17. Wiesmann, N., Tremel, W. & Brieger, J. Zinc oxide nanoparticles for therapeutic purposes in cancer medicine. *J. Mater. Chem. B* **8**, 4973–4989 (2020).

18. Ciofani, G. *Smart nanoparticles for biomedicine*. (Elsevier, 2018).

19. Rasmussen, J. W., Martinez, E., Louka, P. & Wingett, D. G. Zinc oxide nanoparticles for selective destruction of tumor cells and potential for drug delivery applications. *Expert Opin. Drug Deliv.* **7**, 1063–1077 (2010).

20. Punnoose, A. *et al.* Cytotoxicity of ZnO nanoparticles can be tailored by modifying their surface structure: A green chemistry approach for safer nanomaterials. *ACS Sustain. Chem. Eng.* **2**, 1666–1673 (2014).

21. Chen, B. *et al.* Targeting negative surface charges of cancer cells by multifunctional nanoprobes. *Theranostics* **6**, 1887 (2016).

22. Song, W. *et al.* Role of the dissolved zinc ion and reactive oxygen species in cytotoxicity of ZnO nanoparticles. *Toxicol. Lett.* **199**, 389–397 (2010).

23. Avramescu, M.-L., Rasmussen, P. E., Chénier, M. & Gardner, H. D. Influence of pH, particle size and crystal form on dissolution behaviour of engineered nanomaterials. *Environ. Sci. Pollut. Res.* **24**, 1553–1564 (2017).

24. Eixenberger, J. E. *et al.* Rapid dissolution of ZnO nanoparticles induced by biological buffers significantly impacts cytotoxicity. *Chem. Res. Toxicol.* **30**, 1641–1651 (2017).

25. Turney, T. W. *et al.* Formation of zinc-containing nanoparticles from Zn2+ ions in cell culture media: Implications for the nanotoxicology of ZnO. *Chem. Res. Toxicol.* **25**, 2057–2066 (2012).

26. Shen, C. *et al.* Relating cytotoxicity, zinc ions, and reactive oxygen in ZnO nanoparticle–exposed human immune cells. *Toxicol. Sci.* **136**, 120–130 (2013).

27. Mu, Q. *et al.* Systematic investigation of the physicochemical factors that contribute to the toxicity of ZnO nanoparticles. *Chem. Res. Toxicol.* **27**, 558–567 (2014).

28. Horie, M. *et al.* Protein adsorption of ultrafine metal oxide and its influence on cytotoxicity toward cultured cells. *Chem. Res. Toxicol.* **22**, 543–553 (2009).

29. Quadri, T. W., Olasunkanmi, L. O., Fayemi, O. E., Solomon, M. M. & Ebenso, E. E. Zinc oxide nanocomposites of selected polymers: synthesis, characterization, and corrosion inhibition studies on mild steel in HCl solution. *ACS omega* **2**, 8421–8437 (2017).

30. Ancona, A. *et al.* Lipid-coated zinc oxide nanoparticles as innovative ROS-generators for photodynamic therapy in cancer cells. *Nanomaterials* **8**, 143 (2018).

31. Chia, S. L. & Leong, D. T. Reducing ZnO nanoparticles toxicity through silica coating. *Heliyon* **2**, e00177 (2016).

32. Tavakoli, A. *et al.* Polyethylene glycol-coated zinc oxide nanoparticle: an efficient nanoweapon to fight against herpes simplex virus type 1. *Nanomedicine* **13**, 2675–2690 (2018).

33. Yin, H. *et al.* Reducing the cytotoxicity of ZnO nanoparticles by a pre-formed protein corona in a supplemented cell culture medium. *RSC Adv.* **5**, 73963–73973 (2015).

34. Zukiene, R. & Snitka, V. Zinc oxide nanoparticle and bovine serum albumin interaction and nanoparticles influence on cytotoxicity in vitro. *COLLOIDS AND SURFACES B-BIOINTERFACES* **135**, 316–323 (2015).

35. Anders, C. B., Chess, J. J., Wingett, D. G. & Punnoose, A. Serum Proteins Enhance Dispersion Stability and Influence the Cytotoxicity and Dosimetry of ZnO Nanoparticles in Suspension and Adherent Cancer Cell Models. *NANOSCALE Res. Lett.* **10**, (2015).

36. Ramasamy, M., Das, M., An, S. S. A. & Yi, D. K. Role of surface modification in zinc oxide nanoparticles and its toxicity assessment toward human dermal fibroblast cells. *Int. J. Nanomedicine* **9**, 3707–3718 (2014).

37. Xia, T. *et al.* Comparison of the mechanism of toxicity of zinc oxide and cerium oxide nanoparticles based on dissolution and oxidative stress properties. *ACS Nano* **2**, 2121–2134 (2008).

38. Yang, Q. B. & Ma, Y. F. Irradiation-Enhanced Cytotoxicity of Zinc Oxide Nanoparticles. *Int. J. Toxicol.* **33**, 187–203 (2014).

39. Hackenberg, S. *et al.* Zinc oxide nanoparticles induce photocatalytic cell death in human head and neck squamous cell carcinoma cell lines in vitro. *Int. J. Oncol.* **37**, 1583–1590 (2010).

40. Prasanna, V. L. & Vijayaraghavan, R. Insight into the Mechanism of Antibacterial Activity of ZnO: Surface Defects Mediated Reactive Oxygen Species Even in the Dark. *LANGMUIR* **31**, 9155–9162 (2015).

41. Choudhury, S. R. *et al.* Zinc oxide Nanoparticles-Induced Reactive Oxygen Species Promotes Multimodal Cyto- and Epigenetic Toxicity. *Toxicol. Sci.* **156**, 261–274 (2017).

42. Toduka, Y., Toyooka, T. & Ibuki, Y. Flow Cytometric Evaluation of Nanoparticles Using Side-Scattered Light and Reactive Oxygen Species-Mediated Fluorescence-Correlation with Genotoxicity. *Environ. Sci. Technol.* **46**, 7629–7636 (2012).

43. Ng, C. T. *et al.* Zinc oxide nanoparticles exhibit cytotoxicity and genotoxicity through oxidative stress responses in human lung fibroblasts and Drosophila melanogaster. *Int. J. Nanomedicine* **12**, 1621–1637 (2017).

44. Wahab, R. *et al.* ZnO Nanoparticles Induce Oxidative Stress in Cloudman S91 Melanoma Cancer Cells. *J. Biomed. Nanotechnol.* **9**, 441–449 (2013).

45. Moghaddam, A. B. *et al.* Eco-Friendly Formulated Zinc Oxide Nanoparticles: Induction of Cell Cycle Arrest and Apoptosis in the MCF-7 Cancer Cell Line. *Genes (Basel).* **8**, (2017).

46. Wahab, R. *et al.* ZnO nanoparticles induced oxidative stress and apoptosis in HepG2 and MCF-7 cancer cells and their antibacterial activity. *COLLOIDS AND SURFACES B-BIOINTERFACES* **117**, 267–276 (2014).

47. Ahamed, M. *et al.* ZnO nanorod-induced apoptosis in human alveolar adenocarcinoma cells via p53, survivin and bax/bcl-2 pathways: role of oxidative stress. *Nanomedicine*

Nanotechnology, Biol. Med. **7**, 904–913 (2011).

48. Bai, D. P., Zhang, X. F., Zhang, G. L., Huang, Y. F. & Gurunathan, S. Zinc oxide nanoparticles induce apoptosis and autophagy in human ovarian cancer cells. *Int. J. Nanomedicine* **12**, 6521–6535 (2017).

49. Wilhelmi, V. *et al.* Zinc Oxide Nanoparticles Induce Necrosis and Apoptosis in Macrophages in a p47phox-and Nrf2-Independent Manner. *PLoS One* **8**, (2013).

50. Garcia-Hevia, L. *et al.* Nano-ZnO leads to tubulin macrotube assembly and actin bundling, triggering cytoskeletal catastrophe and cell necrosis. *Nanoscale* **8**, 10963–10973 (2016).

51. Sharma, V., Anderson, D. & Dhawan, A. Zinc oxide nanoparticles induce oxidative DNA damage and ROS-triggered mitochondria mediated apoptosis in human liver cells (HepG2). *APOPTOSIS* **17**, 852–870 (2012).

52. Wang, J. F., Gao, S. T., Wang, S. Y., Xu, Z. N. & Wei, L. M. Zinc oxide nanoparticles induce toxicity in CAL 27 oral cancer cell lines by activating PINK1/Parkin-mediated mitophagy. *Int. J. Nanomedicine* **13**, 3441–3450 (2018).

53. Hanley, C. *et al.* Preferential killing of cancer cells and activated human T cells using ZnO nanoparticles. *Nanotechnology* **19**, (2008).

54. Ostrovsky, S., Kazimirsky, G., Gedanken, A. & Brodie, C. Selective Cytotoxic Effect of ZnO Nanoparticles on Glioma Cells. *NANO Res.* **2**, 882–890 (2009).

55. Sliwinski, T. *et al.* Zinc salts differentially modulate DNA damage in normal and cancer cells. *CELL Biol. Int.* **33**, 542–547 (2009).

56. Wang, H. *et al.* Fluorescent dye encapsulated ZnO particles with cell-specific toxicity for potential use in biomedical applications. *J. Mater. Sci. Med.* **20**, 11–22 (2009).

57. Premanathan, M., Karthikeyan, K., Jeyasubramanian, K. & Manivannan, G. Selective toxicity of ZnO nanoparticles toward Gram-positive bacteria and cancer cells by apoptosis through lipid peroxidation. *NANOMEDICINE-NANOTECHNOLOGY Biol. Med.* **7**, 184–192 (2011).

58. Sasidharan, A. *et al.* Rapid dissolution of ZnO nanocrystals in acidic cancer microenvironment leading to preferential apoptosis. *Nanoscale* **3**, 3657–3669 (2011).

59. Taccola, L. *et al.* Zinc oxide nanoparticles as selective killers of proliferating cells. *Int. J. Nanomedicine* **6**, (2011).

60. Akhtar, M. J. *et al.* Zinc oxide nanoparticles selectively induce apoptosis in human cancer cells through reactive oxygen species. *Int. J. Nanomedicine* **7**, 845 (2012).

61. Chandrasekaran, M. & Pandurangan, M. In Vitro Selective Anti-Proliferative Effect of Zinc Oxide Nanoparticles Against Co-Cultured C2C12 Myoblastoma Cancer and 3T3-L1 Normal Cells. *Biol. Trace Elem. Res.* **172**, 148–154 (2016).

62. Gupta, J., Bhargava, P. & Bahadur, D. Fluorescent ZnO for imaging and induction of DNA fragmentation and ROS-mediated apoptosis in cancer cells. *J. Mater. Chem. B* **3**, 1968–1978 (2015).

63. Hanley, C. *et al.* The Influences of Cell Type and ZnO Nanoparticle Size on Immune Cell Cytotoxicity and Cytokine Induction. *NANOSCALE Res. Lett.* **4**, 1409–1420 (2009).

64. Wingett, D., Louka, P., Anders, C. B., Zhang, J. & Punnoose, A. A role of ZnO nanoparticle electrostatic properties in cancer cell cytotoxicity. *Nanotechnol. Sci. Appl.* **9**, 29 (2016).

65. Sharma, H., Kumar, K., Choudhary, C., Mishra, P. K. & Vaidya, B. Development and characterization of metal oxide nanoparticles for the delivery of anticancer drug. *Artif. CELLS NANOMEDICINE Biotechnol.* **44**, 672–679 (2016).

66. Deng, Y. X. & Zhang, H. J. The synergistic effect and mechanism of doxorubicin-ZnO nanocomplexes as a multimodal agent integrating diverse anticancer therapeutics. *Int. J. Nanomedicine* **8**, 1835–1841 (2013).

67. Aswathanarayan, J. B., Vittal, R. R. & Muddegowda, U. Anticancer activity of metal nanoparticles and their peptide conjugates against human colon adenorectal carcinoma cells. *Artif. CELLS NANOMEDICINE Biotechnol.* **46**, 1444–1451 (2018).

68. Hackenberg, S. *et al.* Antitumor activity of photo-stimulated zinc oxide nanoparticles combined with paclitaxel or cisplatin in HNSCC cell lines. *J. Photochem. Photobiol. B-BIOLOGY* **114**, 87–93 (2012).

69. Guo, D. D. *et al.* Synergistic cytotoxic effect of different sized ZnO nanoparticles and daunorubicin against leukemia cancer cells under UV irradiation. *J. Photochem. Photobiol. B-BIOLOGY* **93**, 119–126 (2008).

70. Generalov, R., Kuan, W. B., Chen, W., Kristensen, S. & Juzenas, P. Radiosensitizing effect of zinc oxide and silica nanocomposites on cancer cells. *COLLOIDS AND SURFACES B-BIOINTERFACES* **129**, 79–86 (2015).

71. Wang, C. C. *et al.* Phototoxicity of Zinc Oxide Nanoparticles in HaCaT Keratinocytes-Generation of Oxidative DNA Damage During UVA and Visible Light Irradiation. *J. Nanosci. Nanotechnol.* **13**, 3880–3888 (2013).

72. Hosny, A. E.-D. M., Kashef, M. T., Taher, H. A. & El-Bazza, Z. E. The use of unirradiated and γ-irradiated zinc oxide nanoparticles as a preservative in cosmetic preparations. *Int. J. Nanomedicine* **12**, 6799 (2017).

73. Bedi, P. & Kaur, A. An overview on uses of zinc oxide nanoparticles. *World J. Pharm. Pharm. Sci.* **4**, 1177–1196 (2015).

74. Mishra, P. K., Mishra, H., Ekielski, A., Talegaonkar, S. & Vaidya, B. Zinc oxide nanoparticles: a promising nanomaterial for biomedical applications. *Drug Discov. Today* **22**, 1825–1834 (2017).

75. Li, C. H. *et al.* Organ biodistribution, clearance, and genotoxicity of orally administered zinc oxide nanoparticles in mice. *Nanotoxicology* **6**, 746–756 (2012).

76. Fujihara, J. *et al.* Distribution and toxicity evaluation of ZnO dispersion nanoparticles in single intravenously exposed mice. *J. Med. Investig.* **62**, 45–50 (2015).

77. Aula, S. *et al.* Route of administration induced in vivo effects and toxicity responses of

Zinc Oxide nanorods at molecular and genetic levels. *Int. J. Nano Dimens.* **9**, 158–169 (2018).

78. Chowdhury, S., Sinha, K., Banerjee, S. & Sil, P. C. Taurine protects cisplatin induced cardiotoxicity by modulating inflammatory and endoplasmic reticulum stress responses. *Biofactors* **42**, 647–664 (2016).

79. Banerjee, S., Sinha, K., Chowdhury, S. & Sil, P. C. Unfolding the mechanism of cisplatin induced pathophysiology in spleen and its amelioration by carnosine. *Chem. Biol. Interact.* **279**, 159–170 (2018).

80. Sompar, N., Kukongviriyapan, V., Kukongviriyapan, U., Senggunprai, L. & Prawan, A. Protective effects of tetrahydrocurcumin and curcumin against doxorubicin and cadmium-induced cytotoxicity in Chang liver cells. *Trop. J. Pharm. Res.* **14**, 769–776 (2015).

81. Brigger, I., Dubernet, C. & Couvreur, P. Nanoparticles in cancer therapy and diagnosis. *Adv. Drug Deliv. Rev.* **64**, 24–36 (2012).

82. Brannon-Peppas, L. & Blanchette, J. O. Nanoparticle and targeted systems for cancer therapy. *Adv. Drug Deliv. Rev.* **56**, 1649–1659 (2004).

83. Kang, B., Opatz, T., Landfester, K. & Wurm, F. R. Carbohydrate nanocarriers in biomedical applications: functionalization and construction. *Chem. Soc. Rev.* **44**, 8301–8325 (2015).

84. Duncan, R. & Richardson, S. C. W. Endocytosis and Intracellular Trafficking as Gateways for Nanomedicine Delivery: Opportunities and Challenges. *Mol. Pharm.* **9**, 2380–2402 (2012).

85. Huang, X., Zheng, X., Xu, Z. J. & Yi, C. X. ZnO-based nanocarriers for drug delivery application: From passive to smart strategies. *Int. J. Pharm.* **534**, 190–194 (2017).

86. Accardo, A., Aloj, L., Aurilio, M., Morelli, G. & Tesauro, D. Receptor binding peptides for target-selective delivery of nanoparticles encapsulated drugs. *Int. J. Nanomedicine* **9**, 1537–1557 (2014).

87. Croissant, J. & Zink, J. I. Nanovalve-Controlled Cargo Release Activated by Plasmonic Heating. *J. Am. Chem. Soc.* **134**, 7628–7631 (2012).

88. Du, J. Z., Du, X. J., Mao, C. Q. & Wang, J. Tailor-Made Dual pH-Sensitive Polymer-Doxorubicin Nanoparticles for Efficient Anticancer Drug Delivery. *J. Am. Chem. Soc.* **133**, 17560–17563 (2011).

89. Voliani, V. *et al.* Multiphoton Molecular Photorelease in Click-Chemistry-Functionalized Gold Nanoparticles. *SMALL* **7**, 3271–3275 (2011).

90. Barick, K. C., Nigam, S. & Bahadur, D. Nanoscale assembly of mesoporous ZnO: A potential drug carrier. *J. Mater. Chem.* **20**, 6446–6452 (2010).

91. Muhammad, F. *et al.* pH-triggered controlled drug release from mesoporous silica nanoparticles via intracelluar dissolution of ZnO nanolids. *J. Am. Chem. Soc.* **133**, 8778–8781 (2011).

92. Liu, Y. *et al.* ZnO quantum dots-embedded collagen/polyanion composite hydrogels with

integrated functions of degradation tracking/inhibition and gene delivery. *J. Mater. Chem.* **22**, 512–519 (2012).

93. Zhang, Z. *et al.* Biodegradable ZnO@ polymer core–shell nanocarriers: pH-triggered release of doxorubicin in vitro. *Angew. chemie* **125**, 4221–4225 (2013).

94. Gong, Y., Ji, Y., Liu, F., Li, J. & Cao, Y. Cytotoxicity, oxidative stress and inflammation induced by ZnO nanoparticles in endothelial cells: interaction with palmitate or lipopolysaccharide. *J. Appl. Toxicol.* **37**, 895–901 (2017).

95. O'Shaughnessy, J. Extending survival with chemotherapy in metastatic breast cancer. *Oncologist* **10**, 20–29 (2005).

96. Wagner, D., Kern, W. V & Kern, P. Liposomal doxorubicin in AIDS-related Kaposi's sarcoma: long-term experiences. *Clin. Investig.* **72**, 417–423 (1994).

97. Collins, Y. & Lele, S. Long-term pegylated liposomal doxorubicin use in recurrent ovarian carcinoma. *J. Natl. Med. Assoc.* **97**, 1414 (2005).

98. Carvalho, C. *et al.* Doxorubicin: the good, the bad and the ugly effect. *Curr. Med. Chem.* **16**, 3267–3285 (2009).

99. Hilmer, S. N., Cogger, V. C., Muller, M. & Le Couteur, D. G. The hepatic pharmacokinetics of doxorubicin and liposomal doxorubicin. *DRUG Metab. Dispos.* **32**, 794–799 (2004).

100. Mitra, S. *et al.* Porous ZnO nanorod for targeted delivery of doxorubicin: in vitro and in vivo response for therapeutic applications. *J. Mater. Chem.* **22**, 24145–24154 (2012).

101. Tan, L. C., Liu, J., Zhou, W. H., Wei, J. C. & Peng, Z. P. A novel thermal and pH responsive drug delivery system based on ZnO@PNIPAM hybrid nanoparticles. *Mater. Sci. Eng. C-MATERIALS Biol. Appl.* **45**, 524–529 (2014).

102. Cai, X. L., Luo, Y. N., Zhang, W. Y., Du, D. & Lin, Y. H. pH-Sensitive ZnO Quantum Dots-Doxorubicin Nanoparticles for Lung Cancer Targeted Drug Delivery. *ACS Appl. Mater. Interfaces* **8**, 22442–22450 (2016).

103. Zheng, C. C., Wang, Y., Phua, S. Z. F., Lim, W. Q. & Zhao, Y. L. ZnO-DOX@ZIF-8 Core-Shell Nanoparticles for pH-Responsive Drug Delivery. *ACS Biomater. Sci. Eng.* **3**, 2223–2229 (2017).

104. Al Dine, E. J. *et al.* A Facile Approach for Doxorubicine Delivery in Cancer Cells by Responsive and Fluorescent Core/Shell Quantum Dots. *Bioconjug. Chem.* **29**, 2248–2256 (2018).

105. Yang, X. X., Zhang, C., Li, A. X., Wang, J. & Cai, X. L. Red fluorescent ZnO nanoparticle grafted with polyglycerol and conjugated RGD peptide as drug delivery vehicles for efficient target cancer therapy. *Mater. Sci. Eng. C-MATERIALS Biol. Appl.* **95**, 104–113 (2019).

106. Chen, M. M. *et al.* pH-Responsive and Biodegradable ZnO-Capped Mesoporous Silica Composite Nanoparticles for Drug Delivery. *Materials (Basel).* **13**, (2020).

107. Bai, H. & Liu, X. Green hydrothermal synthesis and photoluminescence property of ZnO2

nanoparticles. *Mater. Lett.* **64**, 341–343 (2010).

108. Gondal, M. A., Drmosh, Q. A., Yamani, Z. H. & Saleh, T. A. Synthesis of ZnO2 nanoparticles by laser ablation in liquid and their annealing transformation into ZnO nanoparticles. *Appl. Surf. Sci.* **256**, 298–304 (2009).

109. Sun, M., Hao, W., Wang, C. & Wang, T. A simple and green approach for preparation of ZnO2 and ZnO under sunlight irradiation. *Chem. Phys. Lett.* **443**, 342–346 (2007).

110. Chen, W. *et al.* Synthesis, thermal stability and properties of ZnO2 nanoparticles. *J. Phys. Chem. C* **113**, 1320–1324 (2009).

111. Rosenthal-Toib, L., Zohar, K., Alagem, M. & Tsur, Y. Synthesis of stabilized nanoparticles of zinc peroxide. *Chem. Eng. J.* **136**, 425–429 (2008).

112. Yang, L. Y., Feng, G. P. & Wang, T. X. Green synthesis of ZnO2 nanoparticles from hydrozincite and hydrogen peroxide at room temperature. *Mater. Lett.* **64**, 1647–1649 (2010).

113. Uekawa, N. *et al.* Nonstoichiometric properties of zinc oxide nanoparticles prepared by decomposition of zinc peroxide. *Phys. Chem. Chem. Phys.* **5**, 929–934 (2003).

114. Han, X., Liu, R., Chen, W. & Xu, Z. Properties of nanocrystalline zinc oxide thin films prepared by thermal decomposition of electrodeposited zinc peroxide. *Thin Solid Films* **516**, 4025–4029 (2008).

115. Cheng, S. *et al.* Soft-template synthesis and characterization of ZnO2 and ZnO hollow spheres. *J. Phys. Chem. C* **113**, 13630–13635 (2009).

116. Sebők, D., Szabó, T. & Dékány, I. Optical properties of zinc peroxide and zinc oxide multilayer nanohybrid films. *Appl. Surf. Sci.* **255**, 6953–6962 (2009).

117. Wolanov, Y., Prikhodchenko, P. V, Medvedev, A. G., Pedahzur, R. & Lev, O. Zinc dioxide nanoparticulates: a hydrogen peroxide source at moderate pH. *Environ. Sci. Technol.* **47**, 8769–8774 (2013).

118. Bawn, C. E. H. & Margerison, D. Molecular dissociation processes in solution. Part 4.—The rate of decomposition of persulphate ion and its catalysis by metal ions. *Trans. Faraday Soc.* **51**, 925–934 (1955).

119. Colonia, R., Solís, J. L. & Gómez, M. Bactericidal, structural and morphological properties of ZnO2 nanoparticles synthesized under UV or ultrasound irradiation. *Adv. Nat. Sci. Nanosci. Nanotechnol.* **5**, 15008 (2013).

120. Ali, S. S., Morsy, R., El-Zawawy, N. A., Fareed, M. F. & Bedaiwy, M. Y. Synthesized zinc peroxide nanoparticles (ZnO2-NPs): a novel antimicrobial, anti-elastase, anti-keratinase, and anti-inflammatory approach toward polymicrobial burn wounds. *Int. J. Nanomedicine* **12**, 6059 (2017).

121. Elbahri, M. *et al.* Underwater Leidenfrost nanochemistry for creation of size-tailored zinc peroxide cancer nanotherapeutics. *Nat. Commun.* **8**, 1–10 (2017).

122. Taale, M. *et al.* Bioactive carbon-based hybrid 3D scaffolds for osteoblast growth. *ACS Appl. Mater. Interfaces* **10**, 43874–43886 (2018).

123. Mecklenburg, M. *et al.* Aerographite: ultra lightweight, flexible nanowall, carbon microtube material with outstanding mechanical performance. *Adv. Mater.* **24**, 3486–3490 (2012).

124. Shree, S. Interactive Interfaces of Smart Composites. (2019).

125. Adelung, R. *et al.* Elastic material with a pore space bridged at the particle level by nanobridges betweenparticles. (2016).

126. Mishra, Y. K. *et al.* Fabrication of macroscopically flexible and highly porous 3D semiconductor networks from interpenetrating nanostructures by a simple flame transport approach. *Part. \& Part. Syst. Charact.* **30**, 775–783 (2013).

127. Mishra, Y. K. *et al.* Virostatic potential of micro–nano filopodia-like ZnO structures against herpes simplex virus-1. *Antiviral Res.* **92**, 305–312 (2011).

128. Antoine, T. E. *et al.* Prophylactic, therapeutic and neutralizing effects of zinc oxide tetrapod structures against herpes simplex virus type-2 infection. *Antiviral Res.* **96**, 363–375 (2012).

129. Wille, S. *et al.* Zinc oxide micro-and nanostructures as multifunctional materials. *SPIE Newsroom* (2011).

130. Papavlassopoulos, H. *et al.* Toxicity of functional nano-micro zinc oxide tetrapods: impact of cell culture conditions, cellular age and material properties. *PLoS One* **9**, e84983 (2014).

131. Burdall, S. E., Hanby, A. M., Lansdown, M. R. J. & Speirs, V. Breast cancer cell lines: friend or foe? *Breast cancer Res.* **5**, 1–7 (2003).

132. Baguley, B. C. & Leung, E. Heterogeneity of phenotype in breast cancer cell lines. *Breast Cancer-Carcinog. Cell Growth Signal. Pathways* **2**, 732 (2011).

133. Shirazi, F. H. *et al. Remarks in successful cellular investigations for fighting breast cancer using novel synthetic compounds*. (INTECH Open Access Publisher Croatia, 2011).

134. Sweeney, E. E., McDaniel, R. E., Maximov, P. Y., Fan, P. & Jordan, V. C. Models and mechanisms of acquired antihormone resistance in breast cancer: significant clinical progress despite limitations. *Horm. Mol. Biol. Clin. Investig.* **9**, 143–163 (2012).

135. Gest, C. *et al.* Rac3 induces a molecular pathway triggering breast cancer cell aggressiveness: differences in MDA-MB-231 and MCF-7 breast cancer cell lines. *BMC Cancer* **13**, 1–14 (2013).

136. Anderson, A. CM-DiI and MCF-7 Breast Cancer Cell Responses to Chemotherapeutic Agents. (2018).

137. Niles, A. L. *et al.* A homogeneous assay to measure live and dead cells in the same sample by detecting different protease markers. *Anal. Biochem.* **366**, 197–206 (2007).

138. Casey, J. R., Grinstein, S. & Orlowski, J. Sensors and regulators of intracellular pH. *Nat. Rev. Mol. cell Biol.* **11**, 50–61 (2010).

139. Becker, J. S. & Jakubowski, N. The synergy of elemental and biomolecular mass spectrometry: new analytical strategies in life sciences. *Chem. Soc. Rev.* **38**, 1969–1983

(2009).

140. Richter, P., Toral, M. I., Fuenzalida, E. & Tapia, A. E. Flow injection photometric determination of zinc and copper with Zincon based on the variation of the stability of the complexes with pH. *Analyst* **122**, 1045–1048 (1997).

141. McCall, K. A. & Fierke, C. A. Colorimetric and fluorimetric assays to quantitate micromolar concentrations of transition metals. *Anal. Biochem.* **284**, 307–315 (2000).

142. Cheng, K. L., Ueno, K. & Imainura, T. Handbook of Organic Analytical Reagents, CRC PRES. *INC, Boca Rat. Flórida* (1982).

143. Rush, R. M. & Yoe, J. H. Colorimetric Determination of Zinc and Copper with 2-Carboxy-2-hydroxy-5-sulfoformazylbenzene. *Anal. Chem.* **26**, 1345–1347 (1954).

144. Säbel, C. E., Shepherd, J. L. & Siemann, S. A direct spectrophotometric method for the simultaneous determination of zinc and cobalt in metalloproteins using 4-(2-pyridylazo) resorcinol. *Anal. Biochem.* **391**, 74–76 (2009).

145. Coyle, P. *et al.* Measurement of zinc in hepatocytes by using a fluorescent probe, zinquin: relationship to metallothionein and intracellular zinc. *Biochem. J.* **303**, 781–786 (1994).

146. Fatikow, S. *Automated nanohandling by microrobots*. (Springer Science & Business Media, 2007).

147. Yacobi, B. G. *Semiconductor materials: an introduction to basic principles*. (Springer Science & Business Media, 2003).

148. Yadav, L. D. S. Ultraviolet (UV) and visible spectroscopy. in *Organic Spectroscopy* 7–51 (Springer, 2005).

149. Robertson, J. H. Elements of X-ray diffraction by BD Cullity. (1979).

150. Suryanarayana, C. & Norton, M. G. Practical aspects of X-ray diffraction. in *X-ray Diffraction* 63–94 (Springer, 1998).

151. Su, D. Advanced electron microscopy characterization of nanomaterials for catalysis. *Green Energy Environ.* **2**, 70–83 (2017).

152. Scimeca, M., Bischetti, S., Lamsira, H. K., Bonfiglio, R. & Bonanno, E. Energy Dispersive X-ray (EDX) microanalysis: A powerful tool in biomedical research and diagnosis. *Eur. J. Histochem. EJH* **62**, (2018).

153. Hodoroaba, V., Rades, S. & Unger, W. E. S. Inspection of morphology and elemental imaging of single nanoparticles by high-resolution SEM/EDX in transmission mode. *Surf. interface Anal.* **46**, 945–948 (2014).

154. Papavlassopoulos, H. *et al.* Toxicity of functional nano-micro zinc oxide tetrapods: Impact of cell culture conditions, cellular age and material properties. *PLoS One* **9**, (2014).

155. Säbel, C. E., Neureuther, J. M. & Siemann, S. A spectrophotometric method for the determination of zinc, copper, and cobalt ions in metalloproteins using Zincon. *Anal. Biochem.* **397**, 218–226 (2010).

156. Bhattacharjee, A., Purkait, M. K. & Gumma, S. Loading and release of doxorubicin hydrochloride from Iron (III) trimesate MOF and zinc oxide nanoparticle composites. *Dalt. Trans.* **49**, 8755–8763 (2020).

157. Özgür, Ü. *et al.* A comprehensive review of ZnO materials and devices. *J. Appl. Phys.* **98**, 11 (2005).

158. Ursaki, V. V, Lupan, O. I., Chow, L., Tiginyanu, I. M. & Zalamai, V. V. Rapid thermal annealing induced change of the mechanism of multiphonon resonant Raman scattering from ZnO nanorods. *Solid State Commun.* **143**, 437–441 (2007).

159. Šćepanović, M., Grujić-Brojčin, M., Vojisavljević, K., Bernik, S. & Srećković, T. Raman study of structural disorder in ZnO nanopowders. *J. Raman Spectrosc.* **41**, 914–921 (2010).

160. Postica, V. *et al.* Multifunctional device based on ZnO: Fe nanostructured films with enhanced UV and ultra-fast ethanol vapour sensing. *Mater. Sci. Semicond. Process.* **49**, 20–33 (2016).

161. Hu, P. A., Liu, Y. Q., Fu, L., Wang, X. B. & Zhu, D. B. Controllable morphologies of ZnO nanocrystals: nanowire attracted nanosheets, nanocartridges and hexagonal nanotowers. *Appl. Phys. A* **80**, 35–38 (2005).

162. Giannakoudakis, D. A. *et al.* Zinc peroxide nanoparticles: surface, chemical and optical properties and the effect of thermal treatment on the detoxification of mustard gas. *Appl. Catal. B Environ.* **226**, 429–440 (2018).

163. Tawale, J. S., Dey, K. K., Pasricha, R., Sood, K. N. & Srivastava, A. K. Synthesis and characterization of ZnO tetrapods for optical and antibacterial applications. *Thin Solid Films* **519**, 1244–1247 (2010).

164. Abrahams, S. C. & Bernstein, J. L. Remeasurement of the structure of hexagonal ZnO. *Acta Crystallogr. Sect. B Struct. Crystallogr. Cryst. Chem.* **25**, 1233–1236 (1969).

165. Heng, B. C. *et al.* Cytotoxicity of zinc oxide (ZnO) nanoparticles is influenced by cell density and culture format. *Arch. Toxicol.* **85**, 695–704 (2011).

166. Moos, P. J. *et al.* ZnO particulate matter requires cell contact for toxicity in human colon cancer cells. *Chem. Res. Toxicol.* **23**, 733–739 (2010).

167. Sun, R.-D., Nakajima, A., Fujishima, A., Watanabe, T. & Hashimoto, K. Photoinduced surface wettability conversion of ZnO and TiO2 thin films. *J. Phys. Chem. B* **105**, 1984–1990 (2001).

168. Feng, X. *et al.* Reversible super-hydrophobicity to super-hydrophilicity transition of aligned ZnO nanorod films. *J. Am. Chem. Soc.* **126**, 62–63 (2004).

169. H. Müller, K. *et al.* pH-dependent toxicity of high aspect ratio ZnO nanowires in macrophages due to intracellular dissolution. *ACS Nano* **4**, 6767–6779 (2010).

170. Adam, N. *et al.* The chronic toxicity of ZnO nanoparticles and ZnCl2 to Daphnia magna and the use of different methods to assess nanoparticle aggregation and dissolution. *Nanotoxicology* **8**, 709–717 (2014).

171. Andre, F. & Zielinski, C. C. Optimal strategies for the treatment of metastatic triple-negative breast cancer with currently approved agents. *Ann. Oncol.* **23**, vi46–vi51 (2012).

172. Bacchetta, R. *et al.* Evidence and uptake routes for Zinc oxide nanoparticles through the gastrointestinal barrier in Xenopus laevis. *Nanotoxicology* **8**, 728–744 (2014).

173. Churchman, A. H. *et al.* Serum albumin enhances the membrane activity of ZnO nanoparticles. *Chem. Commun.* **49**, 4172–4174 (2013).

174. Gilbert, B. *et al.* The fate of ZnO nanoparticles administered to human bronchial epithelial cells. *ACS Nano* **6**, 4921–4930 (2012).

175. Lin, W. *et al.* Toxicity of nano-and micro-sized ZnO particles in human lung epithelial cells. *J. Nanoparticle Res.* **11**, 25–39 (2009).

176. Hong, H. *et al.* Cancer-targeted optical imaging with fluorescent zinc oxide nanowires. *Nano Lett.* **11**, 3744–3750 (2011).

177. Othman, B. A. *et al.* Correlative light-electron microscopy shows RGD-targeted ZnO nanoparticles dissolve in the intracellular environment of triple negative breast cancer cells and cause apoptosis with intratumor heterogeneity. *Adv. Healthc. Mater.* **5**, 1310–1325 (2016).

178. Adam, N. *et al.* The chronic toxicity of ZnO nanoparticles and ZnCl2 to Daphnia magna and the use of different methods to assess nanoparticle aggregation and dissolution. *Nanotoxicology* **8**, 709–717 (2014).

Declaration

Hiermit erkläre ich an Eides statt, diese Dissertation eigenständig, d.h. insbesondere selbständig und ohne Hilfe eines kommerziellen Promotionsberaters, angefertigt und keine anderen als die von mir angegebenen Quellen und Hilfsmittel verwendet zu haben. Ich erkläre außerdem, dass die Dissertation weder in gleicher noch in ähnlicher Form bere- its in einem anderen Prüfungsverfahren vorgelegen hat und unter Einhaltung der Regeln guter wissenschaftlicher Praxis der Deutschen Forschungsgemeinschaft entstanden ist. Es wurde kein akademischer Grad entzogen.

_____ _____

Ort, Datum Unterschrift

I hereby confirm that this dissertation is the result of my own work. I did not receive any help or support from commercial consultants. All sources and/or materials applied here are listed and specified in the thesis. Furthermore, I confirm that this thesis has not yet been submitted as part of another examination process, neither in identical nor in similar form, and has been prepared subject to the Rules of Good Scientific Practice of the German Research Foundation. No academic degree has been withdrawn.

_____ _____

Place, Date Signature

Rightslink® by Copyright Clearance Center

RightsLink

Help | Live Chat

SPRINGER NATURE

Underwater Leidenfrost nanochemistry for creation of size-tailored zinc peroxide cancer nanotherapeutics

Author: Mady Elbahri et al
Publication: Nature Communications
Publisher: Springer Nature
Date: May 12, 2017

Creative Commons

Creative Commons License Deed

Attribution 4.0 International (CC BY 4.0)

This is a human-readable summary of (and not a substitute for) the license.

You are free to:

Share — copy and redistribute the material in any medium or format

Adapt — remix, transform, and build upon the material

for any purpose, even commercially.

The licensor cannot revoke these freedoms as long as you follow the license terms.

Under the following terms:

Attribution — You must give appropriate credit, provide a link to the license, and indicate if changes were made. You may do so in any reasonable manner, but not in any way that suggests the licensor endorses you or your use.

No additional restrictions — You may not apply legal terms or technological measures that legally restrict others from doing anything the license permits.

Notices:

You do not have to comply with the license for elements of the material in the public domain or where your use is permitted by an applicable exception or limitation.

No warranties are given. The license may not give you all of the permissions necessary for your intended use. For example, other rights such as publicity, privacy, or moral rights may limit how you use the material.